

– 1 –

Accretion in the Early Kuiper Belt

I. Coagulation and Velocity Evolution

Scott J. Kenyon

Harvard-Smithsonian Center for Astrophysics

60 Garden Street, Cambridge, MA 02138

e-mail: skenyon@cfa.harvard.edu

and

Jane X. Luu

Department of Astronomy

Harvard University

60 Garden Street, Cambridge, MA 02138

e-mail: jluu@cfa.harvard.edu

to appear in

The Astronomical Journal

May 1998

Received 5 November 1997; accepted 2 February 1998

ABSTRACT

We describe planetesimal accretion calculations in the Kuiper Belt. Our evolution code simulates planetesimal growth in a single annulus and includes velocity evolution but not fragmentation. Test results match analytic solutions and duplicate previous simulations at 1 AU.

In the Kuiper Belt, simulations without velocity evolution produce a single runaway body with a radius $r_i \gtrsim 1000$ km on a time scale $\tau_r \propto M_0^{-1} e_0^x$, where M_0 is the initial mass in the annulus, e_0 is the initial eccentricity of the planetesimals, and $x \approx 1\text{--}2$. Runaway growth occurs in 100 Myr for $M_0 \approx 10 M_{\oplus}$ and $e_0 \approx 10^{-3}$ in a 6 AU annulus centered at 35 AU. This mass is close to the amount of dusty material expected in a minimum mass solar nebula extrapolated into the Kuiper Belt.

Simulations with velocity evolution produce runaway growth on a wide range of time scales. Dynamical friction and viscous stirring increase particle velocities in models with large (8 km radius) initial bodies. This velocity increase delays runaway growth by a factor of two compared to models without velocity evolution. In contrast, collisional damping dominates over dynamical friction and viscous stirring in models with small (80–800 m radius) initial bodies. Collisional damping decreases the time scale to runaway growth by factors of 4–10 relative to constant velocity calculations. Simulations with minimum mass solar nebulae, $M_0 \sim 10 M_{\oplus}$, and small eccentricities, $e \approx 10^{-3}$, reach runaway growth on time scales of 20–40 Myr with 80 m initial bodies, 50–100 Myr with 800 m bodies, and 75–250 Myr for 8 km initial bodies. These growth times vary linearly with the mass of the annulus, $\tau_r \propto M_0^{-1}$, but are less sensitive to the initial eccentricity than constant velocity models.

In both sets of models, the time scales to produce 1000+ km objects are comparable to estimated formation time scales for Neptune. Thus, Pluto-sized objects can form in the outer solar system in parallel with the condensation of the outermost large planets.

1. INTRODUCTION

Current models for planet formation involve aggregation of solid planetesimals and gas accretion in a circumstellar disk (see, for example, Hayashi *et al.* 1985; Boss 1993; and references therein). Large dust grains within the disk first settle to the midplane. These grains may then coagulate into successively larger grains (e.g., Weidenschilling 1980; Weidenschilling & Cuzzi 1985) or continue to settle in a very thin layer that eventually becomes gravitationally unstable (e.g., Goldreich & Ward 1973). Both paths produce km-sized planetesimals that collide and merge to produce large bodies such as planets. Despite the complex and sometimes unknown physics, many simulations produce objects resembling known planets on time scales roughly comparable to the expected lifetime of the protosolar nebula (see, for example, Safronov 1969; Greenberg *et al.* 1978, 1984; Nakagawa *et al.* 1983; Wetherill & Stewart 1989; 1993; Spaute *et al.* 1991; Kolvoord & Greenberg 1992; Weidenschilling & Davis 1992; Pollack *et al.* 1996).

Recent observations of slow-moving objects in the outer solar system offer a new challenge to planet formation models. The trans-Neptunian region now contains several dozen Kuiper Belt objects (KBOs) with estimated radii of 100–300 km (Jewitt *et al.* 1996). The orbits of known KBOs suggest a division into at least three dynamical components with an inner radius of 30 AU and an unknown outer radius: (i) the classical KBOs, objects with roughly circular orbits, (ii) the resonant KBOs, objects in orbital resonance with Neptune (Jewitt *et al.* 1996), and (iii) the scattered KBOs, objects with large, eccentric orbits (Luu *et al.* 1997). Although the known population is still small, Jewitt *et al.* (1996) estimate that the region between 30 and 50 AU contains $\approx 70,000$ objects larger than 100 km. The total mass in the classical Kuiper Belt is thus at least $0.1 M_{\oplus}$. This mass probably represents a small fraction of the initial mass, because dynamical interactions with Neptune reduce the number of KBOs on short time scales compared to the age of the solar system (Levison & Duncan 1993; Malhotra 1996).

Despite these new observations, the origin of KBOs remains uncertain. Edgeworth (1949) and Kuiper (1951) first suggested that the Kuiper Belt was a natural extension of the original solar nebula. Holman & Wisdom (1993) later showed that small KBOs, once formed, can survive at 30–50 AU for times approaching the age of the solar system. More recent dynamical studies confirm this conclusion and explain the observed distribution of KBOs in a general way (Levison & Duncan 1993). The formation process and time scale for KBOs, however, is still controversial. Planetesimal simulations for plausible protosolar nebulae at 25–30 AU show that Neptune can grow to its present size in 10–100 Myr (Fernández & Ip 1981, 1984; Ip 1989; Pollack *et al.* 1996). These results suggest that Pluto might form on a similar time scale at ~ 40 AU, because growth times are not a steep function of semi-major axis (see Aarseth *et al.* 1993; Pollack *et al.* 1996; and references therein). Nevertheless, Stern (1995, 1996) and Stern & Colwell (1997) conclude that KBO

formation requires 100–1000 Myr for the conditions expected in the outer solar system. These limits far exceed the time scale required to produce Neptune, whose accretion time is constrained by the 10–100 Myr lifetime of the protosolar nebula (see Pollack *et al.* 1996 and references therein).

In this paper, we attempt to resolve the uncertainties surrounding KBO production with a new planetesimal simulation at 35 AU. We have developed an evolution code to follow the growth and velocity evolution of planetesimals with a wide range of initial masses. The code matches analytic models and duplicates Wetherill & Stewart’s (1993; hereafter WS93) simulation of planetesimal evolution at 1 AU. Our numerical results demonstrate that small bodies with initial radii of 80 m to 8 km can produce 1000+ km objects on time scales of 10–100 Myr. We confirm these calculations with a simple analytic estimate of the growth time as a function of semi-major axis. This analysis supports previous estimates for a short growth phase for Neptune, 10–100 Myr, and indicates that Pluto-Charon can form just outside the current orbit of Neptune on a similar time scale.

We outline the accretion model in Sec. 2, describe our calculations in Sec. 3, and conclude with a discussion and summary in Sec. 4. The Appendix contains a complete description of the algorithms and detailed comparisons with analytic models.

2. The Accretion Model

For our simulations of accretion in the Kuiper Belt, we adopt Safronov’s (1969) particle-in-a-box method, where planetesimals are treated as a statistical ensemble of masses with a distribution of horizontal and vertical velocities about a Keplerian orbit. Our simulations begin with a differential mass distribution, $n(m_i)$, in a single accumulation zone centered at a heliocentric distance, a , with an inner radius at $a - \Delta a/2$ and an outer radius at $a + \Delta a/2$. We approximate the continuous distribution of particle masses with discrete batches having particle populations $n_i(t)$ and total masses $M_i(t)$ (WS93). The average mass of a batch, $m_i(t) = M_i(t)/n_i(t)$, changes with time as collisions add and remove bodies from the batch. This procedure naturally conserves mass and allows a coarser grid than simulations with fixed mass bins (Wetherill 1990, and references therein; WS93).

To evolve the mass and velocity distributions in time, we solve the coagulation and energy conservation equations for an ensemble of objects with masses ranging from $\sim 10^{12}$ g to $\sim 10^{26}$ g. The Appendix describes our model in detail and compares our numerical results with analytic solutions for standard test cases. We adopt analytic cross-sections to derive collision rates and compute velocity changes from gas drag and collective interactions such as dynamical friction and viscous stirring. Our initial approach to this problem ignores fragmentation, which we will consider in a later paper. In this study, we focus on developing a good understanding of planetesimal growth as a function of initial conditions

in the Kuiper Belt.

To test our numerical procedures in detail, we attempt to duplicate WS93’s simulations of planetary embryo formation at 1 AU. WS93 (see also Wetherill & Stewart 1989; Barge & Pellat 1990, 1991, 1993; Spaute *et al.* 1991; Aarseth *et al.* 1993) demonstrate that an ensemble of 8 km objects can produce 10^{26} g (Moon-sized) objects on a 10^5 yr time scale. WS93’s model begins with 8.33×10^8 planetesimals having radii of 8 km and a velocity dispersion of 4.7 m s^{-1} relative to a Keplerian orbit (Table 1; see also Table 1 of WS93). Tables 2–3 summarize our results using the WS93 initial conditions with a mass spacing factor of $\delta \equiv m_{i+1}/m_i = 1.25$ and 1.4 between successive mass batches and two different analytic cross-sections. Figure 1 shows our reproduction of the WS93 results without fragmentation for $\delta = 1.25$. This simulation produces $14.3 - 9 \times 10^{25}$ g objects in 1.5×10^5 yr, which agrees with the results in WS93 (see their Figure 12). Our simulation confirms the broad “plateau” in the cumulative number, N_C , at $\log m_i = 24 - 26$ and the rough power law dependence, $N_C \propto m_i^{-1}$, at $\log m_i = 21 - 23$. The broad plateau extends across a smaller mass range and becomes more rounded as δ increases (Figure 2). The maximum planetesimal mass, m_{max} , at the conclusion of the calculation depends on both δ and the cross-sections. We find marginally larger m_{max} for the Spaute *et al.* (1991) cross-sections. In general, m_{max} increases as δ increases.

The evolution of particle velocities in our simulations agrees with the WS93 results (Figure 1b). All of the velocities increase monotonically with time due to viscous stirring. The velocities of the larger bodies increase very slowly, because dynamical friction transfers their kinetic energy to the smaller bodies. The simulation maintains a nearly constant ratio of vertical to horizontal velocity, $v_i/h_i \approx 0.53$, for all but the most massive bodies, which have $v_i/h_i < 0.5$. The equilibrium ratio of v_i/h_i yields $\langle i \rangle / \langle e \rangle \approx 0.6$, in agreement with Barge & Pellat (1990, 1991; see also Hornung *et al.* 1985). At the conclusion of the simulation, our velocities for small bodies, $h_i \approx 500 \text{ m s}^{-1}$ at $m_i \sim 10^{19}$ g, are roughly 50% larger than those of WS93. Our velocities for large bodies, $h_i \approx 10 \text{ m s}^{-1}$ at $m_i \sim 10^{26}$ g, are roughly 50% smaller than those of WS93. We also fail to reproduce WS93’s abrupt drop in h_i at $\log m_i = 24$. However, these differences – which are independent of δ – have a negligible effect on the final mass distribution and probably result from slightly different algorithms for low velocity collisions.

Gas drag is included in our simulations but has a negligible impact on the evolution. All of the 1 AU models lose $\sim 0.01\%$ of their initial mass over 1.5×10^5 yr. Velocity changes due to gas drag are essentially zero, because the particle masses are so large.

To understand the sensitivity of these results to initial conditions, we consider the growth time of planetesimals from the coagulation equation, equation A4. For most cases of interest, the growth time for bodies with m_i is approximately $\tau \approx n_0/(dn/dt) \propto Ha\Delta a/n_j VF_g(r_i + r_j)^2$, where n_j is the number of lower mass bodies,

V is the relative velocity, F_g is the gravitational focusing factor, r_i and r_j are the radii of particles i and j , and H is the vertical scale height. Collisions between low mass objects are in the high velocity regime, where the gravitational focusing factor is $F_g \approx 1$ and $\tau \propto a^{5/2} \Delta a n_j^{-1} (r_i + r_j)^{-2}$. This growth time is independent of the initial e and i . Gravitational focusing becomes effective in low-velocity collisions of massive objects; the growth time then depends on the initial velocity and is $\tau \propto a^{5/2} \Delta a n_j^{-1} (r_i + r_j)^{-1} V^2$. The extreme sensitivity of the growth time to velocity is the reason why low-velocity planetesimals experience runaway growth in our 1 AU simulations (Wetherill & Stewart 1989; Ida & Makino 1992a, 1992b; Kokubo & Ida 1996; see also WS93 and references therein). We adopt 1000 km as a useful reference radius and write the time for 8 km objects to produce 1000 km objects at 1 AU as (see also Barge & Pellat 1990):

$$\tau \approx \tau_0 \left(\frac{a}{1 \text{ AU}} \right)^{5/2} \left(\frac{\Delta a}{0.17 \text{ AU}} \right) \left(\frac{\rho_0}{3 \text{ g cm}^{-3}} \right)^{1/3} \left(\frac{V_0}{450 \text{ cm s}^{-1}} \right)^2 \left(\frac{6 \times 10^{27} \text{ g}}{M_0} \right). \quad (1)$$

Using our simulations with $\delta = 1.4$, we derive the proportionality constant for this standard case with velocity evolution, $\tau_{0,v} = 10700$ yr, and for a model with no velocity evolution, $\tau_{0,nv} = 3750$ yr. Additional simulations confirm the mass, velocity, and volume dependence of this relation for factor of two variations in a , Δa , ρ_0 , V_0 , and M_0 about the values in Eqn 1 (see also Aarseth *et al.* 1993; Pollack *et al.* 1996).

3. Kuiper Belt Calculations

3.1. Starting Conditions

To choose appropriate constraints on planetesimal simulations in the outer solar system, we rely on observations of other stellar systems and models of the protosolar nebula. First, current data indicate lifetimes of ~ 5 –10 Myr for *typical* gaseous disks surrounding nearby pre-main sequence stars and for the solar nebula (Sargent & Beckwith 1993; Strom *et al.* 1993; Russell *et al.* 1996). We adopt this estimate as a rough lower limit to the formation time scale of KBOs and assume that interactions between gas and planetesimals disappear on a similar time scale, $\tau_g \approx 10$ Myr (see the Appendix, equation A29). Neptune formation places an upper limit on the KBO growth time, because Neptune excites KBOs through gravitational perturbations. Recent calculations suggest Neptune can form in 5–100 Myr (Ip 1989; Lissauer & Stewart 1993; Lissauer *et al.* 1995; Lissauer *et al.* 1996). Once formed, Neptune inhibits KBO formation at 30–40 AU by increasing particle random velocities on time scales of 20–100 Myr (Holman & Wisdom 1993; Duncan *et al.* 1990). We thus adopt 100 Myr as a rough upper limit to the KBO formation time scale at 30–40 AU.

We assume a wide range of starting conditions for KBO simulations. Our model annulus is centered outside the orbit of Neptune at 35 AU and has a width of 6 AU. This annulus can accommodate at least 10–100 isolated bodies¹ with $m_i \gtrsim 10^{24}$ g for $e \leq 0.01$. The simulations begin with N_0 bodies of radius r_0 , with $r_0 = 80$ m, 800 m, and 8 km. These bodies have small initial eccentricities, $e \sim 10^{-3}$ to 10^{-2} (Malhotra 1995), and an equilibrium ratio of inclination to eccentricity, $\beta = \langle i \rangle / \langle e \rangle = 0.6$ (Barge & Pellat 1990, 1991, 1993). The mass density of each body is fixed at 1.5 g cm⁻³. To set N_0 , we extend the minimum mass solar nebula to the Kuiper Belt and integrate the surface density distribution for solid particles, $\Sigma = \Sigma_0 (a/a_0)^{-3/2}$, across the 6 AU annulus. The dust mass is then $M_{min} \approx 0.25 \Sigma_0 M_{\oplus}$ at 32–38 AU ($a_0 = 1$ AU). Most minimum mass solar nebula models have $\Sigma_0 = 30$ – 60 g cm⁻², which sets $M_{min} \approx 7$ – $15 M_{\oplus}$ (Weidenschilling 1977; Hayashi 1981; Bailey 1994). We thus consider models with initial masses of $M_0 = 1$ – $100 M_{\oplus}$ to allow for additional uncertainty in Σ_0 . Table 1 compares input parameters for all Kuiper Belt models with initial conditions at 1 AU (see also WS93). Tables 4–5 summarize other initial conditions and results for the Kuiper Belt simulations summarized below.

Our success criteria are based on direct observations of KBOs. The present day Kuiper Belt contains at least 70,000 objects with diameters exceeding 100 km at 30–50 AU (Jewitt & Luu 1995, Jewitt *et al.* 1996). This population is some fraction of the initial Kuiper Belt population, because Neptune has eroded the Kuiper Belt over time (Holman & Wisdom 1993; Duncan *et al.* 1990). Thus, a successful KBO simulation must achieve $r_5 \gtrsim 50$ km in $\lesssim 100$ Myr, where r_5 is the radius where the cumulative number of objects exceeds $N_C \geq 10^5$. Pluto formation is our second success criterion: plausible models must produce 1 or more objects with maximum radius $r_{max} \geq 1000$ km. In models with velocity evolution, we end simulations at 100–200 Myr or when r_{max} exceeds ~ 1000 km. To evaluate the dependence of runaway growth on the initial conditions, we extend simulations without velocity evolution to 5000 Myr or to when r_{max} exceeds ~ 2000 km.

3.2. Models Without Velocity Evolution

To isolate important processes in trans-Neptunian planetesimal evolution, we begin with constant velocity solutions to the coagulation equation. We ignore fragmentation and fix the velocities for all masses at $h_i = 4.0 e_{init}$ km s⁻¹ and $v_i = 3.6 \sin i_{init}$ km s⁻¹. The initial eccentricity and inclination are set at $i_{init} = 0.60 e_{init}$. The total mass and kinetic energy remain constant throughout the calculation. We also adopt a coarse mass spacing

¹ “Isolated bodies” are planetesimals that cannot collide with one another, as defined in the Appendix following Eqn (A5)

factor, $\delta = 1.4$. This choice limits our ability to follow runaway growth with high accuracy during the late stages of the simulation but allows us to investigate a wide range of initial masses and velocities with a modest investment of computer time. Finally, we adopt simple formulae for gravitational focusing to speed our calculations (see equation A18; Spaute *et al.* 1991). Table 4 summarizes the initial conditions and results for models with $M_0 = 1\text{--}100 \text{ M}_\oplus$ and $e_{init} = 10^{-3}$ and 10^{-2} .

Figure 3 shows how N_C evolves with time for a model with an initial planetesimal radius $r_0 = 8 \text{ km}$, total mass $M_0 = 10 \text{ M}_\oplus$, and $e_{init} = 10^{-3}$. This model begins with 1.87×10^{10} initial bodies and produces $\sim 42,500$ objects with twice the initial mass after $\tau = 100 \text{ yr}$. Roughly half of the original population experiences at least one collision by $\tau \approx 16 \text{ Myr}$, when the 17 largest bodies have $m_i \approx 10^{20} \text{ g}$. Slow growth continues until $\tau \approx 59 \text{ Myr}$ when the 3 largest objects have sizes comparable to large KBOs, $r_i \approx 100 \text{ km}$ and $m_i \approx 10^{22} \text{ g}$. The growth rate of the large masses then increases considerably due to gravitational focusing. Runaway growth ensues. The cumulative mass distribution then follows a power law, $N_C \propto r_i^{-2.75}$, at low masses and develops a high mass shoulder that extends to larger and larger masses as the simulation proceeds. This shoulder resembles the runaway plateau observed in 1 AU models but does not evolve into a true plateau with $N_C \approx \text{constant}$ as in Figs. 1–2. The largest planetesimals reach $r_{max} \approx 200 \text{ km}$ at $\tau \approx 66 \text{ Myr}$; r_{max} exceeds 1000 km only 9 Myr later. A single runaway body with $r_{max} \approx 4000 \text{ km}$ begins to sweep up lower mass planetesimals at $\tau \approx 80 \text{ Myr}$; by $\tau \approx 85 \text{ Myr}$, it contains essentially all of the mass in the annulus.

Simulations with $r_0 = 8 \text{ km}$ produce runaway growth independent of the initial mass in the annulus. Figure 4(a) indicates that each model experiences a long, linear growth phase until $r_{max} \approx 100\text{--}200 \text{ km}$. The largest objects then begin a short, rapid growth phase that produces several isolated, runaway bodies with $r_{max} \approx 1000 \text{ km}$. These runaway bodies accumulate all of the lower mass bodies and may merge to form a single runaway body if the isolation criterion permits. The time to produce runaway bodies with $r_i = 1000 \text{ km}$ scales with the mass in the annulus, $\tau_r \approx 753 \text{ Myr} (M_0/1 \text{ M}_\oplus)^{-1}$. For comparison, our scaling relation in Eqn (1) predicts $\tau_r \approx 775 \text{ Myr} (M_0/1 \text{ M}_\oplus)^{-1}$ for $\rho_0 = 1.5 \text{ g cm}^{-3}$ in a 6 AU annulus centered at 35 AU.

Runaway growth also occurs independent of the initial radius, r_0 (Figures 4(a)–4(c)). Due to smaller initial cross-sections, models with $r_0 = 80\text{--}800 \text{ m}$ take longer to reach the rapid growth phase. These models make the transition from rapid growth to runaway growth more quickly, because it is easier for 100+ km objects to sweep up small objects with $r < 1 \text{ km}$. In all cases, a single runaway body with $r > 1000 \text{ km}$ eventually accumulates all of the mass in each simulation, although the time scale is quite long, $\tau_r \approx 2700 \text{ Myr}$, for simulations with $M_0 = 1 \text{ M}_\oplus$ and $r_0 = 80 \text{ m}$. Again, the runaway growth time scales with mass: $\tau_r \approx 2340 \text{ Myr} (M_0/1 \text{ M}_\oplus)^{-1}$ for $r_0 = 800 \text{ m}$ and $\tau_r \approx 2700 \text{ Myr} (M_0/1 \text{ M}_\oplus)^{-1}$ for

$r_0 = 80$ m. The small increase in τ_r with initial radius for $r_0 \lesssim 800$ m suggests that models with $r_0 < 80$ m will reach runaway growth on time scales of ~ 3000 Myr, which is ~ 40 times slower than models with $r_0 = 8$ km.

Our results also confirm the velocity dependence derived in Eqn (1). Low eccentricity simulations with 50% smaller initial velocities reach runaway growth in 25% of the time for our standard model; simulations with twice the initial velocity require four times as long to achieve runaway growth. This simple relation begins to break down as the eccentricity increases to $e \approx 10^{-2}$, as outlined below. The runaway time also scales with the width of the annulus, Δa , and the semi-major axis, a , as indicated in equation (1).

High eccentricity models also achieve runaway growth but do not follow precisely the velocity scaling in Eqn (1). Figure 5 shows the radius evolution for models with various r_0 and m_0 for $e = 10^{-2}$ (see also Table 4). The growth time for 1000+ km objects is $\tau_r \approx 20\text{--}25$ Gyr $(M_0/1 \text{ M}_\oplus)^{-1}$ nearly independent of the initial radius and velocity. This relation contrasts with the low eccentricity results, where the growth time is very sensitive to the initial conditions. In all of our simulations, planetesimal growth is orderly until gravitational focusing becomes important and runaway growth occurs. However, the radius where gravitational focusing becomes important increases from $r_i \sim 10$ km at $e = 10^{-3}$ to $r_i \sim 100$ km at $e = 10^{-2}$. For models with small initial bodies, $r_0 \lesssim 800$ m, the time scale to reach runaway growth is directly proportional to e . For models with large initial eccentricity, the long orderly phase also “erases” memory of the initial radius. Thus, τ_r is nearly independent of r_0 for large e . The relatively short orderly growth phase of low e models does not erase memory of r_0 ; τ_r decreases with increasing r_0 for $e_{\text{init}} \lesssim 0.05$. For models with $r_0 \sim 8$ km, gravitational focusing accelerates growth immediately at low e . These simulations do not have an orderly growth phase; instead, they follow the 1 AU simulations and satisfy the scaling relation in Eqn (1).

Before we consider Kuiper Belt simulations with velocity evolution, our basic result that constant velocity models achieve runaway growth deserves some comment. First, previous simulations at 1 AU show that runaway growth requires dynamical friction to decrease the velocities of the largest bodies to the regime where gravitational focusing becomes important (Wetherill & Stewart 1989, 1993; Barge & Pellat 1990, 1991; Ida 1990; Ida & Makino 1992a, 1992b; Ohtsuki 1992; Kokubo & Ida 1996). In Kuiper Belt models with $e_{\text{init}} = 10^{-3}$, gravitational focusing factors become very large at planetesimal masses of 10^{23} to 10^{24} g. Further growth of these bodies only enhances gravitational focusing, because the escape velocity increases while the impact velocities remain low. More massive objects thus “run away” from their lower mass counterparts. This response occurs in *any* constant velocity simulation as long as bodies can reach masses where the escape velocity is large compared to the relative impact velocity, $V_{e,ij}/V_{ij} \gg 1$. Models with $e_{\text{init}} \gtrsim 0.1$ never reach this limit for plausible M_0 and thus do not experience runaway growth. Models with

$e_{init} \lesssim 0.05$ always produce runaway bodies, albeit at much later stages than models with $e_{init} \sim 10^{-3}$ (Figure 5).

Our final comment on runaway growth concerns the shape of the cumulative number distribution near the end of the simulation. During runaway growth, models at 1 AU develop a plateau in the cumulative number distribution that extends from $m_i = 10^{23}$ g to $m_i = 10^{25}$ to 10^{26} g (see Figures 1–2). This plateau separates runaway bodies from the lower mass objects which are in the orderly growth regime and have a power law size distribution, $N_C \propto r_i^{-3}$ for $\log m_i = 21\text{--}24$ (WS93; see Figures 1–2). The Kuiper Belt simulations also produce a power law size distribution, $N_C \propto r_i^{-2.7}$ for $m_i \lesssim 10^{25}$ g, but they develop a high mass “shoulder” instead of a marked plateau at runaway growth (see Figure 3). To test if this feature is a function of the mass resolution as in 1 AU models, we simulate evolution at 35 AU with $\delta = 1.1$ and 1.25 for $M_0 = 10 M_\oplus$ and $r_0 = 8$ km. As the mass resolution in the simulation increases from $\delta = 1.4$ to $\delta = 1.1$, the high mass shoulder follows a very shallow power law, $N_C \propto r_i^{-1.7}$ (Figure 6). This power law becomes better defined as the mass resolution increases further, but it never develops into the “runaway plateau” produced in the 1 AU models (Figures 1–2). This result suggests that the broad plateau in 1 AU models is the result of velocity evolution, which reduces the velocity of the most massive objects and enhances gravitational focusing (WS93). We will now test this hypothesis by considering Kuiper Belt models with velocity evolution.

3.3. Models with Velocity Evolution

To understand the importance of velocity evolution in the Kuiper Belt, we add several physical processes to the calculation: (i) gas drag, (ii) dynamical friction and viscous stirring from long-range (elastic) collisions, and (iii) dynamical friction and viscous stirring from short-range (inelastic) collisions. As in our constant velocity models, we begin with N_0 bodies at radii, $r_0 = 80$ m, 800 m, and 8 km. We adopt $\delta = 1.4$ for the mass spacing factor and use our simple expression for gravitational focusing, Eqn A18. The initial velocities are $h_i = 4.0 (e_{init}/10^{-3})$ m s $^{-1}$ and $v_i = 2.1 (e_{init}/10^{-3})$ m s $^{-1}$. The eccentricity and inclination evolve separately due to collisions and collective interactions (see section A.3 of the Appendix). Table 5 summarizes the initial conditions and results for models with $M_0 = 1\text{--}30 M_\oplus$ and $e_{init} = 10^{-3}$ to 10^{-2} .

Before describing the results of our simulations, it is useful to compare various time scales for velocity evolution at 35 AU. First, gas drag is negligible in models that ignore fragmentation. A typical simulation at 35 AU loses $\sim 10^{-5}\%$ of its total mass due to gas drag in 100 Myr. Velocity changes due to gas drag are also insignificant; the time scale for gas drag to modify the velocity exceeds 10 Gyr for all masses in our simulation.

Velocity changes due to elastic and inelastic collisions, however, are significant. Figure

7(a) compares time scales, $\tau_{v,h} = h_i/(dh_i/dt)$, for horizontal velocity evolution as a function of particle mass at 35 AU. The two curves show $\tau_{v,h}$ for interactions between particles of the same mass with a power-law size distribution, $N_C \propto r^{-2.7}$, and constant velocity. These time scales are *not* integrated over the size distribution and are relevant only when a simulation has a small range of masses. Viscous stirring – which tends to increase particle velocities – is ineffective for $m_i \lesssim 10^{13}$ kg, $\tau_{v,h} \approx 10^{16}$ yr, but very effective, $\tau_{v,h} \lesssim 10^6$ yr, at $m_i \gtrsim 10^{17}$ kg. Collisional damping is also more effective at large masses, but the time scale is much less mass-sensitive than viscous stirring. Collisional damping balances viscous stirring for an initial particle mass, $m_0 \approx 10^{15}$ kg, which corresponds to $r_0 \approx 5$ km.

To illustrate these points in more detail, Figures 7(b) and 7(c) plot the *integrated* time scales, $\tau_{v,h} = \sum_{i=1}^N h_i/(dh_i/dt)$, for the horizontal velocity at two stages of a model with velocity evolution. In Figure 7(b), the maximum mass has $m_{max} \approx 10^{14}$ kg. Collisional damping still dominates viscous stirring for the lowest masses, but the mass where the two processes balance has moved from $m_i \approx 10^{15}$ kg to $m_i \approx 5 \times 10^{11}$ kg. Once $m_{max} \approx 10^{19}$ kg, viscous stirring dominates collisional damping for all masses. Particle velocities thus increase once massive objects with $r_i \gtrsim 100$ km are produced. The time scale for viscous stirring is quite short, $\lesssim 10^6$ yr, at the lowest masses considered in our models, so the velocity increases can be large during the 100 Myr time scale of a typical simulation.

Figure 8 shows how N_C and h_i evolve with time in a model with $r_0 = 8$ km, $M_0 = 10 M_\oplus$, and $e_{init} = 10^{-3}$. The simulation begins with $N_0 = 1.87 \times 10^{10}$ and produces 762 objects having eight times the initial mass in 1 Myr. Roughly half of the initial bodies experience at least one collision by 24 Myr, when the largest object has $r_{max} \approx 37$ km. The horizontal velocities then range from $h_i = 1$ m s⁻¹ at $r_i = 37$ km up to $h_i = 7$ m s⁻¹ at $r_i = 8$ km. Orderly growth produces $r_i = 100$ km objects at 56 Myr, and this population reaches $N_C \approx 100$ at 61 Myr. This phase continues until ~ 100 Myr, when Charon-sized objects with $r_i \approx 500$ km begin to grow rapidly. There are 10 “Charons” at 110 Myr, 47 “Charons” at 125 Myr, 107 “Charons” at 150 Myr, and 202 “Charons” at 180 Myr when we ended the simulation. At 180 Myr, 20 Pluto-sized objects with $r_i \approx 1000$ km are isolated bodies about to run away from the rest of the mass distribution.

In contrast to the constant velocity simulations with low e_{init} , this model does not immediately enter a rapid growth phase once objects with $r_i \approx 100$ km are first produced. Viscous stirring and dynamical friction slowly increase the velocities of low mass bodies throughout the simulation: the horizontal velocity increases from $h_{init} = 4$ m s⁻¹ to $h_i \approx 65$ m s⁻¹ at 180 Myr (Figure 8). This twentyfold increase in the eccentricity reduces gravitational focusing by a factor of 400 and retards the growth of the most massive objects. Evolution thus proceeds at a pace between the constant velocity simulations with $e_{init} = 10^{-3}$ and $e_{init} = 10^{-2}$.

The evolution for simulations with smaller initial masses is different, because collisional

damping then dominates the velocity evolution (Figure 7). Figure 9 shows the time evolution of N_C and h_i for $r_0 = 800$ m, $M_0 = 10 M_{\oplus}$, and $e_{init} = 10^{-3}$. This simulation begins with $N_0 = 1.87 \times 10^{13}$ and produces five objects having eight times the initial mass in 1 Myr. It takes only 7.7 Myr for half of the initial objects to collide at least once. The maximum radius is then $r_{max} \approx 2.5$ km. Velocity damping from inelastic collisions overcomes viscous stirring, so the particle velocities remain low and do not change significantly with mass. As evolution proceeds, dynamical friction efficiently damps the velocities of the largest bodies, but collisional damping still maintains modest velocities at low masses. Bodies with $r_i = 8\text{--}10$ km begin to form at 32–33 Myr, when only 11% of the original objects remain. The evolution soon overtakes the $r_0 = 8$ km model. Orderly growth produces 50 km objects at 45 Myr and 100 km objects at 48 Myr. Runaway growth begins shortly thereafter. Charon-sized objects form at 60 Myr and reach Pluto-size at 80–81 Myr.

Simulations with $r_0 = 80$ m reach runaway growth on even faster time scales. Figure 10 shows the time evolution of N_C and h_i for $M_0 = 10 M_{\oplus}$ and $e_{init} = 10^{-3}$. At 1 Myr, only 43% of the initial bodies have yet to experience a collision; 33 objects already have $r_i \approx 270$ m. The maximum radius reaches $r_{max} = 800$ m in 9 Myr and $r_{max} = 8$ km in 17 Myr. The low mass bodies first lose $\sim 50\%$ of their initial velocity, $h_{init} = 4 \text{ m s}^{-1}$, and begin to increase in velocity at 17–18 Myr when viscous stirring from long-range collisions finally overcomes damping from inelastic collisions. At this time, the high mass bodies have low velocities due to dynamical friction, $h_i \approx 0.01 \text{ m s}^{-1}$, and begin to grow rapidly. A runaway plateau in the N_C distribution develops at 24 Myr and extends to Charon-sized objects at 25 Myr. At the conclusion of this simulation at 33 Myr, five Pluto-sized objects have $r_i \approx 900\text{--}1000$ km. The velocities of these high mass objects are then $h_i \approx 0.03\text{--}0.05 \text{ m s}^{-1}$.

With their long runaway growth times, models with $r_0 = 8$ km cannot meet both of our success criteria unless the initial mass is very large, $M_0 \gtrsim 15\text{--}20 M_{\oplus}$. Viscous stirring and dynamical friction increase the velocities of the small objects throughout these simulations, which reduces gravitational focusing and delays runaway growth compared to models with smaller r_0 . The long approach to runaway growth allows the production of many large KBO's; simulations with $M_0 \approx 6\text{--}20 M_{\oplus}$ have $r_5 \approx 50\text{--}100$ km and thus reach our first success criterion. However, the time scale to produce 1000+ km objects is 4–5 times longer than models with $r_0 = 80$ m, i.e., $\tau_r \approx 130$ Myr $(M_0/10 M_{\oplus})^{-1}$. Most of these models thus fail to make Pluto on a reasonable time scale.

Models starting with lower mass objects, $r_0 = 80$ m and 800 m, meet both success criteria. Although viscous stirring and dynamical friction stir up the velocities of the lowest mass objects, the time scale for the velocity to increase is large compared to models with $r_0 = 8$ km (see Figure 7). The $r_0 = 800$ m models reach runaway growth faster than models with $r_0 = 8$ km and produce Pluto-sized objects in $\tau_r \approx 83$ Myr $(M_0/10 M_{\oplus})^{-1}$ for $e_{init} = 10^{-3}$. The combination of smaller particle velocities and a shorter time to runaway growth

results in fewer KBOs compared to models with $r_0 = 8$ km. Nevertheless, these models achieve $r_5 \approx 50\text{--}90$ km during the runaway growth phase.

Models with $r_0 = 80$ m and $e_{init} = 10^{-3}$ have the shortest runaway growth times and produce the fewest numbers of KBOs. The time scale to produce Pluto-sized planets is $\tau_r \approx 32$ Myr $(M_0/10 M_\oplus)^{-1}$ for $e_{init} = 10^{-3}$, which easily allows Pluto formation in a minimum mass solar nebula as Neptune forms at a smaller semi-major axis. These models, however, struggle to build a population of 10^5 KBOs during the runaway growth phase. With relatively low particle velocities at all masses (see Figure 10b), objects with $r_i \approx 10\text{--}20$ km do not grow as rapidly as larger bodies. This evolution tends to concentrate material in the more massive KBOs and reduces the number of lower mass KBOs with $r_i \approx 50\text{--}100$ km. This smaller r_5 in the calculations leads to partially-successful models that yield several Pluto-sized objects and $r_5 \lesssim 50$ km (Table 5).

At large initial eccentricity, planetesimal growth follows the evolution of low eccentricity models but on longer time scales (Figure 12). In simulations with $r_0 = 80$ m and 800 m, there are enough small bodies for inelastic collisions to damp the particle velocities substantially. Dynamical friction further decreases the velocities of the most massive bodies and allows runaway growth to occur on reasonable time scales. In simulations with $r_0 = 80$ m and $e_{init} = 10^{-2}$, runaway growth is delayed by a factor of ~ 2.5 compared to simulations with $e_{init} = 10^{-3}$. This delay increases to a factor of ~ 3 for $r_0 = 800$ m. At $r_0 = 8$ km, collisional damping initially reduces particle velocities but is overcome by viscous stirring when $r_{max} \approx 50$ km. At this time, the velocities are large, $V_i \approx 30$ m s $^{-1}$, and growth is slow. None of these models reach runaway growth on a 100 Myr time scale. Runaway growth, if it occurs, is delayed by a factor of ~ 6 in large e_{init} models compared to that in low e_{init} models.

Our results for large e_{init} thus favor low mass initial bodies. Simulations with $r_0 = 80$ m and $e_{init} = 10^{-2}$ produce more KBOs with $r_i \approx 50\text{--}100$ km than their low e_{init} counterparts. The longer orderly growth phase and somewhat larger particle velocities at the onset of runaway growth favor the growth of 50–100 km objects. The r_5 for these mass distributions is 10% to 20% larger than the r_5 for low e_{init} ($r_5 \approx 50\text{--}90$ km for $e_{init} = 10^{-2}$ compared to $r_5 \approx 50\text{--}75$ km for $e_{init} = 10^{-3}$). Models with larger r_0 are less successful. For $r_0 = 800$ m, runaway growth begins well after 100 Myr unless $M_0 \gtrsim 20\text{--}30 M_\oplus$. Runaway growth always occurs on a very long time scale, $\gtrsim 150\text{--}200$ Myr, for $r_0 = 8$ km and $M_0 \lesssim 30 M_\oplus$.

Unlike the constant velocity models, simulations with velocity evolution begin to develop a “runaway plateau” in the cumulative mass distribution when $r_{max} \gtrsim 500$ km (see Figures 8–10). In constant velocity simulations, we found two power law cumulative mass distributions, $N_C \propto r^{-2.75}$ at low masses and $N_C \propto r^{-1.75}$ at large masses. The total mass per mass batch is then roughly constant at low masses and increases slowly with mass at

large masses. In models *with* velocity evolution, dynamical friction reduces the velocities of the largest bodies to $V_i \lesssim 0.1 \text{ m s}^{-1}$ and maintains velocities of $V_i \sim 1\text{--}10 \text{ m s}^{-1}$ for smaller objects with $r_i \lesssim 10 \text{ km}$. As noted by WS93, the increase in the escape velocity with mass coupled with the decrease in V_i produce substantial increases in the collisional cross-sections (see also Wetherill & Stewart 1989; Barge & Pellat 1990, 1991, 1993; Ida & Makino 1992a, 1992b, Ohtsuki 1992; Kokubo & Ida 1996). In our models, the velocity distribution resembles a step function and produces a step-like increase in the gravitational focusing factors, from $F_g \sim 10\text{--}100$ at $r_i \sim 10\text{--}100 \text{ km}$ up to $F_g \sim 10^4$ at $r_i \sim 300\text{--}1000 \text{ km}$. Runaway growth then converts the $N_C \propto r^{-1.75}$ mass distribution into $N_C \approx \text{constant}$, because objects with $r_i \sim 100\text{--}200 \text{ km}$ grow too slowly to fill in the power law as objects with $r_i \gtrsim 500 \text{ km}$ run away. At low masses, the size distribution remains a power law, $N_C \propto r^{-2.75}$, because runaway growth does not change the size distribution significantly.

To conclude this section, Figure 13 summarizes results for accretional evolution in the Kuiper Belt with velocity evolution and no fragmentation. Successful simulations that produce $\sim 10^5$ KBOs and a few Pluto-sized objects on time scales of 100 Myr or less have initial masses somewhat larger than that predicted for a minimum mass solar nebula extrapolated into the Kuiper Belt, $M_0 \gtrsim 10 \text{ M}_\oplus$, and bodies with initial radii of $r_0 \approx 80 \text{ m}$ to 8 km . Simulations with small initial bodies, $r_0 = 80 \text{ m}$, tend to produce fewer KBOs than simulations with larger initial bodies, $r_0 = 800 \text{ m}$ and 8 km . This feature of our calculations results in partially-successful models that produce Pluto-sized objects but too few KBOs in 100 Myr. In models with $M_0 \approx 6 \text{ M}_\oplus$ and $r_0 = 80 \text{ m}$, runaway growth removes KBOs from the mass distribution more rapidly than they are produced from lower mass objects. This evolution does not occur in models with larger initial bodies, because collisional damping is less effective at “circularizing” the orbits during the orderly growth phase. The higher particle velocities in these models allows formation of more KBOs during the runaway growth of Charon-sized objects.

Collisional evolution often fails to produce 100+ km objects on any useful time scale. Simulations with $M_0 \approx 1\text{--}6 \text{ M}_\oplus$ produce neither Pluto-sized objects nor a substantial number of 100+ km KBOs in 100 Myr. Large initial eccentricities exacerbate this problem for models with $r_0 \gtrsim 800 \text{ m}$, because collisional damping cannot reduce the particle velocities before 100+ km objects form. These simulations can produce KBOs and Plutos on longer time scales, 100–1000 Myr, in systems where a Neptune-sized object does not constrain the formation time. Extrapolating our results to smaller initial masses, simulations with $M_0 \lesssim 0.1 \text{ M}_\oplus$ fail to produce KBOs during the age of the solar system, $\sim 5 \text{ Gyr}$.

3.4. Limitations of the Models

Statistical simulations of planetesimal growth have well-documented approximations and uncertainties. The model assumes a homogeneous spatial distribution of planetesimals whose velocities are small compared to the orbital velocity. These assumptions are good during the early stages of planetesimal evolution. As planetesimals grow, dynamical friction can reduce the velocities of high mass objects below limits where the statistical approach is valid (Barge & Pellat 1990). Once this limit is reached, runaway growth produces a few large bodies that are not distributed homogeneously in space (WS93; Kokubo & Ida 1996). These large bodies can then pump up the velocities of the smallest bodies on short time scales through viscous stirring (Figure 7). We end the simulations with velocity evolution during the runaway growth stage when the basic assumption of a homogeneous distribution of planetesimals begins to break down. The velocities of low mass bodies remain small compared to the Keplerian velocity, but the most massive objects often have velocities below the low velocity limit of the kinetic approximation. We will discuss this problem below.

The remaining limitations of the statistical approach involve our implementation of standard algorithms. We adopt a single accumulation zone and thus cannot follow the evolution in semi-major axis of a planetesimal swarm (see Spaute *et al.* 1991). We use a coarser grid than some simulations, but this choice has little impact on the results at 35 AU. At 1 AU, the lag of simulations with $\delta > 1.1$ relative to a simulation with $\delta = 1.1$ increases with increasing δ ; we find a 12% lag for $\delta = 1.4$ but only a 2–3% lag for $\delta = 1.25$. At 35 AU, the lag in runaway growth relative to a $\delta = 1.1$ model increases from 4%–5% for $\delta = 1.4$ to 10%–15% at $\delta = 2$. Our $\delta = 1.4$ simulations thus overestimate the runaway growth time only by 4–5% (see also Wetherill 1990; Kolvoord & Greenberg 1992). This error is small compared to other uncertainties in the calculation.

Our choice of the initial mass distribution has a modest impact on our results. We calculated the evolution of several size distributions with equal mass per mass batch for $r_{min} \lesssim r_i \lesssim r_{max}$. Simulations with $r_{min} \sim 100$ –1000 m and $r_{max} \lesssim$ a few km are nearly indistinguishable from simulations with a single starting radius, $r_0 \approx r_{max}$. In these models, collisional damping effectively reduces all particle velocities as described above and allows runaway growth to occur. Simulations with large $r_{max} \approx 8$ km are similar to those with a single starting mass, unless r_{min} is small. For $r_{min} \lesssim 800$ m, collisional damping keeps the particle velocities small compared to models with a single starting mass. Runaway growth occurs in these models, but the time scale to runaway is sensitive to r_{min} . We plan to explore this sensitivity in more detail when we include fragmentation in the calculation.

The most uncertain approximation in our calculations is the treatment of low velocity collisions. During the late stages of most simulations, the massive bodies have very low velocities and very large gravitational ranges. The velocities are often smaller than the Hill

velocity, V_H , which invalidates the basic assumptions for our velocity evolution calculations (Barge & Pellat 1990, 1991, 1993). Barge & Pellat (1990) and WS93 have developed different approximations to low velocity collisions based on Ida's (1990) n -body simulations (see also Ohtsuki 1992). We note that these two approximations produce different velocities for high mass planetesimals, which we plan to examine in more detail when we include fragmentation in our calculations. The mass evolution of runaway bodies is not affected by our treatment of velocity evolution in the low velocity regime.

The large gravitational ranges of the most massive bodies also invalidate the standard treatment of collisions. We use the WS93 prescription for isolating the largest bodies from collisions with one another and adopt the Greenberg *et al.* (1992) approach to low velocity collisions in the two-dimensional regime. Removing the isolation criteria allows the largest body to grow more rapidly than the isolated bodies and reduces the time scale to runaway growth by 5%–10%. Removing the Greenberg *et al.* (1992) two-dimensional cross-sections has no substantial effect on our results.

Aside from fragmentation, we have included all important physical processes in planetesimal evolution. Our neglect of fragmentation, however, is a serious limitation. In previous simulations, fragmentation of relatively strong bodies with $r_i \gtrsim 1$ –10 km produces a significant amount of cratering debris that can be accumulated later by runaway bodies (e.g., WS93; Barge & Pellat 1993). This process usually becomes important only in the late stages of calculations at 1 AU: it slows growth during early stages but speeds up runaway growth later in the evolution (Barge & Pellat 1993; WS93). However, collisions between very weak bodies can disrupt and thereby prevent *any* growth of icy planetesimals at modest velocities. The importance of fragmentation at $a \approx 35$ AU thus depends on the unknown strength of KBOs.

We can estimate the importance of fragmentation in Kuiper Belt simulations using Barge & Pellat's (1993) results for a reasonable fragmentation model. They adopt the Housen *et al.* (1991) energy prescription for planetesimal disruption and derive collisional outcomes for several test cases. These results are most appropriate for rocky asteroids, but it is straightforward to scale them to the weaker, icy bodies that might exist at 35 AU. We consider the two cases recently adopted by Stern & Colwell (1997): strong, rocky KBOs and weak, icy KBOs.

Fragmentation does not significantly change our main conclusions if KBOs are strong objects. According to Figure 5 of Barge & Pellat (1993), fragmentation modifies the growth of 10 km bodies only when $e \gtrsim e_{crit} \approx 0.025$. The critical eccentricity for fragmentation decreases to $e_{crit} \approx 10^{-2}$ for 1 km objects and $e_{crit} \approx 2 \times 10^{-3}$ for 0.1 km objects (see also Fig. 1 of Stern 1996). Our low e simulations never reach these critical values. Fragmentation is important in large e simulations, but most of these models do not produce KBOs on a reasonable time scale.

The growth of icy KBOs is probably very sensitive to the time scale for velocity evolution. We expect fragmentation to dominate the early evolution of all simulations considered above, because only objects with $r_i \gtrsim 20\text{--}30$ km can survive collisions and produce larger bodies (see also Stern & Colwell 1997). As the evolution proceeds, however, inelastic collisions should damp the velocities of bodies with $r_i \lesssim 1$ km, while dynamical friction damps the velocities of the most massive objects (see Figure 7). These damping time scales are short compared to the viscous stirring time scales, so the particle velocities decrease on relatively short time scales, ~ 10 Myr. This damping is probably sufficient to allow the growth of 1–10 km objects on time scales similar to those found in our models without fragmentation. Smaller bodies may not grow unless dynamical friction is very efficient. We will explore this possibility in our second paper.

4. DISCUSSION AND SUMMARY

We have developed a time-dependent planetesimal evolution program similar to the WS93 code used to simulate the formation of terrestrial embryos from small bodies. The program incorporates coagulation with realistic cross-sections and velocity evolution using the statistical formulation of Barge & Pellat (1990, 1991; see also Hornung *et al.* 1985). Our numerical solutions to the coagulation equation agree with analytical solutions for three standard test cases. Our results also agree with WS93’s simulation of the formation of the Earth at 1 AU. The present models do not incorporate fragmentation of bodies during collisions. We will include fragmentation in a separate paper.

We have considered two simple cases of planetesimal evolution in a 6 AU wide annulus centered at 35 AU. Models without velocity evolution invariably produce several large bodies that accrete practically all of the material in the annulus. The runaway growth in these simulations occurs without dynamical friction or gas drag; it is a direct consequence of gravitational focusing. The time required to produce a runaway body in our models scales inversely with the initial mass of the annulus *and* with the initial radii and velocities of the planetesimals. For bodies with $r_0 = 80\text{--}8000$ m and $e_{init} = 10^{-3}$, our simulations produce runaway growth in 100 Myr for annular masses of roughly $10\text{--}30 M_{\oplus}$. The time scale for runaway growth increases to 700–2000 Myr for $e = 10^{-2}$. A minimum mass solar nebula with $\Sigma \propto R^{-3/2}$ contains $7\text{--}15 M_{\oplus}$ in a 6 AU wide annulus centered at 35 AU. These models thus reach runaway growth in a minimum mass nebula on time scales comparable to the maximum formation time scale for Neptune ($\sim 50\text{--}100$ Myr, Lissauer *et al.* 1996; Pollack *et al.* 1996). Runaway growth on much shorter time scales, ~ 10 Myr, requires annular masses that far exceed the minimum mass solar nebula, $\sim 100 M_{\oplus}$ in a 6 AU wide annulus for $e_{init} = 10^{-2}$ to 10^{-3} .

Models with velocity evolution produce runaway growth on a much wider range of time

scales compared to constant velocity calculations. First, dynamical friction and viscous stirring dominate the evolution of models with relatively large (8 km) initial bodies. The velocities of these bodies thus increase as collisions produce more massive objects. This velocity increase delays runaway growth by factors of 2 or more compared to constant velocity evolution. The delay in the runaway growth time increases with increasing e_{init} . In contrast, collisional damping dominates the evolution of models with smaller (80–800 m) initial bodies. These bodies ‘cool’ until the largest objects have radii of 10–20 km. Dynamical friction and viscous stirring then ‘heat up’ the small bodies but this heating is small compared to the velocity increases of the $r_0 = 8$ km models. For $e_{init} = 10^{-3}$, collisional damping enhances collision rates and decreases the time scale to runaway growth by factors of 4–12 compared to constant velocity calculations. Our simulations of minimum mass solar nebulae with $e_{init} = 10^{-3}$ reach runaway growth on time scales of 20–40 Myr for 80 m initial bodies, 50–100 Myr for 800 m bodies, and 75–250 Myr for 8 km bodies. These time scales increase by factors of 2–4 for $e_{init} = 10^{-2}$.

The formation of runaway bodies in constant velocity simulations is surprising. Previous simulations demonstrate a need for dynamical friction, which decreases the velocities of the most massive objects (Wetherill & Stewart 1989, 1993; Barge & Pellat 1990, 1991; Ohtsuki 1992; Ida & Makino 1992a, 1992b; Kokubo & Ida 1996). Gravitational focusing then allows these bodies to sweep up lower mass bodies very rapidly. Kokubo & Ida (1996) summarize necessary and sufficient conditions for runaway growth and show that the ratio of the maximum mass of planetesimals to their mean mass increases dramatically during runaway growth. Our constant velocity simulations satisfy the “necessary” condition for runaway growth,

$$2R_{H,ij}\Omega \lesssim V_{ij} \lesssim V_{e,ij} \quad (2)$$

but do not meet the “sufficient” condition,

$$\frac{dV}{dm} < 0 , \quad (3)$$

because our velocities are constant with mass, $dV/dm = 0$. Nevertheless, the maximum mass, M_{max} , of each constant velocity simulation increases much more rapidly than the mean mass, $\langle m_i \rangle$ (Figure 14). In Figure 14(a), the ratio $M_{max}/\langle m_i \rangle$ increases slowly during the orderly growth phase and then increases rapidly when several isolated bodies begin to accrete most of the mass in the annulus. This runaway growth is not as extreme as that seen in models with velocity evolution. We derive $M_{max}/\langle m_i \rangle \approx 10^6$ in constant velocity models compared to $M_{max}/\langle m_i \rangle \approx 10^8\text{--}10^{10}$ in models with velocity evolution (Figure 14(b)). Dynamical friction is responsible for the larger increase in $M_{max}/\langle m_i \rangle$ in models with velocity evolution.

Although the constant velocity simulations are artificial, they are a useful guide for planetesimal growth in the outer solar system. Our results show that collisional damping by small bodies can overcome viscous stirring and keep particle velocities low at $a = 35$ AU. The relative efficiency of collisional damping should increase with a , because the collision rates decrease more rapidly with a than do the damping rates ($\tau_{coll} \propto a^{-5/2}$ vs. $\tau_{damp} \propto a^{-3/2}$). The situation in the outer solar system differs markedly from conditions at small a . In our simulations at 1 AU, bodies with $r_i \approx 80\text{--}800$ m grow to 10 km objects in ~ 1000 yr. As in the 35 AU simulations described above, collisional damping reduces the velocities of the small bodies by a factor of ~ 2 in 1000 yr. In contrast to our 35 AU models, viscous stirring and dynamical friction act quickly to increase velocities once larger bodies are produced at 1 AU. Aside from the longer time scale to reach runaway growth, this evolution then follows closely the simulations in Figures 1–2.

With these considerations in mind, we suggest a modest modification to the sufficient condition for runaway growth,

$$\frac{dV}{dm} \leq 0 , \quad (4)$$

instead of the condition in Eqn. (3). This condition maintains the relative growth rate necessary for runaway in a three-dimensional system (see Kokubo & Ida 1996)

$$\frac{1}{M} \frac{dm}{dt} \propto M^{1/3} , \quad (5)$$

when the gravitational focusing factor is large (e.g., $V_{ij} \lesssim V_{e,ij}$).

In addition to this new criterion for runaway growth, our simulations show that Neptune and Pluto can grow in parallel at $a \approx 30\text{--}35$ AU. For a minimum mass solar nebula, previous calculations indicate that Neptune reaches its current size in no longer than 50–100 Myr (Ip 1989; Lissauer *et al.* 1996; Pollack *et al.* 1996). In our models of minimum mass solar nebulae at 35 AU, 800 m objects grow to Pluto-sized planets on similar time scales. However, recent observations indicate a much shorter lifetime, $\sim 5\text{--}10$ Myr, for gaseous disks surrounding nearby pre-main sequence stars (Sargent & Beckwith 1993; Strom *et al.* 1993; Russell *et al.* 1996; see also Fernández 1997). If our solar system evolved on a similar time scale, the formation of the gas-rich outer planets requires solar nebulae with masses 2–5 times larger than the minimum mass solar nebula, M_{min} (Lissauer *et al.* 1996; Pollack *et al.* 1996). Neptune then attains its current size in 5–10 Myr. At 35 AU, objects reach 1000 km sizes in 10–20 Myr for $M_0 \approx 2\text{--}3 M_{min}$ and in 5–10 Myr for $M_0 \approx 5 M_{min}$ assuming the initial bodies have small masses and eccentricities. Fragmentation should not change these conclusions unless collisional erosion can prevent the formation of 1 km bodies from smaller building blocks.

Our Kuiper Belt simulation produce Pluto-sized objects on reasonable time scales for other plausible solar nebula models. In particular, Cameron’s (1995 and references therein) detailed disk models for the protosolar nebula have a shallower density distribution, $\Sigma = \Sigma_0(a/a_0)^{-1}$, than the minimum mass model we considered above to derive our success criteria (see also Ruden & Lin 1986; Ruden & Pollack 1991). Cameron’s model contains $\sim 100 M_{\oplus}$ in our 6 AU annulus. The growth time for 1000+ km objects scales simply from results with smaller disk masses. For models with velocity evolution, we estimate $\tau_r \approx 3$ Myr for $r_0 = 80$ m, $\tau_r \approx 8$ Myr for $r_0 = 800$ m, and $\tau_r \approx 15$ Myr for $r_0 = 8$ km. Although all of these models can produce Pluto-sized objects before Neptune reaches its final mass, models with $r_0 = 8$ km produce more KBOs with $r_i \sim 100$ –300 km as outlined in Sec. 3.3.

These results – together with recent dynamical calculations of Malhotra (1993, 1995, 1996) – suggest a self-consistent picture for the formation of Pluto-Charon in the outer solar system. In this picture, Pluto and Charon begin as ~ 1 km planetesimals at $a \sim 35$ –40 AU and grow to their present sizes on a time scale of 10–100 Myr. Both objects are runaway bodies more massive than the bulk of the planetesimal mass distribution and have low velocities due to collisional damping and dynamical friction. At a somewhat smaller semi-major axis, $a \approx 25$ –30 AU, Neptune accretes its current mass in 10–100 Myr and migrates radially outward through the protosolar disk during the late stages of giant planet formation (Malhotra 1993; Pollack *et al.* 1996; Fernández & Ip 1996; see also Ipatov 1989, 1991). During this outward migration, Neptune captures Pluto-Charon in the 3:2 resonance (Malhotra 1995). This capture should effectively end further growth of Pluto-Charon, because the orbital elements increase to $e \sim 0.2$ and $i \sim 10^\circ$ on a short time scale, ~ 10 Myr, inside the resonance (Malhotra 1995). High velocity collisions within the resonance should also hinder growth as in our large e models. Neptune also captures other KBOs at $a \approx 35$ –40 AU into the 3:2 and other resonances (Malhotra 1996; see also Jewitt *et al.* 1996). Further growth of these objects is also slowed due to rapidly increasing velocities (Malhotra 1995, 1996; Morbidelli *et al.* 1995; Davis & Farinella 1997). As long as collisional erosion does not decrease significantly the radii of captured KBOs, this sequence of events accounts for the general aspects of the mass distribution and orbital elements of observed KBOs in a simple way.

This picture for the formation of Neptune, Pluto-Charon, and KBOs differs from those of Stern (1995, 1996) and Stern & Colwell (1997a,b), who studied KBO evolution at 40–70 AU. Stern & Colwell (1997) concluded that the formation of Neptune and KBOs, including Pluto-Charon, requires ~ 100 –1000 Myr due to the low collision rates at $a \approx 30$ –50 AU. Stern & Colwell’s (1997a; also Stern 1995, 1996) time scale for KBO formation is a factor of 10–20 longer than our time scale. Their results also conflict with the more detailed gas dynamic calculations of Pollack *et al.* (1996). Although the exact origin of this discrepancy is unclear, we suspect mass spacing, collision rates, and (less probably) fragmentation may be responsible. Our mass spacing, $\delta = 1.4$, should produce more accurate estimates for

the growth time than $\delta = 2$ (Stern & Colwell 1997) or $\delta = 4$ (Stern 1996). We estimate 10%–20% delays in runaway growth for $\delta = 2$ and expect very long delays for $\delta = 4$. In addition, our collision rates include a factor, β_{coll} , that accounts for the gaussian distribution of impact velocities (Greenzweig & Lissauer 1992; see Eqn. A14). Neglecting this factor delays runaway growth by a factor of 3 (see also WS93). Stern (1995) does not include this factor in his cross-section (see his Eqn. 5) and thus derives much longer growth times. As noted above, our neglect of fragmentation encourages runaway growth. We do not think that including this process should delay runaway growth by another factor of 3, for reasons outlined earlier, and plan to test this suspicion in our next paper.

However the theoretical issues may be resolved, several consequences of our accretion models can be tested with additional observations. All models that reach runaway growth produce 10–100 Pluto-sized objects with radii $r_{max} \approx 1000$ –2000 km and a roughly power-law mass distribution with a maximum radius at ~ 0.1 – $0.2r_{max}$ (see Figures 8–10). If Pluto and Charon are runaway bodies produced at $a \approx 35$ –40 AU, there should be several additional “Plutos” with similar orbital elements. Malhotra (1995) reached a similar conclusion and noted that recent searches have not excluded the possibility of several additional Plutos in 3:2 orbital resonance with Neptune. The accretion models also predict a cumulative power law distribution, $N_C \propto r^{-3}$, for objects with $r \lesssim 100$ –200 km. By analogy with WS93, this shape is fairly independent of fragmentation as long as collisions produce overall growth instead of disruption. The best fit to the observed distribution is shallower than expected, $N_C \propto r^{-2}$, but the data are not yet accurate enough to preclude our model prediction (Jewitt *et al.* 1996). Larger surveys will provide a better test of this prediction (Luu *et al.* 1997).

Finally, our results suggest that KBO formation is likely in other solar systems. KBOs can grow in the dusty disks that surround many nearby main-sequence stars, if the disk masses are within an order of magnitude of the “maximum” disk masses for α Lyr, α PsA, and β Pic (Backman & Paresce 1993). Stars with disk masses near the minimum dust masses of these well-studied A-type stars probably have few, if any, KBOs, but could have many objects with $r_i \sim 1$ –10 km. Observations of nearby pre-main sequence stars also indicate substantial masses, $M_d \gtrsim 10^3 M_\oplus$, in circumstellar disks with radii of 100–1000 AU (e.g., Sargent & Beckwith 1993; see also Beckwith & Sargent 1996). These data imply $M_0 \sim 10$ –100 M_\oplus in the Kuiper Belt. With formation time scales of 1–10 Myr, KBOs can grow in massive circumstellar disks during the pre-main sequence contraction phase of a low mass star (see Kenyon & Hartmann 1995 and references therein). In a less massive disk, KBOs grow while the central star is on the main sequence. We expect no KBO formation in circumstellar disks with very low masses, $M_d \lesssim 10 M_\oplus$. These disks can produce 1–10 km objects at $a \gtrsim 30$ AU, unless fragmentation prevents growth of icy bodies. We will explore this possibility in a subsequent paper.

We thank B. Bromley for making it possible to run our code on the JPL Cray T3D and for a generous allotment of computer time through funding from the NASA Offices of Mission to Planet Earth, Aeronautics, and Space Science. K. Kirby and J. Babb also graciously allocated us computing time on the CfA Dec Alpha computer. Comments from A. Cameron, F. Franklin, M. Geller, M. Holman, J. Wood and an anonymous referee greatly improved our presentation. We acknowledge G. Stewart for clarifying many details of the WS93 calculations. We also thank S. Stewart for designing and implementing a preliminary version of our computer code as part of her Harvard Senior Thesis. Finally, S.K. thanks S. Starrfield for teaching the tools for solving time-dependent differential equations.

A. APPENDIX

A.1. Overview

Our evolution model follows procedures developed for other planet formation calculations, including Safronov (1969), Greenberg *et al.* (1978, 1984) and WS93. We assume planetesimals are a statistical ensemble of masses with a distribution of horizontal and vertical velocities about a single Keplerian orbit. We consider a cylindrical annulus of width, Δa , and height, H , centered at a radius a from the Sun. Particles in the annulus have a horizontal velocity, $h_i(t)$, and vertical velocity, $v_i(t)$, relative to an orbit with mean Keplerian velocity, V_K (see Lissauer & Stewart 1993). These velocities are related to the eccentricity, e_i , and inclination, i_i , through

$$V_i^2 = \left(\frac{5}{8}e_i^2 + \frac{1}{2}\sin^2 i_i\right)V_K^2, \quad (\text{A1})$$

with

$$h_i^2 = \frac{5}{8}e_i^2V_K^2 \quad (\text{A2})$$

and

$$v_i^2 = \frac{1}{2}\sin^2 i_i V_K^2 \quad (\text{A3})$$

We approximate the continuous distribution of particle masses with discrete batches having an integral number of particles, $n_i(t)$, and total masses, $M_i(t)$ (WS93). The average mass of a batch, $m_i(t) = M_i(t)/n_i(t)$, evolves with time as collisions add and remove bodies from the batch. This procedure naturally conserves mass and allows a coarser grid than simulations with fixed mass bins (Wetherill 1990; see also Ohtsuki & Nakagawa 1988; Kolvoord & Greenberg 1992).

To follow the evolution of particle number, we solve the coagulation equations for all mass bins, k , during a time step, δt ,

$$\delta n_k = \delta t [\epsilon_{ij} A_{ij} n_i n_j - n_k A_{ik} n_i] - \delta n_{k,gd} \quad (\text{A4})$$

$$\delta M_k = \delta t [\epsilon_{ij} A_{ij} n_i n_j m_k - n_k A_{ik} n_i m_k] - m_k \delta n_{k,gd} \quad (\text{A5})$$

where A_{ij} is the cross-section, $\epsilon_{ij} = 1/2$ for $i = j$ and $\epsilon_{ij} = 1$ for $i \neq j$. The three terms in A4–A5 represent (i) mergers of m_i and m_j into a body of mass $m_k = m_i + m_j$, (ii) loss of m_k through mergers with other bodies, and (iii) loss of m_k by gas drag. This treatment assumes (i) that each body can collide with every other body and (ii) that bodies do not fragment during collisions. Assumption (i) is correct for all but the very largest bodies, which become isolated from one another as their orbits circularize due to dynamical friction (see below). We correct equations A4–A5 for this effect by calculating the “gravitational range” of the largest bodies – $R_{g,i} = K_1 a R_{H,ii_{mid}} + 2ae_i$ (WS93) – where $K_1 = 2\sqrt{3}$ and $R_{H,ij} = [(m_i + m_j)/3M_\odot]^{1/3}$ is the mutual Hill radius. As in WS93, the isolated bodies are the N largest bodies that satisfy the summation, $\sum_{i_{min}}^{i_{max}} n_i R_{g,i} \geq \Delta a$. Assumption (ii) is rarely correct, because all collisions produce some debris unless the relative velocity of the two particles is very low (see, for example, WS93). In this paper, we concentrate on planetesimal growth and assume that all collisions result in mergers. We will consider the effects of fragmentation in a separate paper.

To calculate the appropriate index k for a specific collision between batches i and j , we first calculate a fixed grid of masses, m_l , for $l = 1$ to N_{max} and $\delta = m_{l+1}/m_l$. The mass spacing, δ , is constant throughout a calculation; N_{max} increases with time as more batches fill with particles. When a collision produces n_k bodies with m_k , we augment either batch l when $m_k \leq \sqrt{m_l m_{l+1}}$ or batch $l + 1$ when $m_k > \sqrt{m_l m_{l+1}}$. A complete cycle through all mass batches produces new values for n_k and M_k , which yields new values for the average mass per bin, $m_k = M_k/n_k$. This process conserves mass and provides a good description of coagulation when δ is small (see below).

Besides collisions, several processes contribute to the velocity evolution of growing planetesimals, including dynamical friction, gas drag, and viscous stirring. We assume that all collisions between mass batches conserve the horizontal and vertical components of kinetic energy, $E_{h,i} = m_i h_i^2/2$ and $E_{v,i} = m_i v_i^2/2$. The change in the two components of kinetic energy due to collisions is

$$\delta E_{h,k}^{co} = -1/2 \left[\delta n_k (m_k h_k^2) = \delta n_i (m_i h_i^2) + \delta n_j (m_j h_j^2) \right] \quad (\text{A6})$$

$$\delta E_{v,k}^{co} = -1/2 \left[\delta n_k (m_k v_k^2) = \delta n_i (m_i v_i^2) + \delta n_j (m_j v_j^2) \right] \quad (\text{A7})$$

for each pair of collisions between m_i and m_j . In these expressions, $\delta n_i \leq 0$ represents the change in n_i due to collisions with particles in batch j . Batch k loses kinetic energy due to collisions with other batches (e.g., $\delta n_k > 0$). We also calculate the evolution of h_i and v_i due to gas drag (Adachi *et al.* 1976) and collective interactions, such as dynamical friction and viscous stirring, using a statistical treatment of the appropriate Boltzmann and Fokker-Planck equations (Hornung *et al.* 1985; see section A.3 below). The complete change in the horizontal and vertical kinetic energies is thus:

$$\delta E_{h,k} = \delta E_{h,k}^{co} + \delta E_{h,k}^{gd} + \delta E_{h,k}^{in} + \delta E_{h,k}^{lr} \quad (\text{A8})$$

$$\delta E_{h,k} = \delta E_{v,k}^{co} + \delta E_{h,k}^{gd} + \delta E_{h,k}^{in} + \delta E_{h,k}^{lr} \quad (\text{A9})$$

where the superscripts “gd” (gas drag), “in” (inelastic), and “lr” (long range elastic collisions, such as viscous stirring and dynamical friction) refer to a specific type of velocity evolution outlined below (see also Barge & Pellat 1990, 1991; WS93).

We solve the complete set of evolution equations, A4, A5, A8, and A9, using an explicit method that automatically prevents large changes ($> 0.1\%$) in the dynamical variables – n_i , M_i , h_i , and v_i – by limiting the time step. As in WS93, we require integer values for n_i and δn_i . Section A.4 compares our numerical procedures with analytic results from Wetherill (1990; see also Ohtsuki & Nakagawa 1988; Ohtsuki *et al.* 1990). Section 2 of the main text compares calculations at 1 AU with results from WS93. In both cases, our procedures reproduce the expected results. Before describing the analytic results, we first describe in detail our treatment of the collision rates (section A.2) and the velocity evolution (section A.3).

A.2. The Collision Rate

Approximations to the collision rates between planetesimals are in the spirit of kinetic theory, where the number of collisions is the product of the local density, the relative velocity, and a cross-section. WS93 express the number of collisions between a single body, m_i , and all of the bodies, m_j , as

$$n_{c,ij} = \alpha_{coll} \left(\frac{n_j}{4 H a \Delta a} \right) V_{ij} F_{g,ij} (r_i + r_j)^2 \delta t \quad (\text{A10})$$

where r_i and r_j are the radii of the two bodies; $V_{ij}^2 = V_i^2 + V_j^2$ is the relative velocity; and $F_{g,ij}$ is the gravitational focusing factor. The constant factor α_{coll} accounts for the gaussian distribution of particle velocities and the difference between the collision frequency

of particles on Keplerian orbits and those in a box (Greenzweig & Lissauer 1992; WS93). The relative velocities and scale height depend on the individual particle velocities (WS93):

$$H = \frac{\sqrt{2}}{\Omega} (v_i^2 + v_j^2)^{1/2} \quad (\text{A11})$$

$$V_{ij} = (h_i^2 + v_i^2 + h_j^2 + v_j^2)^{1/2} \quad (\text{A12})$$

where Ω is the Keplerian angular frequency. The total number of collisions for m_i is simply $n_i n_c$; the cross-section appropriate for equations A4–A5 is then:

$$A_{ij} = \alpha_{coll} \left(\frac{1}{4 H a \Delta a} \right) V_{ij} F_{g,ij} (r_i + r_j)^2. \quad (\text{A13})$$

We consider two approaches to compute the gravitational focusing factor, $F_{g,ij}$. In the first case, we follow WS93 and set

$$F_{g,ij} = F_{WS,ij} = E_{ij} \left(1 + \beta_{coll} \frac{V_{e,ij}^2}{V_{ij}^2} \right), \quad (\text{A14})$$

where $V_{e,ij}^2 = 2G(m_i + m_j)/(r_i + r_j)$ is the mutual escape velocity. The extra factors account for the gaussian distribution of impact velocities (β_{coll} , Greenzweig & Lissauer 1992) and the deviations from two-body focusing at low relative velocities (E_{ij} , Greenzweig & Lissauer 1990). We adopt WS93’s prescription for the variation of β_{coll} as a function of the relative velocity in Hill units, $V_{H,ij} = V_{ij}/(R_{H,ij} V_K/a)$:

$$\beta_{coll} = \begin{cases} 2.7 & V_{H,ij} > 2 \\ 1.0 + 1.7(V_{H,ij} - 1) & 1 \leq V_{H,ij} \leq 2 \\ 1.0 & V_{H,ij} < 1 \end{cases} \quad (\text{A15})$$

and we set

$$E_{ij} = \begin{cases} 1 & V_{ij} > 0.13V_{e,ij} \\ \frac{4\sqrt{e^2 + \sin^2 i} E_k}{\pi^2 \sin i} & V_{ij} \leq 0.13V_{e,ij} \end{cases} \quad (\text{A16})$$

where $E_k = \int_0^{\pi/2} \sqrt{1 - k^2 \sin^2 \theta} d\theta$ for $k^2 = 3/[4(1 + \sin i/e)]$ (Greenzweig & Lissauer 1990; Greenberg *et al.* 1991).

At very low velocities ($V_{H,ij} < 2.3$), we adopt the two-body collisional cross-sections of Greenberg *et al.* (1991):

$$F_{2B,ij} = \begin{cases} \left(1 + V_{e,ij}^2/V_T^2\right) \left(\frac{V_T}{V_{ij}}\right) \left(\frac{R_H}{R_T}\right) & V_{H,ij} < 2.3 \\ 0.5(1 + V_{e,ij}^2/V_T^2)^{1/2} \left(\frac{V_T}{V_{ij}}\right) \left(\frac{R_H}{R_T}\right) \left(\frac{H}{r_i + r_j}\right) & V_{H,ij} < 2.3, v_{H,ij} < v_{H,crit} \end{cases} \quad (\text{A17})$$

where $R_T = a[(m_i + m_j)/1 \text{ M}_\odot]^{2/5}$ is the Tisserand radius, $V_T = 1.1\Omega\Delta a_T$ is the Tisserand velocity, $\Delta a_T = 2.5R_H$ is the half width of the feeding zone, $v_{H,ij} = v_{ij}/V_H$ is the relative vertical velocity in Hill units, and $v_{H,crit} < 0.7 \sin(0.9[(r_i + r_j)/R_{H,ij}]^{1/2})$.

In our second approach to gravitational focusing, we modify the piecewise analytical approximation of Spaute *et al.* (1991):

$$F_{S,ij} = \begin{cases} 1 + \beta_{coll} \left(\frac{V_{e,ij}}{V_{ij}}\right)^2 & V_{ij} > 0.032V_{e,ij} \\ 42.4042 \left(\frac{V_{e,ij}}{V_{ij}}\right)^{1.2} & 0.01 < V_{ij}/V_{e,ij} \leq 0.032 \\ 10706.916 & V_{ij}/V_{e,ij} \leq 0.01 \end{cases} \quad (\text{A18})$$

with β_{coll} as defined above. These expressions are continuous and serve as a check on the more detailed expressions for $F_{WS,ij}$. For very low velocity encounters, we use the two body cross-sections for F_{2B} defined above.

In these approximations to the cross-section, the transition from F_{WS} or F_S to F_{2B} at $V_{H,ij} \approx 2.3$ is not smooth. To affect a smooth transition, we set

$$F_{g,ij} = \begin{cases} (1 - x_{2B,ij}) F_{WS,ij} + x_{2B,ij} F_{2B,ij} & \\ (1 - x_{2B,ij}) F_{S,ij} + x_{2B,ij} F_{2B,ij} & \end{cases} \quad (\text{A19})$$

where

$$x_{2B,ij} = \begin{cases} 0 & V_{H,ij} > 3.3 \\ 0.5(V_{H,ij} - 2.3) & 1.3 < V_{H,ij} < 3.3 \\ 1 & V_{H,ij} < 1.3 \end{cases} \quad (\text{A20})$$

A.3. Velocity Evolution

As noted above, kinetic models approximate planetesimal orbital elements as a mean square random velocity, V_i^2 (Safronov 1969; Stewart & Wetherill 1988; WS93 and references

therein). We divide this velocity into horizontal, h_i , and vertical, v_i , components that are related to V_i , e , and i (see equations A1–A3). Hornung *et al.* (1985) derive analytic expressions for the time evolution of planetesimal velocities using a kinetic approximation to average over the velocity distribution function. WS93 reformulate some of these results in terms of the eccentricity and inclination, which we adopt here for simplicity (see also Stewart & Wetherill 1988). We calculate velocity changes due to (i) gas drag, which decreases particle velocities and causes particles to spiral in through the disk; (ii) dynamical friction from elastic collisions, which transfers kinetic energy from larger to smaller bodies; (iii) viscous stirring from elastic collisions, which taps the solar gravitational field to increase the velocities of all bodies; and (iv) collisional damping from inelastic collisions (see also Hornung *et al.* 1985; Barge & Pellat 1990, 1991; Ohtsuki 1992).

The time evolution of the eccentricity and inclination for long-range, elastic encounters is (WS93, Appendix C)

$$\frac{de_{vs,i}^2}{dt} = \sum_{j=1}^{j=N} \frac{C_{lr}}{4} (m_i + m_j) e_i^2 (J_r + 4J_\theta) \quad (\text{A21})$$

$$\frac{di_{vs,i}^2}{dt} = \sum_{j=1}^{j=N} \frac{C_{lr}}{2\beta_{ij}^2} (m_i + m_j) i_i^2 J_z \quad (\text{A22})$$

for viscous stirring and

$$\frac{de_{df,i}^2}{dt} = \sum_{j=1}^{j=N} \frac{C_{lr}}{2} (m_j e_j^2 - m_i e_i^2) (K_r + 4K_\theta) \quad (\text{A23})$$

$$\frac{di_{df,i}^2}{dt} = \sum_{j=1}^{j=N} \frac{C_{lr}}{2\beta_{ij}^2} (m_j i_j^2 - m_i i_i^2) K_z \quad (\text{A24})$$

for dynamical friction. In these expressions, e_i , e_j , i_i , and i_j are the eccentricity and inclination of each body, $\beta_{ij}^2 = (i_i^2 + i_j^2)/(e_i^2 + e_j^2)$ is the ratio of inclination to eccentricity, and $C_{lr} = 16G^2\rho_j(\ln\Lambda + 0.55)/V_K^3(e_i^2 + e_j^2)^{3/2}$ is a function of the density of particles in batch j and the relative horizontal velocity of the mass batches (WS93). The functions J_r , J_θ , J_z , K_r , K_θ , and K_z are definite integrals that are functions only of β_{ij} (Hornung *et al.* 1985; Barge & Pellat 1990, 1991; WS93; Ohtsuki 1992) describes a similar approach to velocity evolution).

The time evolution of e and i due to collisional damping is

$$\frac{de_{in,i}^2}{dt} = \sum_{j=0}^{j=i} \frac{C_{in}}{2} (m_j e_j^2 - m_i e_i^2 - (m_i + m_j) e_i^2) (I_r + 4I_\theta) \quad (\text{A25})$$

$$\frac{di_{in,i}^2}{dt} = \sum_{j=0}^{j=i} \frac{C_{in}}{\beta_{ij}^2} (m_j i_j^2 - m_i i_i^2 - (m_i + m_j) i_i^2) I_z \quad (\text{A26})$$

where $C_{in} = \alpha_{coll} \epsilon_{ij} \rho_j V_{ij} F_{g,ij} (r_i + r_j)^2$ and ρ_j is the mass density (Hornung *et al.* 1985; see also Ohtsuki 1992). We include terms from the collision rate, α_{coll} , ϵ_{ij} , and $F_{g,ij}$, for consistency. The integrals, $I_r(\beta_{ij})$, $I_\theta(\beta_{ij})$, and $I_z(\beta_{ij})$, are listed in the Appendices of Hornung *et al.* (1985). We integrate these expressions numerically. The I_z integral often diverges; we set $I_z = I - (I_r + I_\theta)$ to avoid these divergences.

In addition to dynamical friction and viscous stirring, we also consider velocity evolution due to gas drag. Gas drag reduces the velocities of all mass batches and also removes material from each mass batch. The inward drift of material is (Adachi *et al.* 1976):

$$\frac{\Delta a}{a} = 2(0.97e + 0.64i + \eta/V_K) \left(\frac{\eta}{V_K} \right) \frac{\delta t}{\tau_0}, \quad (\text{A27})$$

where η is the gas velocity relative to the local Keplerian velocity, V_K . We adopt $\eta = 60 \text{ m s}^{-1}$ for calculations at 1 AU (WS93) and $\eta = 30 \text{ m s}^{-1}$ for calculations at 35 AU (Adachi *et al.* 1976). The characteristic drift time is

$$\tau_0 = \frac{365}{C_D} \left(\frac{m_i}{10^{21} \text{ g}} \right)^{1/3} \left(\frac{1 \text{ AU}}{a} \right) \left(\frac{10^{-9} \text{ g cm}^{-3}}{\rho_g} \right) T_K, \quad (\text{A28})$$

where $C_D = 0.5$ is the drag coefficient, $\rho_g = 1.18 \times 10^{-9} (a/1 \text{ AU})^{-11/4}$ is the gas density (Nakagawa *et al.* 1983), and T_K is the orbital period (see Adachi *et al.* 1976, WS93). To simulate the disappearance of gas in the protosolar nebula, we decrease the gas density with time:

$$\rho_g(t) = \rho_{g,0} e^{-t/\tau_g} \quad (\text{A29})$$

with $\rho_{g,0} = 1.18 \times 10^{-9} \text{ g cm}^{-3} (a/1 \text{ AU})^{-11/4} (M_0/M_{min})$ (Ruden & Lin 1986; Ruden & Pollack 1991; WS93). The radial decrease of the gas density follows models for minimum mass solar nebulae; the mass dependence allows the density to scale with the mass of the annulus.

The number of bodies lost from the calculation at each time step depends on their effectiveness at crossing Δa . We set the number of bodies lost from a batch as:

$$\frac{\delta n_{gd,i}}{n_i} = \left(\frac{\Delta a}{a} \right) \left(\frac{\delta t}{\tau_0} \right). \quad (\text{A30})$$

This expression is used in equations A4–A5.

Finally, we adopt Wetherill & Stewart's (1989) expression for velocity damping due to gas drag:

$$\frac{dV_i}{dt} = \frac{-\pi C_D}{2m_i} \rho_g V_g^2 r_i^2, \quad (\text{A31})$$

where $C_D = 0.5$ is the drag coefficient and $V_g = (V_i(V_i + \eta))^{1/2}$ is the mean relative velocity of the gas.

We convert the differential equations, A21–A26 and A31, into a kinetic energy form in two steps. We use β_i to derive the appropriate horizontal and vertical components of the velocity, V_i , in Eqn A31. Equations A2–A3 similarly yield δh_i and δv_i in terms of δe_i and δi_i , where

$$\delta e_i^2 = \delta t \left[\frac{de^2}{dt} \right] \quad (\text{A32})$$

and

$$\delta i_i^2 = \delta t \left[\frac{di^2}{dt} \right]. \quad (\text{A33})$$

These substitutions yield:

$$(\delta h_i^{gd})^2 = -\delta t \left[\frac{\pi C_D \rho_g V_g^2 r_i^2}{2m_i(1 + 0.8\beta_i^2)} \right] \quad (\text{A34})$$

$$(\delta v_i^{gd})^2 = 0.8 \beta_i^2 \delta h_i^2 \quad (\text{A35})$$

$$(\delta h_i^{in})^2 = \frac{5}{8} V_K^2 \delta t \left[\frac{de_{in,i}^2}{dt} \right] \quad (\text{A36})$$

$$(\delta v_i^{in})^2 = \frac{1}{2} \sin^2 i V_K^2 \delta t \left[\frac{di_{in,i}^2}{dt} \right] \quad (\text{A37})$$

$$(\delta h_i^{lr})^2 = \frac{5}{8} V_K^2 \delta t \left[\frac{de_{vs,i}^2}{dt} + \frac{de_{df,i}^2}{dt} \right] \quad (\text{A38})$$

$$(\delta v_i^{lr})^2 = \frac{1}{2} \sin^2 i V_K^2 \delta t \left[\frac{di_{vs,i}^2}{dt} + \frac{di_{df,i}^2}{dt} \right] \quad (\text{A39})$$

We multiply these relations by m_i for substitution into equations A8–A9.

A.4. Tests of the evolution code

To test the validity of our numerical techniques, we compare our results with several test cases (see Ohtsuki & Nakagawa 1988; Ohtsuki *et al.* 1990; Wetherill 1990). The coagulation equations, A4–A5, have analytic solutions for three simple forms of the cross-section, A_{ij} . Smoluchowski (1916) first solved the coagulation equation for $A_{ij} = \alpha_c = \text{constant}$. Trubnikov (1971) described solutions for $A_{ij} = \beta_c(m_i + m_j)$ and $A_{ij} = \gamma_c m_i m_j$. Wetherill (1990) identified an inconsistency in Trubnikov’s results for $A_{ij} = \gamma_c m_i m_j$ and showed that this cross-section produces runaway growth. Tanaka & Nakazawa (1994) verified Wetherill’s new solution and placed limits on the validity of the coagulation equation during runaway growth.

The analytic solutions to the coagulation equation provide rigorous tests of numerical methods. Two simple cases, $A_{ij} = \alpha_c$ and $A_{ij} = \beta_c(m_i + m_j)$, do not lead to runaway growth, but they test the ability of numerical codes to reach a target mass at a specified time. They also yield estimates for mass conservation over many time steps. Numerical solutions for $A_{ij} = \gamma_c m_i m_j$ are challenging, because runaway growth requires a careful, automatic procedure for changing the time step. In all three cases, the time lag between the analytic and numerical solutions depends on the mass ratio between consecutive batches, δ (Wetherill 1990). These tests thus yield a quantitative measure of the largest allowed value for δ (Ohtsuki & Nakagawa 1988; Ohtsuki *et al.* 1990; Wetherill 1990).

To compare our numerical results with analytic solutions, we follow conventions established by Ohtsuki *et al.* (1988) and Wetherill (1990). For $A_{ij} = \alpha_c$ and $A_{ij} = \beta_c(m_i + m_j)$, we plot $\log N_i m_i^2$ as a function of $\log m_i$. We evaluate $\log N_k$ as a function of $\log m_k$ and the fractional mass in the small body swarm and the runaway body as a function of a dimensionless time for $A_{ij} = \gamma_c m_i m_j$. The numerical calculations do not have regular mass intervals, so we calculate $N = \delta N / \delta m$, where

$$\delta N = N_k + (N_{k+1} + N_{k-1})/2 \quad (\text{A40})$$

$$\delta m = m_{k+1} - m_{k-1}. \quad (\text{A41})$$

Wetherill (1990) describes analytic solutions for each cross-section in detail. The $A_{ij} = \alpha_c$ case has the simplest solution. If n_0 is the initial number of particles with mass m_i , the number of bodies with mass $m_k = km_i$ at a time, t , is

$$n_k = n_0 f^2 (1 - f)^{k-1} \quad (\text{A42})$$

where $f = 1/(1 + \eta_1/2)$ and $\eta_1 = \alpha_c n_0 t$ is the dimensionless time (see also Silk & Takahashi 1979; Ohtsuki & Nakagawa 1988). The solution for $A_{ij} = \beta_c(m_i + m_j)$ has a similar form:

$$n_k = n_0 \frac{k^{k-1}}{k!} f (1-f)^{k-1} e^{-k(1-f)} \quad (\text{A43})$$

where $f = e^{-\eta_2}$ and $\eta_2 = \beta_c n_0 t$. In both of these expressions, f is the fraction of bodies with m_i that have yet to undergo a collision at time t .

Models with $A_{ij} = \gamma_c m_i m_j$ lead to runaway growth when $\eta_3 = \gamma n_0 t = 1$ (Wetherill 1990; Barge & Pellat 1990; Tanaka & Nakazawa 1994). The number distribution for $\eta_3 \leq 1$ is

$$n_k = n_0 \frac{(2k)^{k-1}}{k! k} (\eta_3/2)^{k-1} e^{-k\eta_3} \quad (\text{A44})$$

This solution fails to conserve mass for $\eta_3 > 1$; a single runaway body then contains most of the total mass. The mass of the runaway body for $\eta_3 > 1$ is (Wetherill 1990; Tanaka & Nakazawa 1993, 1994):

$$m_R = n_0 e^{-\int \sum_{k=1}^N k^2 (n_k/n_0) d\eta'} \quad (\text{A45})$$

Figure 15 compares our results for $\delta = 1.25$ with the analytic solution for $A_{ij} = \alpha_c$. The agreement is good and again improves as δ decreases. Our results for $\delta = 1.4$ – 1.6 are consistent with the analytic solution, although we have too few mass batches to make reliable comparisons when $\eta_1 < 10$ – 20 . We did not attempt numerical models for $\delta = 1.6$ – 2 (the maximum allowed), but we expect that these will produce satisfactory results for $\eta > 100$.

Figure 16 shows results for $A_{ij} = \beta_c (m_i + m_j)$ and $\delta = 1.25$. The agreement between our calculation and the analytic solution is quite good and improves as δ increases. We find a slight excess of low mass bodies in our numerical results compared to the analytic solution. Wetherill’s Figure 4 contains a similar excess. The peak of our normalized number distribution lags the analytic result by 1.4%. This lag decreases with δ and is < 1% for $\delta = 1.10$.

Figures 17 and 18 summarize our results for $A_{ij} = \gamma_c m_i m_j$ and $\delta = 1.25$ for $\eta \leq 1$. The numerical solution follows the analytic model very closely for $\eta_3 < 0.95$ and then begins to diverge at large masses as η approaches unity (Figure 17). The numerical model begins runaway growth at $\eta_3 = 1.012$ and lags the analytic model by 1.2%. The numerical runaway begins much closer to the predicted result, $\eta_3 = 1.005$, for $\delta = 1.08$. Larger values for δ produce runaways that are delayed by much longer factors. The lag is 2.7% for $\delta = 1.4$ and 8.7% for $\delta = 2$. Wetherill (1990) quotes similar results for his numerical models with $\delta = 1.07$ and $\delta = 1.25$.

Figure 18 describes the evolution of the runaway growth model for $\delta = 1.08$ and $\eta_3 > 1$. The calculated mass distribution initially lags the analytic result by less than 1% for η_3

marginally larger than 1 (see also WS93) but matches the analytic result almost exactly at $\eta_3 = 1.05$ (Figure 18; left panel). The calculation continues to match the analytic result until $\eta_3 \approx 5$. The right panel of Figure 18 plots the mass of the runaway body for $\eta_3 \geq 1$. The calculated mass agrees with the analytic prediction, Eqn. A45, to 1% or better for all $\eta_3 \geq 1$. Models with $\delta = 1.25$ have greater difficulty reaching large η_3 due to their poorer mass resolution. These models have larger n_k at high masses, which reduces the time step considerably compared to models with small δ . The calculation then requires a significant amount of computer time and does not agree as well with the analytic predictions. Our models with $\delta \geq 1.4$ fail to reach $\eta_3 \approx 1.1$ if we maintain our criterion of small δn_k per time step. Relaxing this criterion allows reasonable time steps but produces very poor agreement, $\gtrsim 20\%$, with the analytic solution.

These results confirm our limits on δn_k for the Kuiper Belt simulation described in the main text, $\lesssim 0.1\%$ per time step, for $\delta = 1.08\text{--}1.4$. Models with larger δ fail to follow growth properly unless the time steps are unreasonably small.

TABLE 1. Basic Model Parameters

Parameter	Symbol	1 AU Models	35 AU Models
Width of annulus	δa	0.17 AU	6 AU
Initial Velocity	V_0	4.7 m s ⁻¹	4.5–45 m s ⁻¹
Particle mass density	ρ_0	3 g cm ⁻³	1.5 g cm ⁻³
Relative gas velocity	η	60 m s ⁻¹	30 m s ⁻¹
Time Step	δt	0.5 yr	5–250 yr
Number of mass bins	N	100–150	64–128
Mass Spacing of bins	δ	≤ 1.20	1.40

TABLE 2. Model Results at 1 AU^(a)

Time (yr)	$\delta = 1.25$			$\delta = 1.40$		
	r_{max} (km)	$m(r_{max})$ (kg)	$N(r_{max})$	r_{max} (km)	$m(r_{max})$ (kg)	$N(r_{max})$
5.0×10^2	19.8	9.7×10^{19}	3	20.9	1.2×10^{20}	1
1.0×10^4	513.3	1.7×10^{24}	3	492.3	1.5×10^{24}	1
2.5×10^4	1167.3	2.0×10^{25}	1	1203.0	2.2×10^{25}	1
5.0×10^4	1540.8	4.6×10^{25}	3	1515.7	4.4×10^{25}	1
1.0×10^5	1890.8	8.5×10^{25}	2	1746.7	6.7×10^{25}	3
1.5×10^5	1948.3	9.3×10^{25}	5	2382.7	1.7×10^{26}	1

^(a)These results are for the WS93 prescription of gravitational focusing, equations A14–A16, as summarized in the main text.

TABLE 3. Model Results at 1 AU^(a)

Time (yr)	$\delta = 1.25$			$\delta = 1.40$		
	r_{max} (km)	$m(r_{max})$ (kg)	$N(r_{max})$	r_{max} (km)	$m(r_{max})$ (kg)	$N(r_{max})$
5.0×10^2	19.8	9.7×10^{19}	3	20.9	1.2×10^{20}	1
1.0×10^4	550.8	2.1×10^{24}	2	492.3	1.5×10^{24}	1
2.5×10^4	1167.5	2.0×10^{25}	1	1223.0	2.3×10^{25}	1
5.0×10^4	1458.6	3.9×10^{25}	4	1735.0	6.6×10^{25}	2
1.0×10^5	1969.0	9.6×10^{25}	1	2174.8	1.3×10^{26}	1
1.5×10^5	2121.0	1.2×10^{26}	1	2335.0	1.7×10^{26}	1

^(a)These results are for an adaptation of the Spaute et al. (1991) prescription of gravitational focusing, equation A18, as summarized in the main text.

TABLE 4. Model Results at 100 Myr (No Fragmentation, No Velocity Evolution)

$M_0 (M_e)$	e	r_0 (m)	N_0	$r_{95\%}$ (km)	r_5 (km)	r_{max} (km)	$N(r_{max})$	τ_r (MYr)
1	10^{-3}	80	1.87×10^{15}	0.5	0.6	0.9	1	2698
3	5.61×10^{15}	1.1	1.5	2.2	1	902
10	1.87×10^{16}	3.9	5.4	6.7	1925	270
30	5.61×10^{16}	NA	NA	8500	1	90
100	1.87×10^{17}	NA	NA	18500	1	27
1	...	800	1.87×10^{12}	1.4	2.2	2.7	1	2340
3	5.61×10^{12}	2.2	3.0	4.2	4	780
10	1.87×10^{13}	5.5	8.5	10.7	341	234
30	5.61×10^{13}	NA	NA	18000	2	78
100	1.87×10^{14}	NA	NA	16700	1	23.5
1	...	8000	1.87×10^9	13.3	16.9	20.7	140	753
3	5.61×10^9	19.2	26.8	36.7	91	250
10	1.87×10^{10}	NA	NA	7585	5	75
30	5.61×10^{10}	NA	NA	9800	1	25
100	1.87×10^{11}	NA	NA	8700	2	7.5
1	10^{-2}	80	1.87×10^{15}	0.5	0.6	0.9	1	...
3	5.61×10^{15}	1.1	1.5	1.9	634	...
10	1.87×10^{16}	3.1	4.8	6.0	28	2552
30	5.61×10^{16}	9.6	13.2	16.4	323	850
100	1.87×10^{17}	33.6	46.5	63.5	5	255
1	...	800	1.87×10^{12}	1.4	2.2	2.4	3195	...
3	5.61×10^{12}	2.2	3.1	3.8	75	...
10	1.87×10^{13}	4.4	6.8	7.4	2018	2521
30	5.61×10^{13}	10.8	14.8	18.4	387	840
100	1.87×10^{14}	37.6	51.8	65.0	70	251
1	...	8000	1.87×10^9	10.1	11.6	16.1	1	...
3	5.61×10^9	11.7	14.9	18.5	8	...
10	1.87×10^{10}	13.4	18.5	23.3	298	2146
30	5.61×10^{10}	21.2	29.3	39.9	1	716
100	1.87×10^{11}	59.2	81.9	104.2	18	215

TABLE 5. Model Results (Velocity Evolution, No Fragmentation)

M_0 (M_e)	e	r_0 (m)	N_0	$r_{95\%}$ (km)	r_5 (km)	r_{max} (km)	$N(r_{max})$	τ_r (MYr)
1	10^{-3}	80	1.87×10^{15}	0.5	0.8	0.9	6	...
2	3.74×10^{15}	2.6	30.4	126.1	2	...
3	5.61×10^{15}	2.7	33.8	603.4	1	184
6	1.12×10^{16}	2.9	44.1	1072.6	1	67
10	1.87×10^{16}	2.6	54.1	1000.5	1	32
17	3.18×10^{16}	2.4	55.7	1008.5	1	18
30	5.61×10^{16}	2.7	74.4	1059.2	1	10
1	...	800	1.87×10^{12}	1.4	2.3	2.7	9	...
2	3.74×10^{12}	2.0	3.2	3.7	24	...
3	5.61×10^{12}	2.8	5.4	6.8	1	...
6	1.12×10^{13}	11.2	47.3	456.9	1	155
10	1.87×10^{13}	10.6	51.4	1007.8	1	83
17	3.18×10^{13}	10.6	68.2	1022.7	1	46
30	5.61×10^{13}	10.6	90.7	1000.3	2	25
1	...	8000	1.87×10^9	11.7	17.9	23.9	8	...
2	3.74×10^9	15.3	24.1	32.7	7	...
3	5.61×10^9	17.3	30.6	46.0	4	...
6	1.12×10^{10}	27.3	57.1	123.0	1	...
10	1.87×10^{10}	43.4	90.6	462.4	1	132
17	3.18×10^{10}	48.8	101.2	1050.0	1	76
30	5.61×10^{10}	51.7	114.2	1017.7	2	44
1	10^{-2}	80	1.87×10^{15}	0.4	0.6	0.8	762	...
2	3.74×10^{15}	0.7	1.2	1.4	39	...
3	5.61×10^{15}	1.0	1.8	1.9	1103	...
6	1.12×10^{16}	5.8	46.6	294.7	1	126
10	1.87×10^{16}	6.3	60.4	1004.1	1	76
17	3.18×10^{16}	6.4	70.0	1002.2	2	43
30	5.61×10^{16}	6.4	82.2	1070.2	1	24
1	...	800	1.87×10^{12}	1.4	2.2	2.7	2	...
2	3.74×10^{12}	1.8	2.8	3.4	2	...
3	5.61×10^{12}	2.2	3.3	3.8	48	...
6	1.12×10^{13}	3.1	4.9	6.0	1	...
10	1.87×10^{13}	4.4	7.3	8.4	78	...
17	3.18×10^{13}	13.9	43.0	74.1	4	130
30	5.61×10^{13}	23.4	90.8	1000.5	2	73
1	...	8000	1.87×10^9	10.1	13.0	16.3	6	...
2	3.74×10^9	10.1	14.3	16.4	303	...
3	5.61×10^9	11.7	15.3	18.3	11	...
6	1.12×10^{10}	13.2	17.8	20.7	68	...
10	1.87×10^{10}	13.4	20.8	26.1	2	...
17	3.18×10^{10}	17.0	25.9	31.0	46	...
30	5.61×10^{10}	28.3	45.8	62.3	6	167

REFERENCES

Aarseth, S. J., Lin, D. N. C., & Palmer, P. L. 1993, *ApJ*, 403, 351

Adachi, I., Hayashi, C., Nakazawa, K. 1976, *Progress of Theoretical Physics* 56, 1756 - 1771.

Bailey, M. 1994, In *Asteroids, Comets, Meteors 1993*, eds. A. Milani, M. DiMartino, and A. Cellino (Kluwer Academic Publishers, Dordrecht), pp. 443 - 459.

Backman, D. E., & Paresce, F. 1993, in *Protostars and Planets III*, eds. E. H. Levy & J. I. Lunine, Tucson, Univ of Arizona, p. 1253

Barge, P., & Pellat, R. 1990, *Icarus*, 85, 481

Barge, P., & Pellat, R. 1991, *Icarus*, 93, 270

Barge, P., & Pellat, R. 1993, *Icarus*, 104, 79

Beckwith, S. V. W., & Sargent, A. I. 1996, *Nature*, 383, 139

Boss, A. P. 1993, *ApJ*, 417, 351

Davis, D. R., & Farinella, P. 1997, *Icarus*, 125, 50

Duncan, M. J., Levison, H. F., & Budd, S. M. 1995, *AJ*, 110, 3073

Edgeworth, K. E. 1949, *MNRAS*, 109, 600

Fernández, J. A. 1997, *Icarus*, 129, 106

Fernández, J. A., & Ip, W.-H. 1981, *Icarus*, 47, 470

Fernández, J. A., & Ip, W.-H. 1984, *Icarus*, 58, 109

Fernández, J. A., & Ip, W.-H. 1996, *Astrophys Sp Sci*, 44, 431

Goldreich, P., & Ward, W. R. 1973, *ApJ*, 183, 1051

Greenberg, R., Wacker, J. F., Hartmann, W. K., & Chapman, C. R. 1978, *Icarus*, 35, 1

Greenberg, R., Bottke, W., Carusi, A., Valsecchi, G. B. 1991, *Icarus*, 94, 98

Greenzweig, Y., & Lissauer, J. J. 1990, *Icarus*, 87, 40

Greenzweig, Y., & Lissauer, J. J. 1992, *Icarus*, 100, 440

Hayashi, C. 1981, *Prog Theor Phys Suppl*, 70, 35

Hayashi, C., Nakazawa, K., & Nakagawa, Y. 1985, In *Protostars and Planets II*, eds. 4 (U. of Arizona Press, Tucson, pp. 1100 - 1153.

Holman, M. J., & Wisdom, J. 1993, AJ, 105, 1987

Hornung, P., Pellat, R., & Barge, P. 1985, Icarus, 64, 295

Housen, K. R., Schmidt, R. M., & Holsapple, K. A. 1991, Icarus, 94, 180

Ida, S. 1990, Icarus, 88, 129

Ida, S., & Makino, J. 1992, Icarus, 96, 107

Ida, S., & Makino, J. 1992, Icarus, 98, 28

Ip, W.-H. 1989, Icarus, 80, 167

Ipatov, S. I. 1989, Solar System Res, 23, 119

Ipatov, S. I. 1991, Soviet Astron Lett, 17, 113

Jewitt, D., Luu, J., & Chen, J. 1996, AJ, 112, 1225

Jewitt, D., & Luu, J. 1995, AJ, 109, 1867

Kenyon, S. J., & Hartmann, L. W. 1995, ApJS, 101, 177

Kokubo, E., & Ida, S. 1996, Icarus, 123, 180

Kolvoord, R. A. & Greenberg, R. 1992, Icarus, 98, 2

Kuiper, G. P. 1951. "On the Origin of the Solar System." In *Astrophysics: A Topical Symposium*, ed. J. A. Hynek (McGraw-Hill, New York, 357 - 424.

Levison, H. F., & Duncan, M. J. 1993, ApJ, 406, L35

Lissauer, J. J., Stewart, G. R. 1993, Growth of Planets from Planetesimals. In *Protostars and Planets III*, eds. E. H. Levy and J. I. Lunine (U. of Arizona Press, Tucson, 1061 - 1088.

Lissauer, J. J., Pollack, J. B., Wetherill, G. W., & Stevenson, D. J. 1996. "Formation of the Neptune System." In *Neptune and Triton*, eds. D. P. Cruikshank, M. S. Matthews, and A. M. Schumann (U. of Arizona Press, Tucson, pp. 37 - 108.

Luu, J. X., Marsden, B., Jewitt, D., Trujillo, C. A., Hergenother, C. W., Chen, J., & Offutt, W. B. 1997, Nature, in press

Malhotra, R. 1993, *Nature*, 365, 819

Malhotra, R. 1995, *AJ*, 110, 420

Malhotra, R. 1996, *AJ*, 111, 504

Morbidelli, A., Thomas, F., & Moons, M. 1995, *Icarus*, 118, 322

Nakagawa, Y., Hayashi, C., & Nakazawa, K. 1983, *Icarus*, 54, 361

Ohtsuki, K., & Nakagawa, Y. 1988, *Prog Theor Phys (Suppl)*, 96, 239

Ohtsuki, K., Nakagawa, Y., & Nakazawa, K. 1990, *Icarus*, 83, 205

Ohtsuki, K. 1992, *Icarus*, 98, 20

Pollack, J. B., Hubickyj, O., Bodenheimer, P., Lissauer, J. J., Podolak, M., & Greenzweig, Y. 1996, *Icarus*, 124, 62

Ruden, S. P., & Lin, D. N. C. 1986, *ApJ*, 308, 883

Ruden, S. P., & Pollack, J. B. 1991, *ApJ*, 375, 740

Russell, S. S., Srinivasan, G., Huss, G. R., Wasserburg, G. J., & Macpherson, G. J. 1996, *Science*, 273, 757

Safronov, V. S. 1969, *Evolution of the Protoplanetary Cloud and Formation of the Earth and Planets*, Nauka, Moscow [Translation 1972, NASA TT F-677]

Sargent, A. I., & Beckwith, S. V. W. 1993, *Phy Tod*, 46, 22

Silk, J., & Takahashi, T. 1979, *ApJ*, 229, 242

Spaute, D., Weidenschilling, S. J., Davis, D. R., & Marzari, F. 1991, *Icarus*, 92, 147

Stern, S. A. 1995, *AJ*, 110, 856

Stern, S. A. 1996, *AJ*, 112, 1203

Stern, S. A., & Colwell, J. E. 1997a, *AJ*, 114, 841

Stern, S. A., & Colwell, J. E. 1997b, *ApJ*, 490, 879

Stewart, G. R., & Wetherill, G. W. 1988, *Icarus*, 75, 542

Strom, S. E., Edwards, S., & Skrutskie, M. F. 1993, in *Protostars and Planets III*, eds. E. H. Levy & J. I. Lunine, Tucson, Univ of Arizona, p. 837

Tanaka, H., & Nakazawa, K. 1993, J Geomag Geoelec, 45, 361.

Tanaka, H., & Nakazawa, K. 1994, Icarus, 107, 404.

Trubnikov, B. A. 1971, Doklady Acad. Nauk SSSR, 196, 1316

Weidenschilling, S. J. 1977, Astrophys Sp Sci, 51, 153

Weidenschilling, S. J. 1980, Icarus, 44, 172

Weidenschilling, S. J., & Cuzzi, J. N., 1993, in *Protostars and Planets III*, edited by E. H. Levy & J. I. Lunine, Tucson, Univ of Arizona, p. 1031

Weidenschilling, S. J., & Davis, D. R. 1992, Lun Planet Sci, XXIII, 1507

Wetherill, G. W. 1990, Icarus, 88, 336

Wetherill, G. W., & Stewart, G. R. 1989. Icarus 77, 300 - 357.

Wetherill, G. W., & Stewart, G. R. 1993, Icarus, 106, 190 (WS93)

FIGURE CAPTIONS

Fig. 1.— Results at 1 AU for $M_0 = 0.667 M_{\oplus}$ and $\delta = 1.25$. (a) Cumulative mass distribution at selected times. The “runaway plateau” forms at $\sim 2 \times 10^4$ yr; it includes 17% of the total mass at 5×10^4 yr, 18% of the total mass at 10^5 yr, and 22% at 1.5×10^5 yr. (b) Horizontal velocity distribution. Viscous stirring increases all velocities with time; dynamical friction breaks the runaway bodies and increases velocities of the lowest mass bodies.

Fig. 2.— Results at 1 AU for $\delta = 1.4$. The runaway plateau is more poorly resolved as the mass spacing increases. (a) Cumulative mass distribution at selected times. The “runaway plateau” includes 12% of the total mass at 5×10^4 yr; this component comprises 18% of the total mass at 10^5 yr and 22% at 1.5×10^5 yr. (b) Horizontal velocity distribution. The horizontal velocities of low mass objects are 5% larger with $\delta = 1.4$ than with $\delta = 1.25$. Higher mass bodies have velocities 2–3 larger than comparable masses in $\delta = 1.25$ simulations.

Fig. 3.— Cumulative size distribution for $M_0 = 10 M_{\oplus}$, $r_0 = 8$ km, and $e = 10^{-3}$. The eccentricity of this model is constant in time. Collisional growth is quasi-linear for 50 Myr until the largest bodies have $r_{max} = 50$ km. Runaway growth begins when $r_{max} \gtrsim 100$ km; these bodies then grow to sizes of 10^3 km to 10^4 km in 20–30 Myr.

Fig. 4.— Radius evolution as a function of initial mass for constant velocity models, with (a) $r_0 = 8$ km, (b) $r_0 = 800$ m, and (c) $r_0 = 80$ m. The eccentricity is $e = 10^{-3}$. The time to runaway growth scales inversely with initial mass, $\tau_r \approx \tau_0 (M_0/1M_{\oplus})^{-1}$; $\tau_0 \approx 753$ Myr for $r_0 = 8$ km, $\tau_0 \approx 2340$ Myr for $r_0 = 800$ m, and $\tau_0 \approx 2700$ Myr for $r_0 = 80$ m.

Fig. 5.— Same as Fig. 4, but with eccentricity $e = 10^{-2}$. (a) $r_0 = 8$ km, (b) $r_0 = 800$ m, and (c) $r_0 = 80$ m.

Fig. 6.— Cumulative size distribution for a constant velocity model with $\delta = 1.1$ for $M_0 = 10 M_{\oplus}$, $r_0 = 8$ km, and $e = 10^{-3}$. This model produces a cumulative size distribution with two distinct power laws: $N_C \propto r^{-2.7}$ for $8 \text{ km} \lesssim r_i \lesssim 300 \text{ km}$ and $N_C \propto r^{-1.7}$ for $300 \text{ km} \lesssim r_i \lesssim 5000 \text{ km}$.

Fig. 7.— Time scales for viscous stirring (solid line) and collisional damping (dashed line) as a function of mass. (a) The two curves show the time scales for interactions only between particles of the same mass for a realistic cumulative mass distribution. The two plots curve up at high masses due to the small number of particles. Collisional damping balances the velocity increase due to viscous stirring at $\sim 10^{15}$ kg. (b) Time scales integrated over all particles during the initial stages, ~ 10 Myr, of a model with velocity evolution. Collisional damping overcomes velocity increases from viscous stirring only for $m_i \lesssim 10^{12}$ kg. (c) As in (b) but for a late stage in the growth process, 15–16 Myr. The integrated effects of viscous stirring now increase the velocities of all particles.

Fig. 8.— Model with $M_0 = 10 M_{\oplus}$, $r_0 = 8$ km, and $e = 10^{-3}$, with velocity evolution: (a) cumulative size distribution, and (b) horizontal velocity as a function of time. Collisional growth is quasi-linear until the largest bodies have $r_{max} = 50\text{--}100$ km at 50–60 Myr. Runaway growth begins when $r_{max} \gtrsim 500$ km at ~ 100 Myr; these bodies then grow to sizes of 10^3 km in another 50–80 Myr.

Fig. 9.— Model with $M_0 = 10 M_{\oplus}$, $r_0 = 800$ m, and $e = 10^{-3}$: (a) cumulative size distribution, and (b) horizontal velocity as a function of time. Collisional growth is quasi-linear for 45–50 Myr until the largest bodies have $r_{max} = 50\text{--}100$ km. The transition to runaway growth requires ~ 10 Myr, when Charon-sized objects form. These bodies grow to sizes of 1000 km in another 20 Myr. The velocities of the smallest objects increase with due to viscous stirring. Dynamical friction reduces the velocities of the largest objects. The velocity minimum at 3–5 km indicates the batches that contain the largest fraction of the

total mass.

Fig. 10.— Model with $M_0 = 10 M_{\oplus}$, $r_0 = 80$ m, and $e = 10^{-3}$: (a) cumulative size distribution, and (b) horizontal velocity as a function of time. The largest bodies reach $r_{max} = 50\text{--}100$ km in 20 Myr and $r_{max} = 500$ km in only 25 Myr. Runaway growth begins at 25 Myr and the largest bodies achieve $r_{max} \sim 1000$ km after another 8 Myr. As in Figure 9, dynamical friction and viscous stirring increase the velocities of the smallest objects at the expense of the largest objects. Dynamical friction produces a velocity minimum in batches that contain the largest fraction of the total mass.

Fig. 11.— Evolution of the maximum radius with time for models with different initial mass (M_0) and initial radius (r_0), for low initial eccentricity ($e = 10^{-3}$). The time scale to reach runaway growth decreases with smaller r_0 and with larger M_0 .

Fig. 12.— Evolution of the maximum radius as in Figure 11, for models with large initial eccentricity ($e = 10^{-2}$). Models with high e require 2–4 times more mass to reach runaway growth on time scales similar to that of low e models.

Fig. 13.— Summary of velocity evolution models for (a) $e = 10^{-3}$ and (b) $e = 10^{-2}$. Filled circles indicate successful simulations that produce a few Pluto-sized objects and $\sim 10^5$ KBOs in 100 Myr or less; open circles indicate simulations that produce no Plutos and too few KBOs in 100 Myr or less); filled circles within a larger open circle indicate partially successful simulations that produce a few Pluto-sized objects but too few KBOs in 100 Myr or less).

Fig. 14.— The evolution of $M_{max}/\langle m \rangle$, as a function of time. (a) constant velocity models, and (b) with velocity evolution. The rapid increase in $M_{max}/\langle m \rangle$ at the latter stages of many simulations indicates runaway growth.

Fig. 15.— Evolution of the mass distribution for a constant cross-section, $A_{ij} = \alpha_c$. The solid lines plot analytic results for four values of η ; the symbols indicate results of the numerical simulations.

Fig. 16.— Evolution of the mass distribution for $A_{ij} = \beta_c(M_i + M_j)$. The solid lines plot analytic results for four values of η ; the symbols indicate results of the numerical simulations.

Fig. 17.— Evolution of the mass distribution for $A_{ij} = \gamma_c M_i M_j$. The solid lines plot analytic results for four values of η ; the symbols indicate results of the numerical simulations.

Fig. 18.— Runaway growth for $A_{ij} = \gamma_c M_i M_j$. (a) Evolution of the residual mass distribution for four values of $\eta > 1$. The simulations lag the analytic model for $\eta \approx 1$ and then follow it closely for larger η . (b) Evolution of the mass of the runaway body for the simulation (symbols) and the analytic model (solid curve) as a function of η .

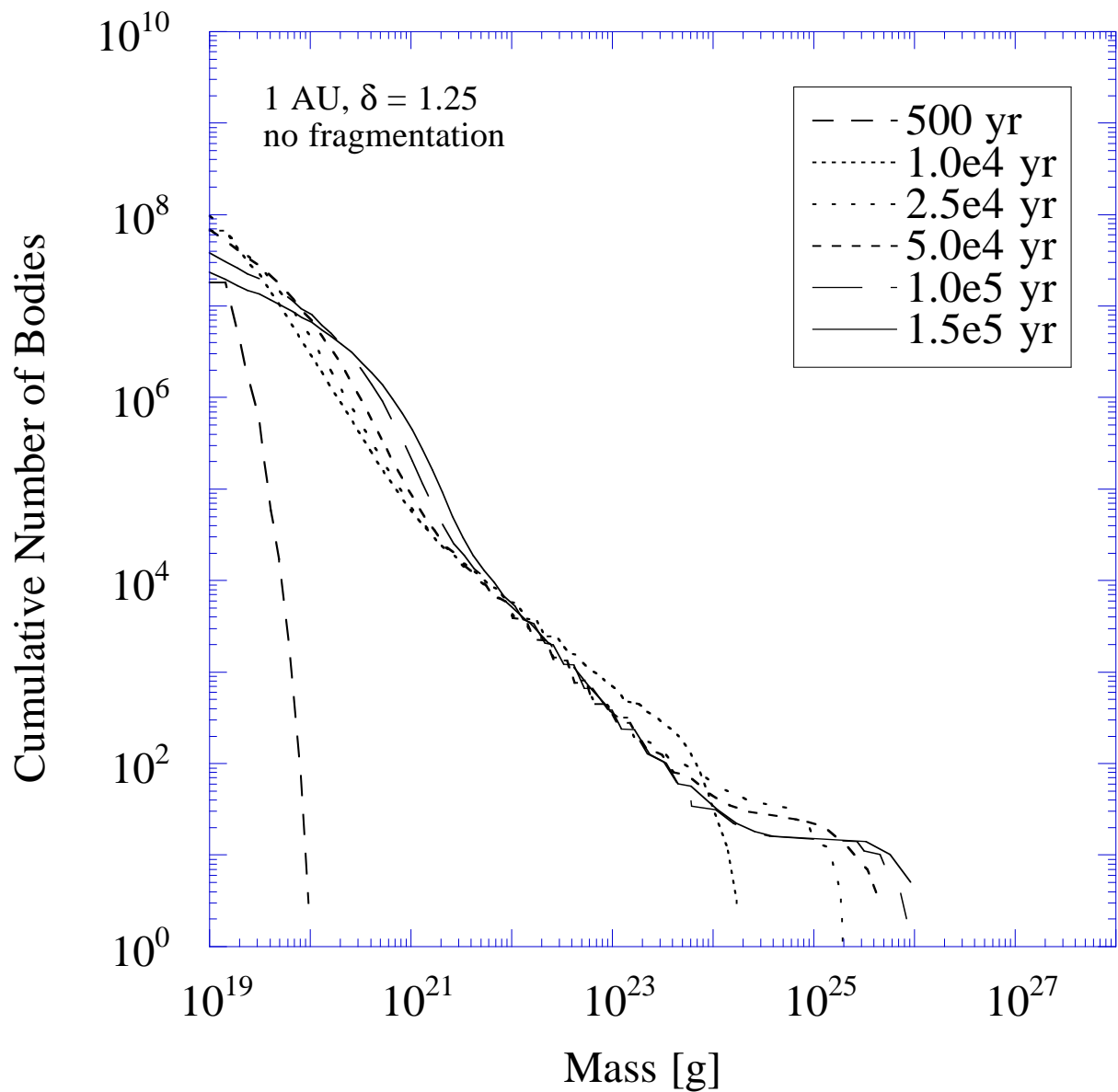


Fig. 1a

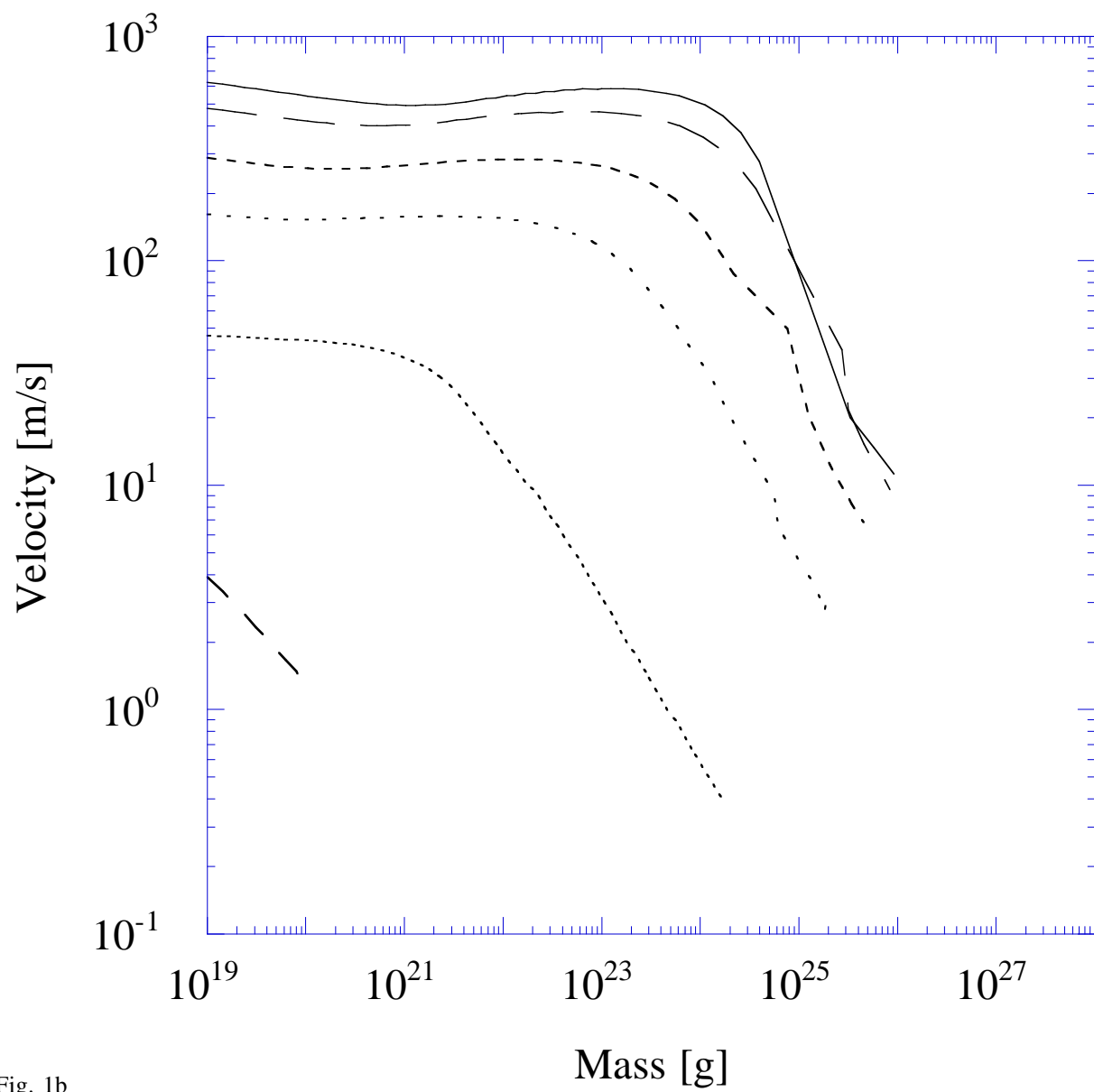


Fig. 1b

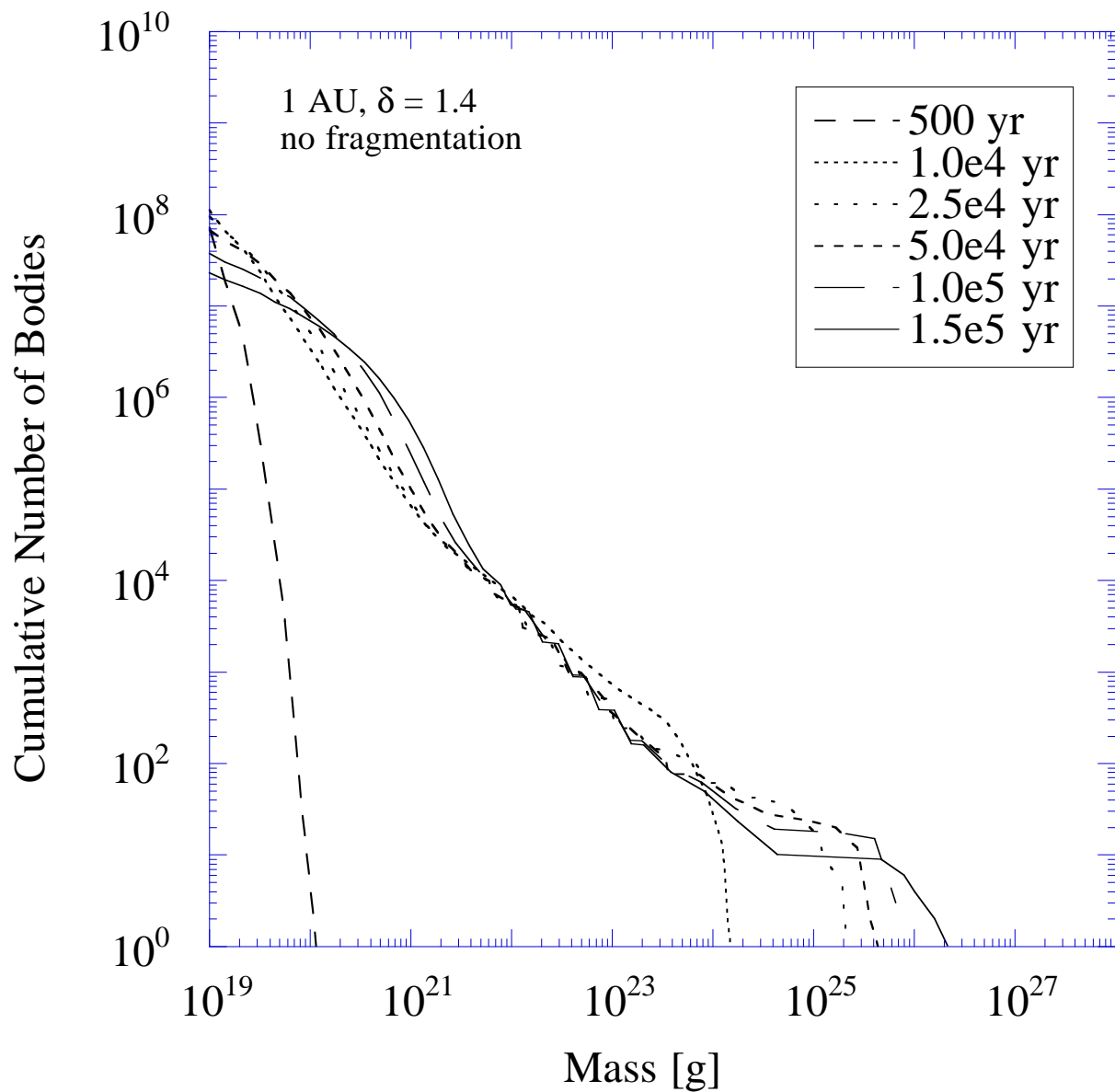


Fig. 2a

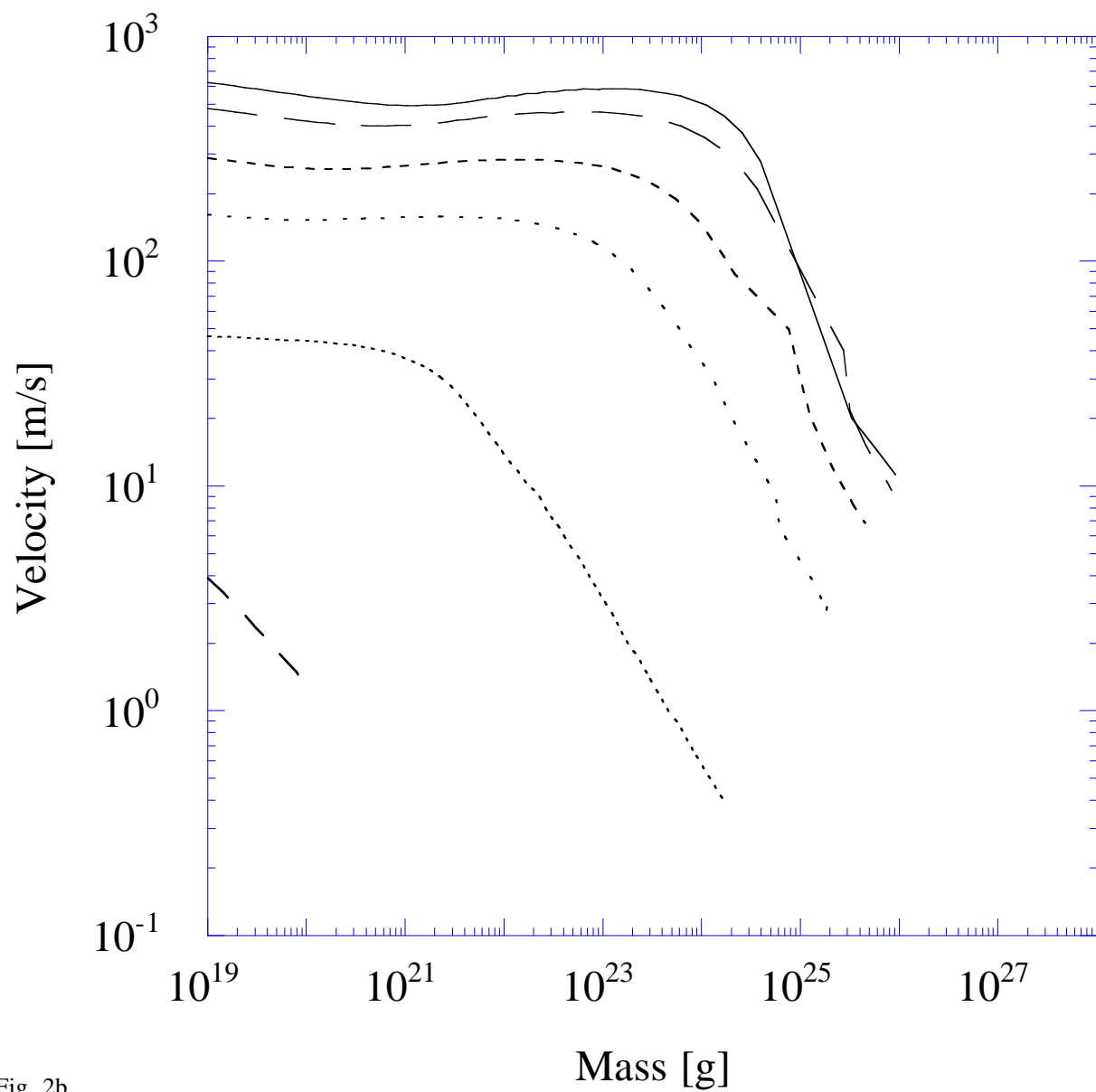


Fig. 2b

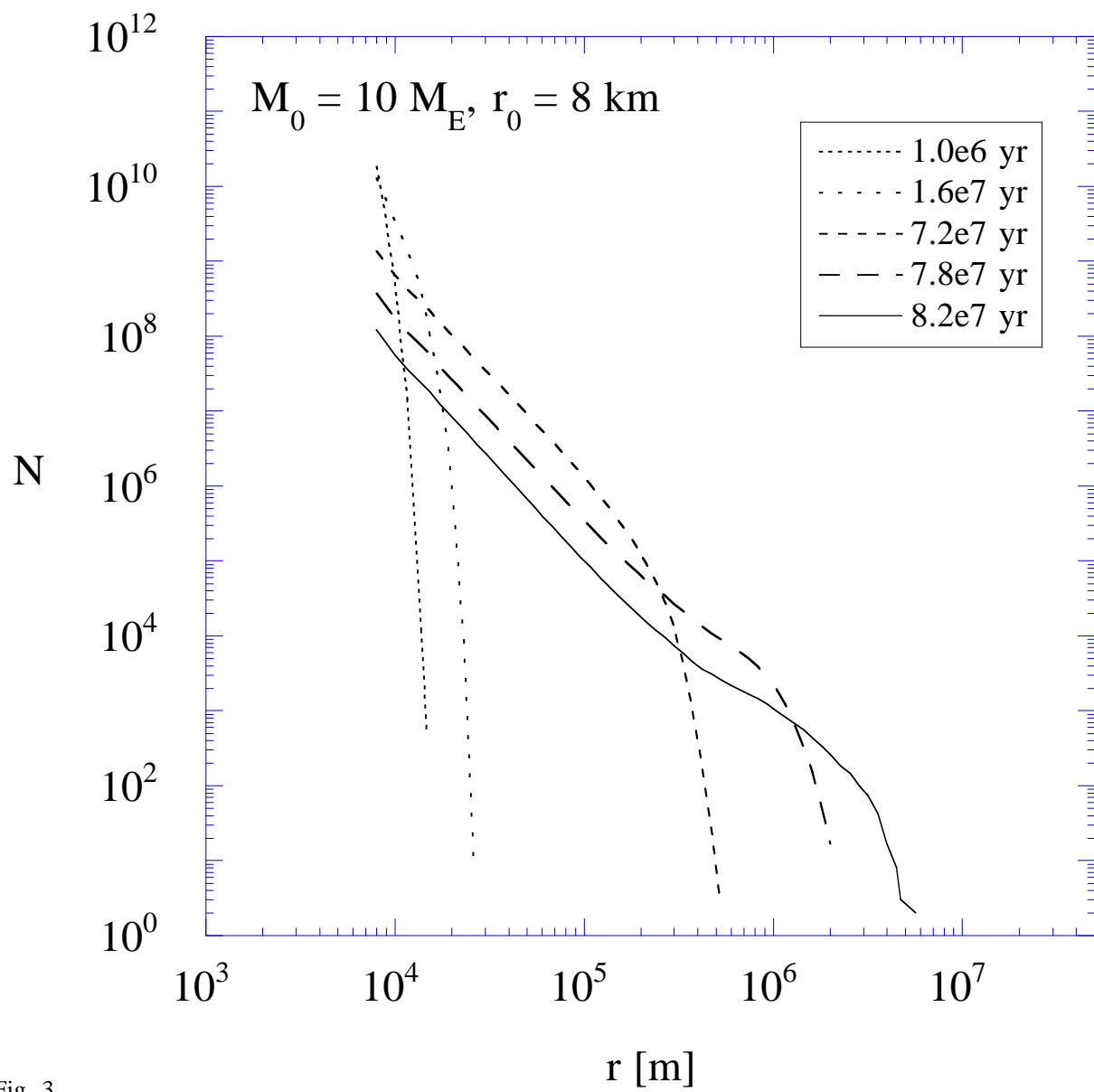


Fig. 3

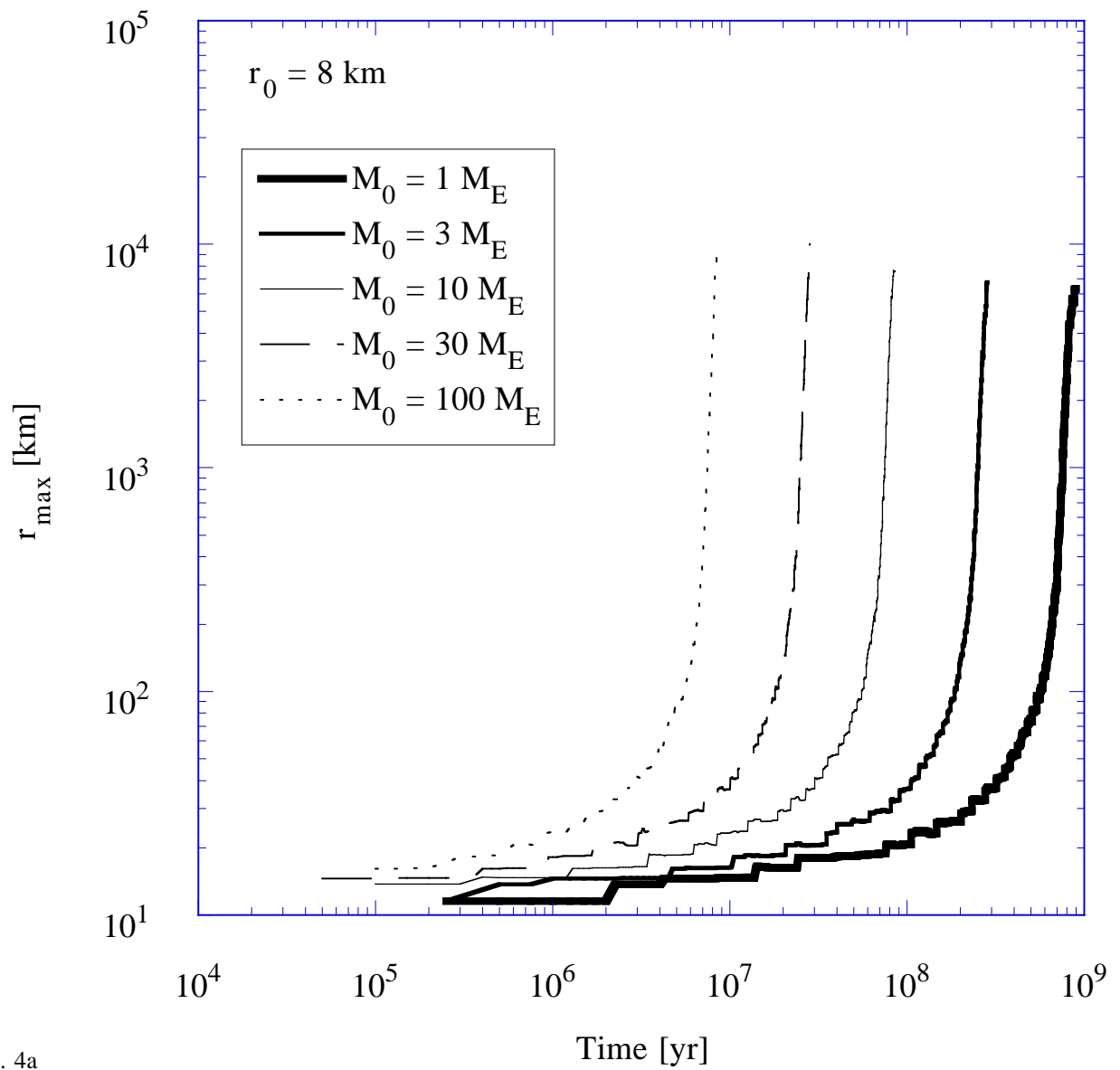


Fig. 4a

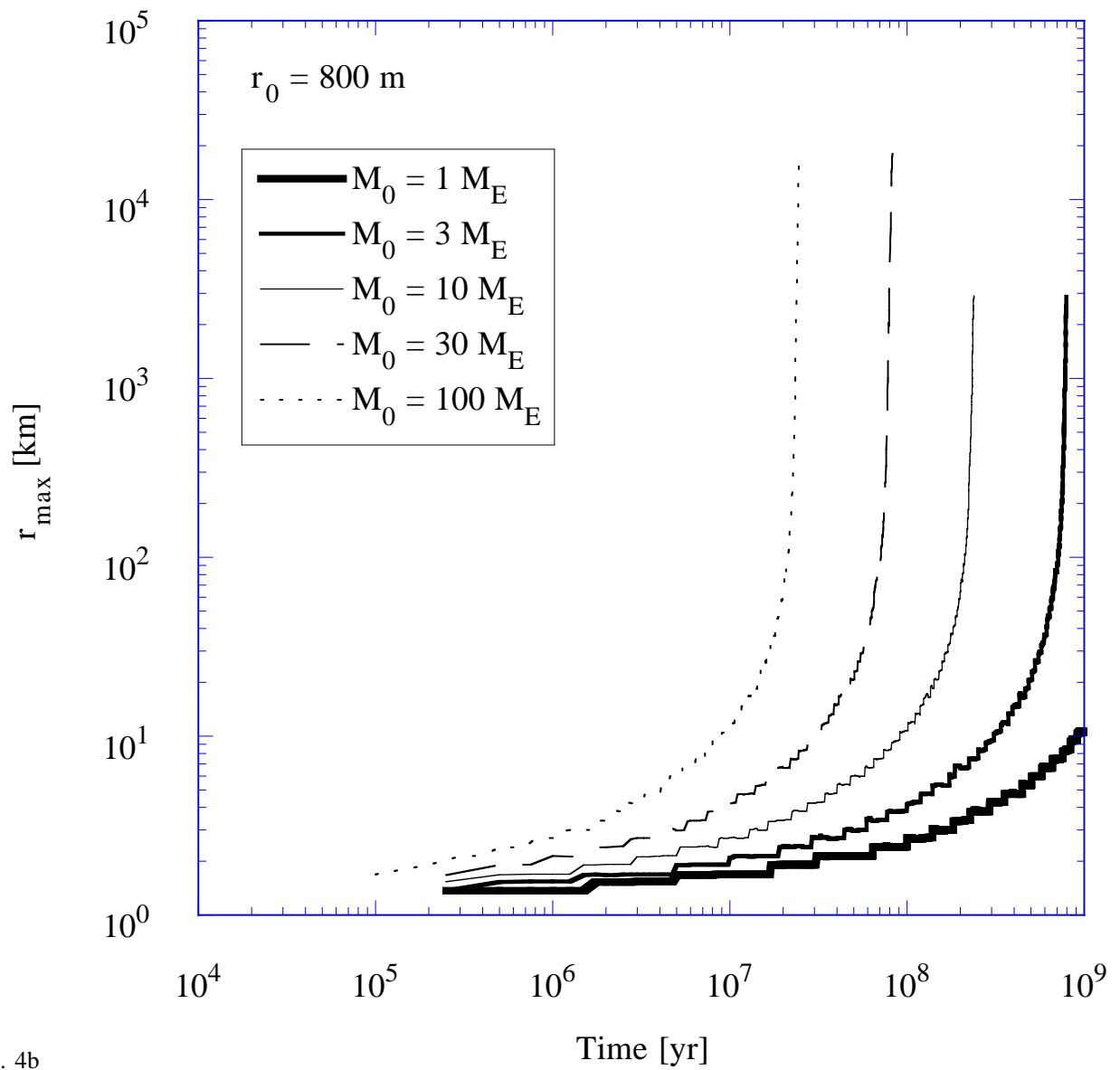


Fig. 4b

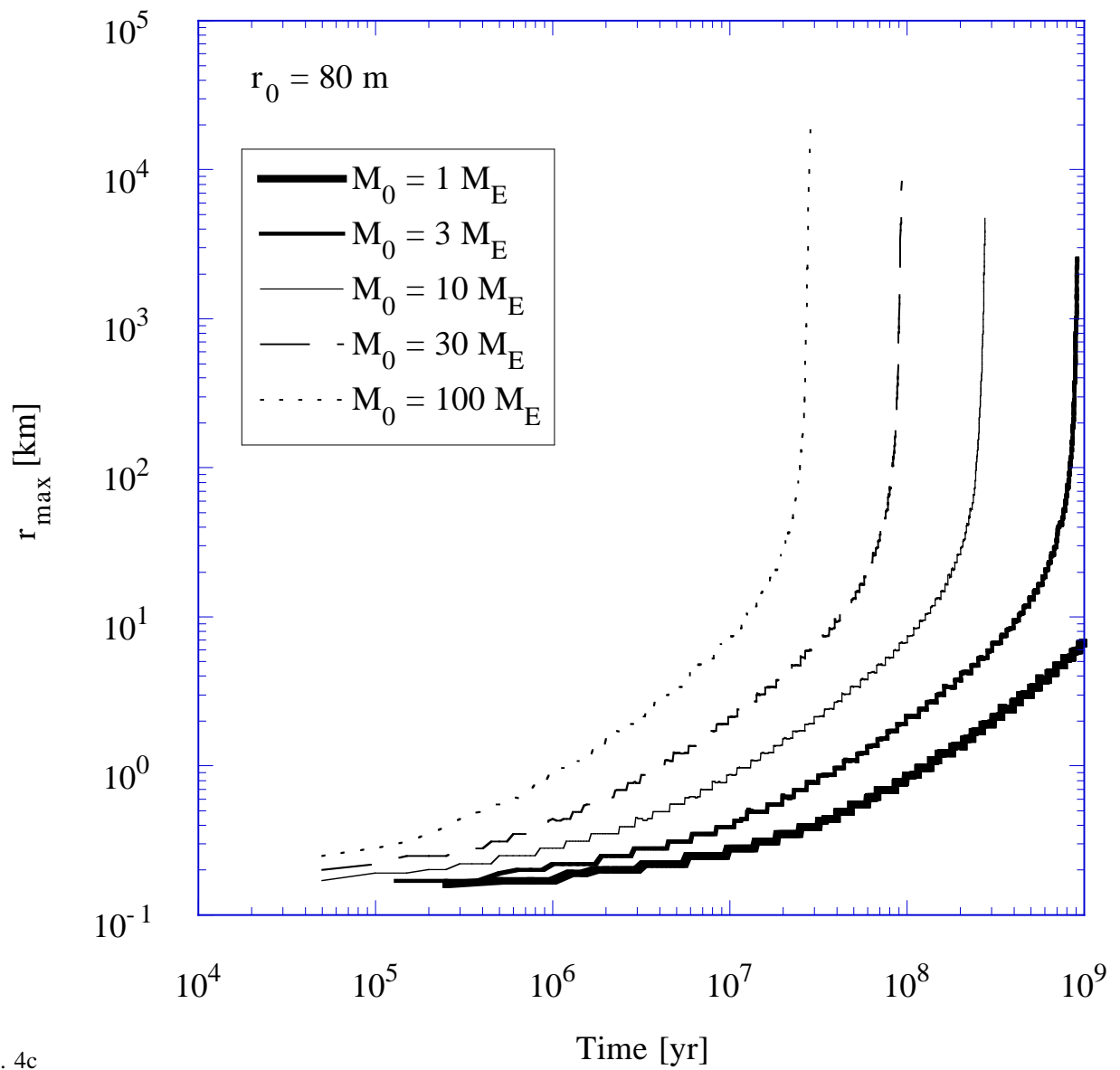


Fig. 4c

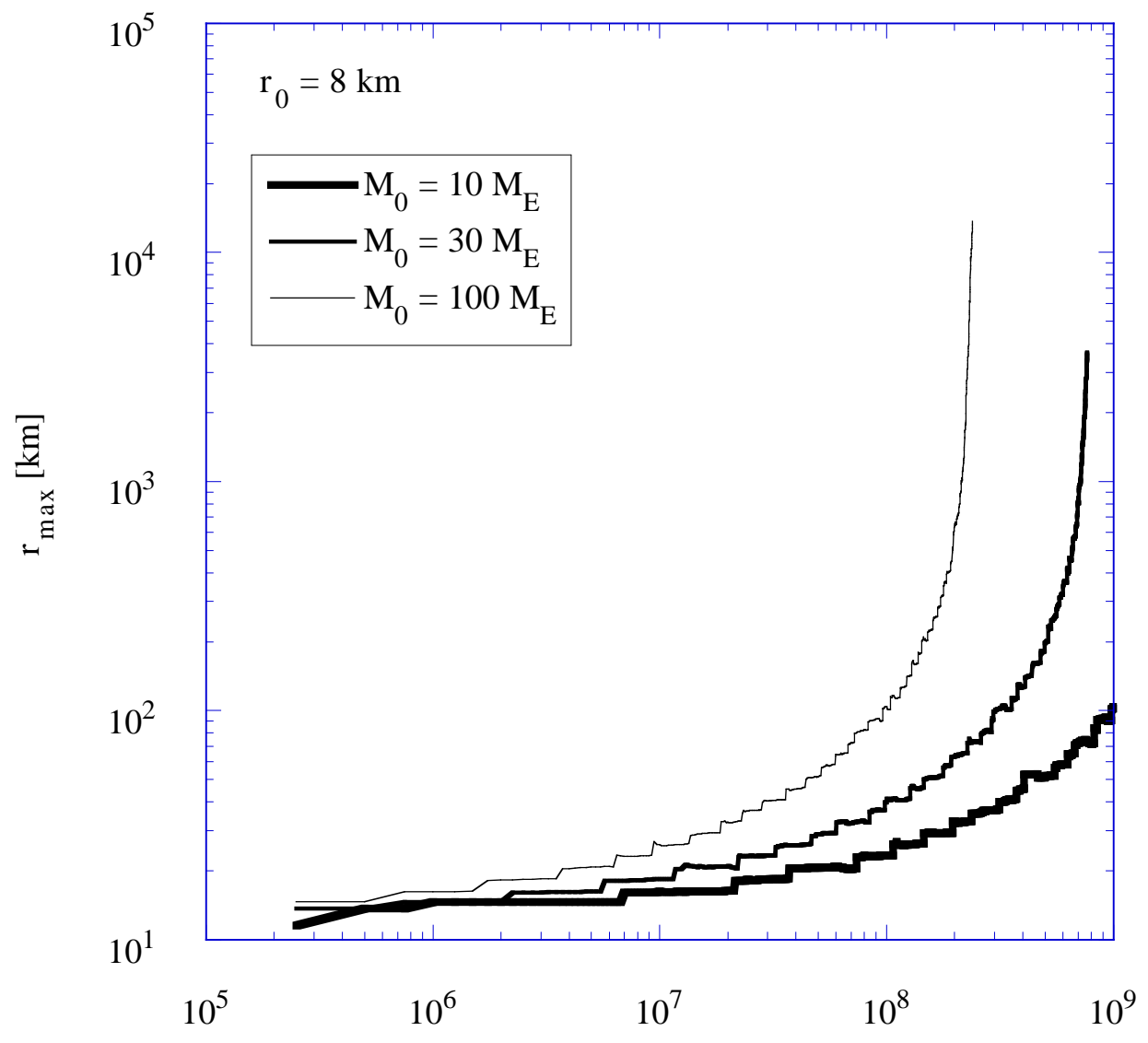


Fig. 5a

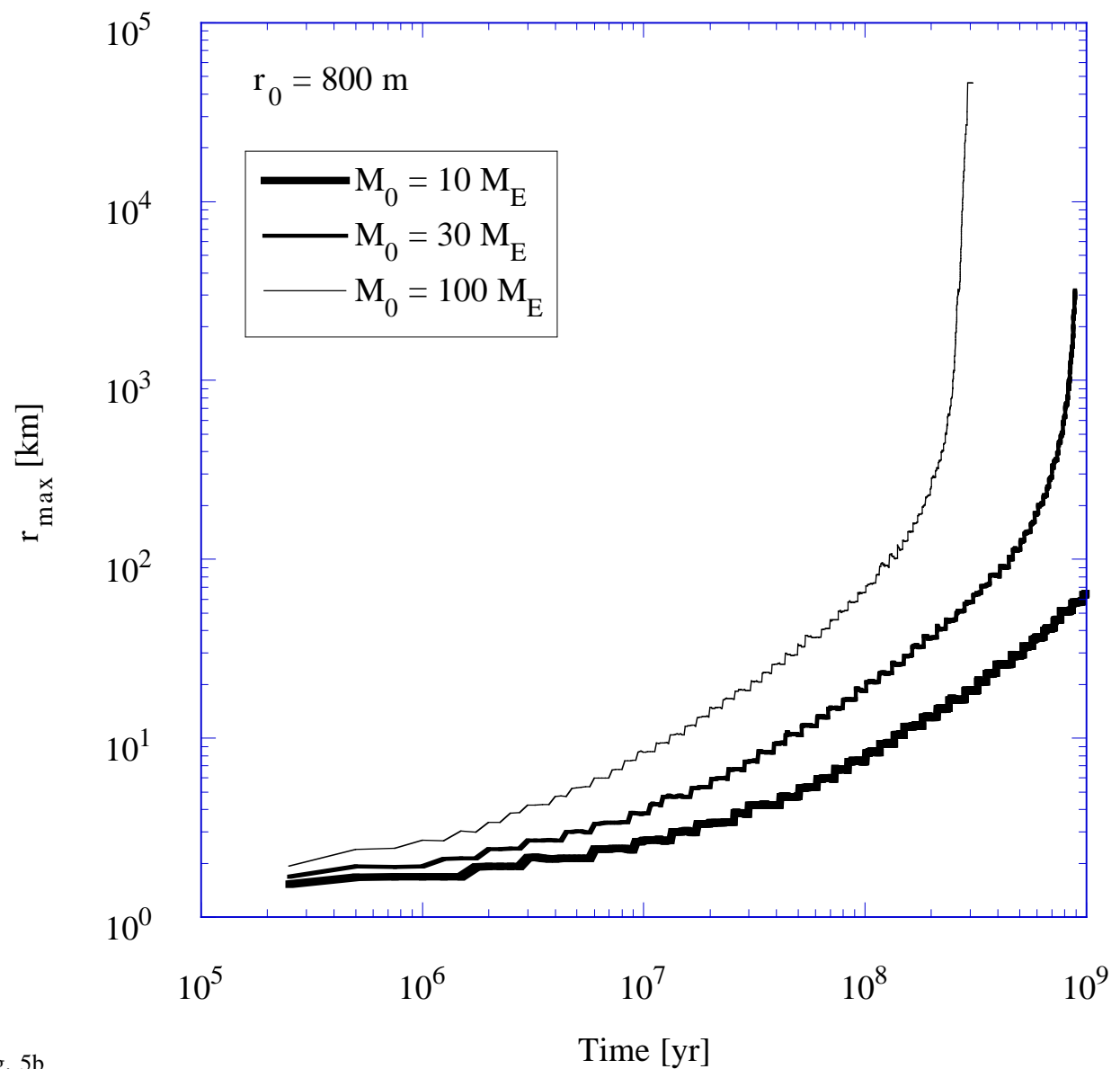


Fig. 5b

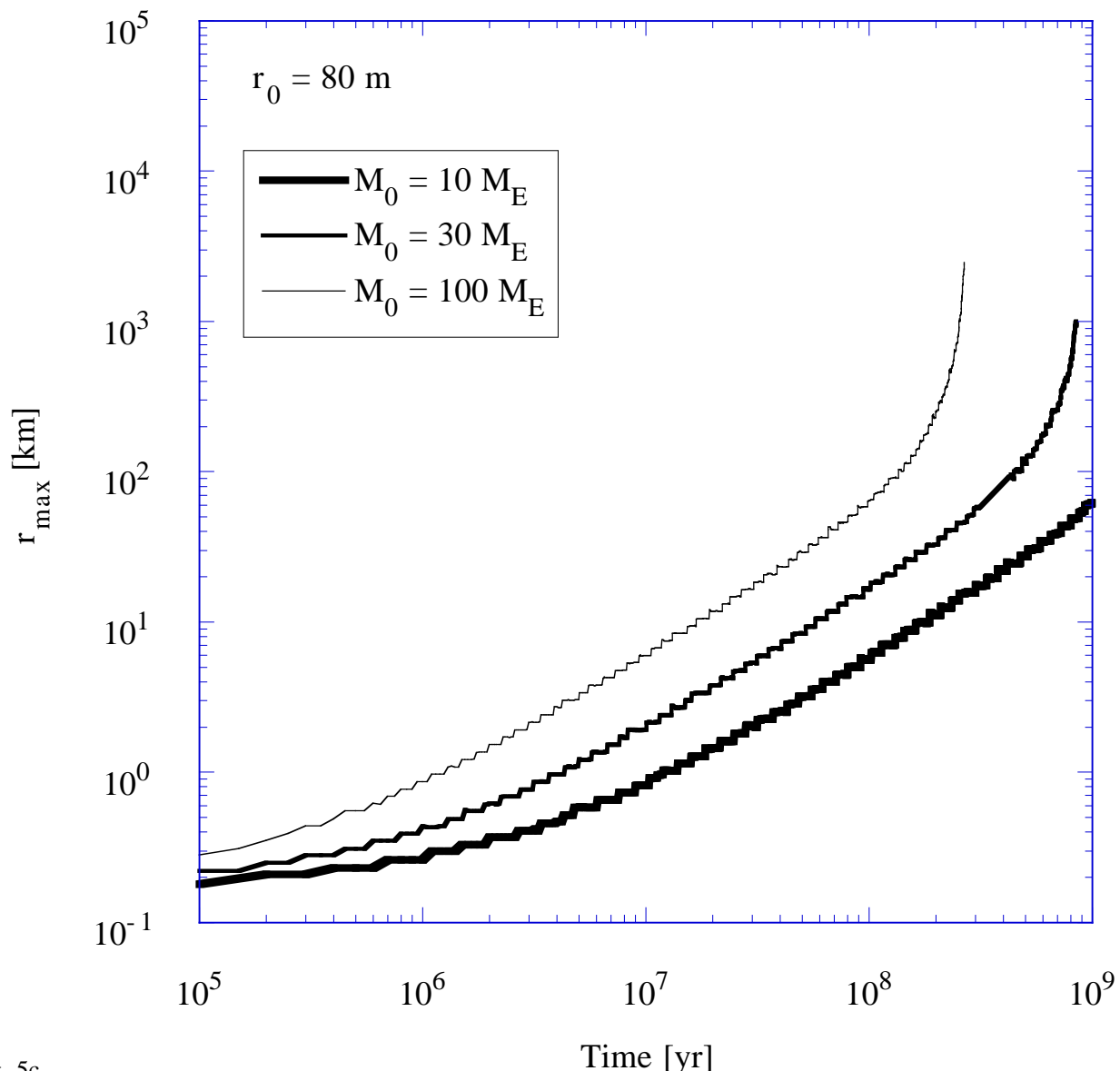


Fig. 5c

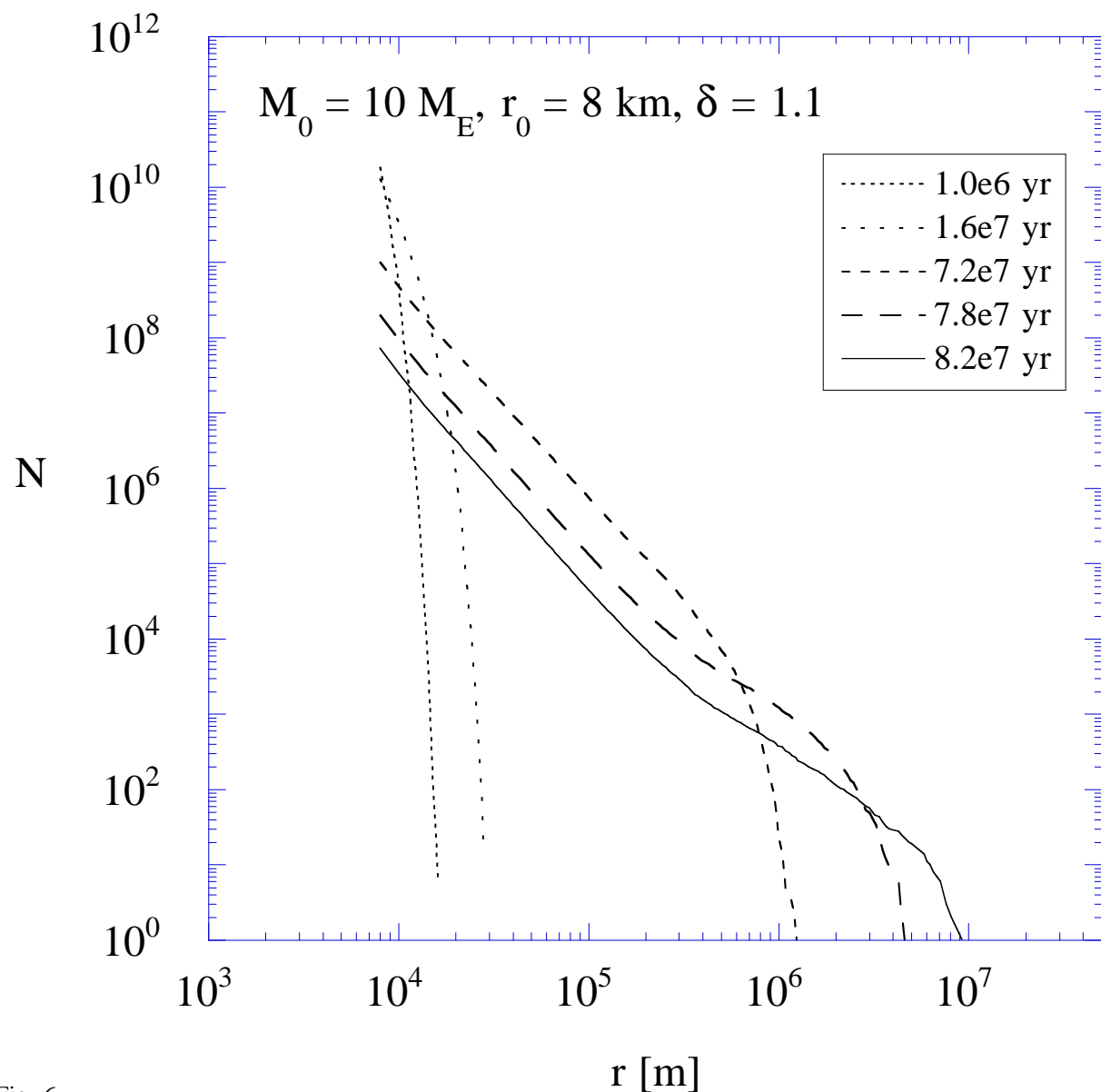


Fig. 6

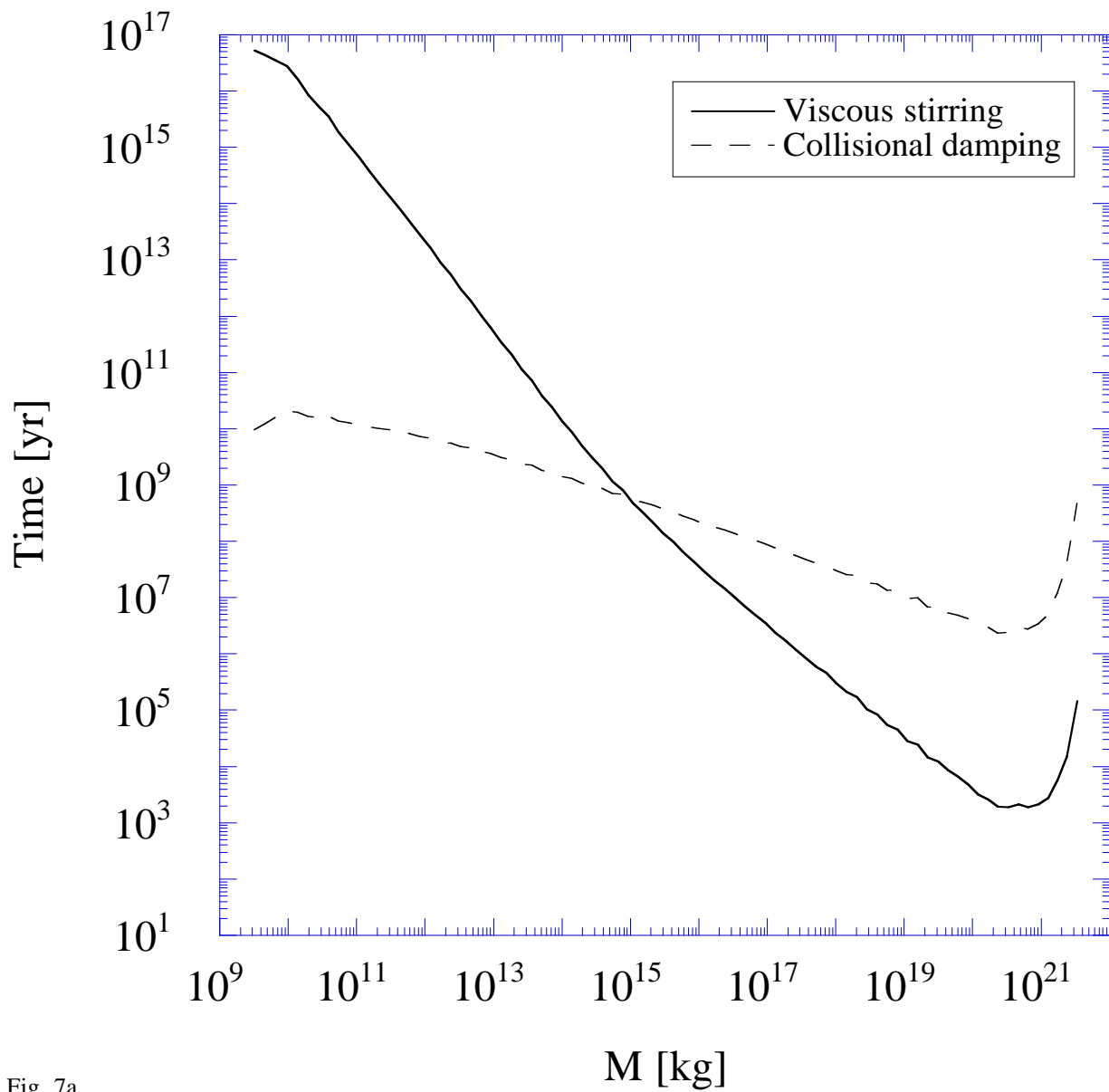


Fig. 7a

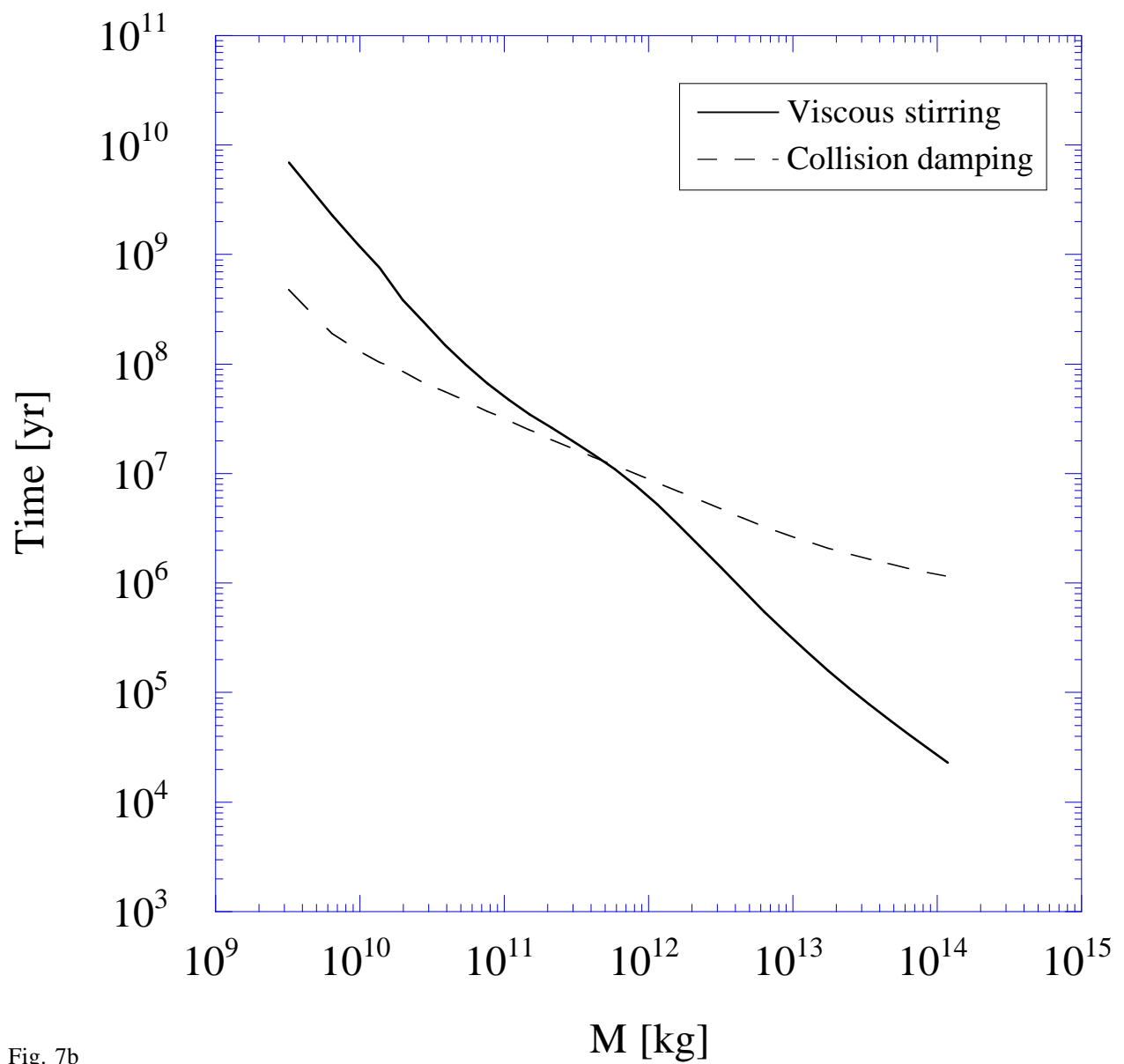


Fig. 7b

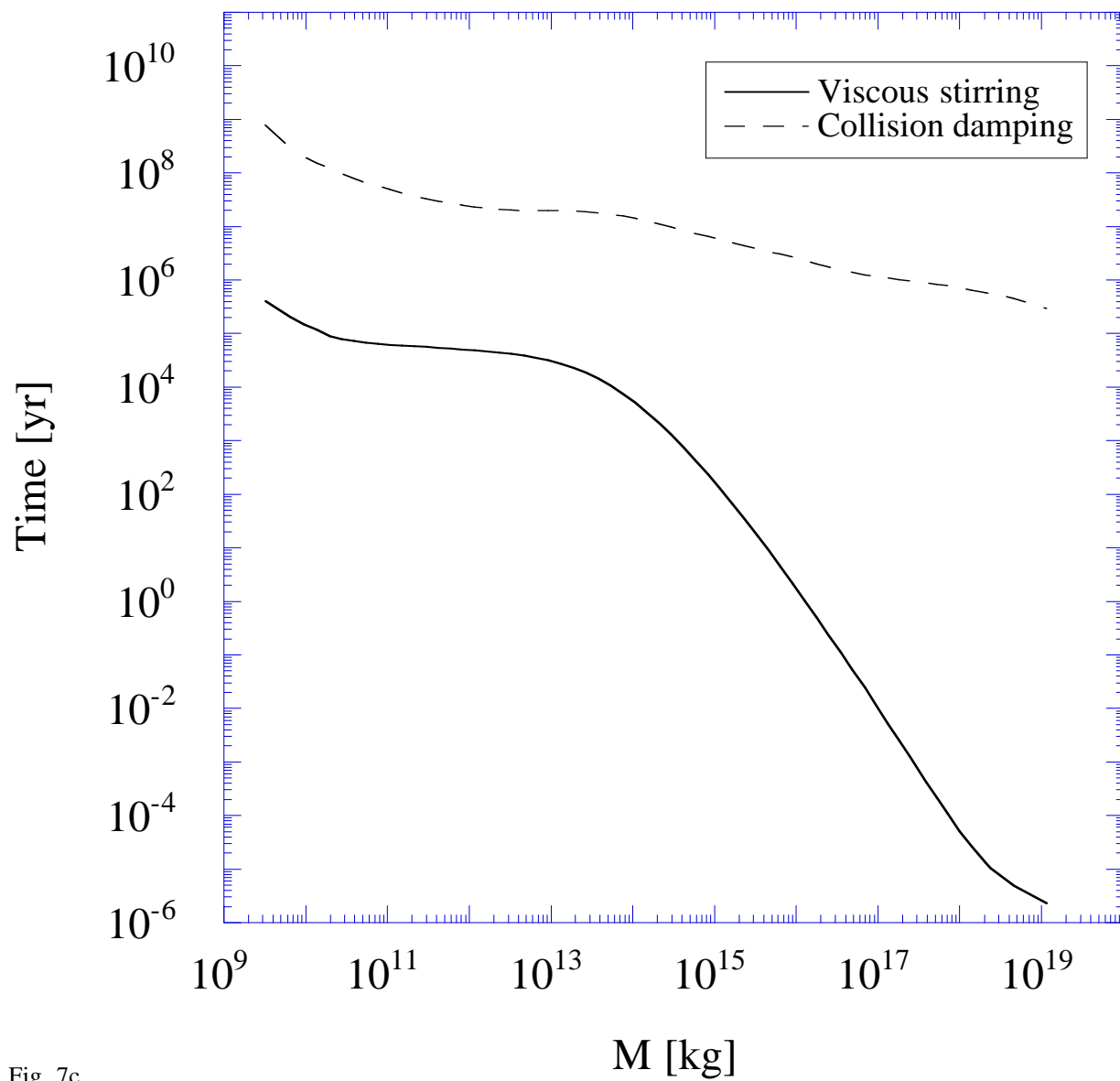


Fig. 7c

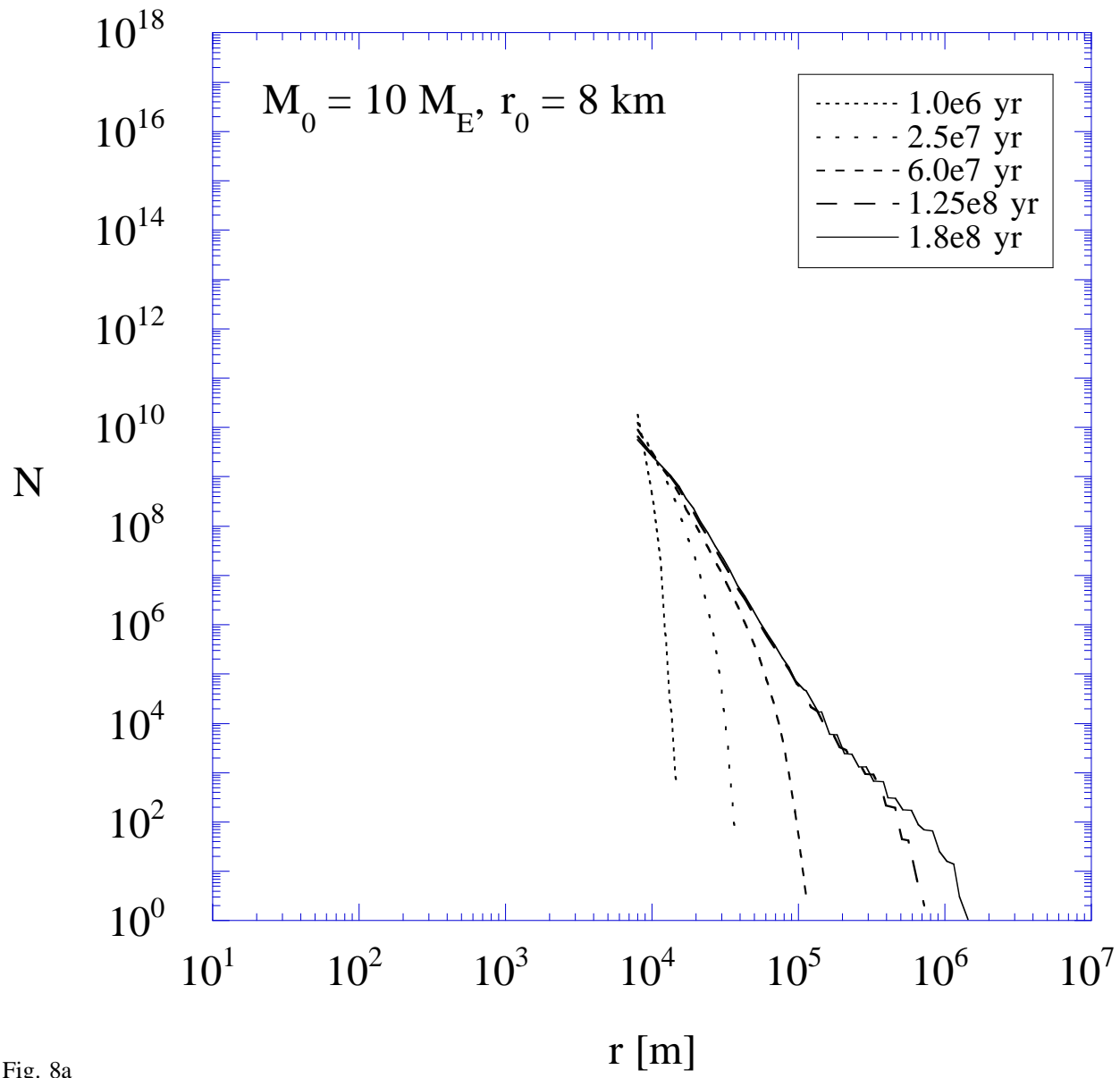


Fig. 8a

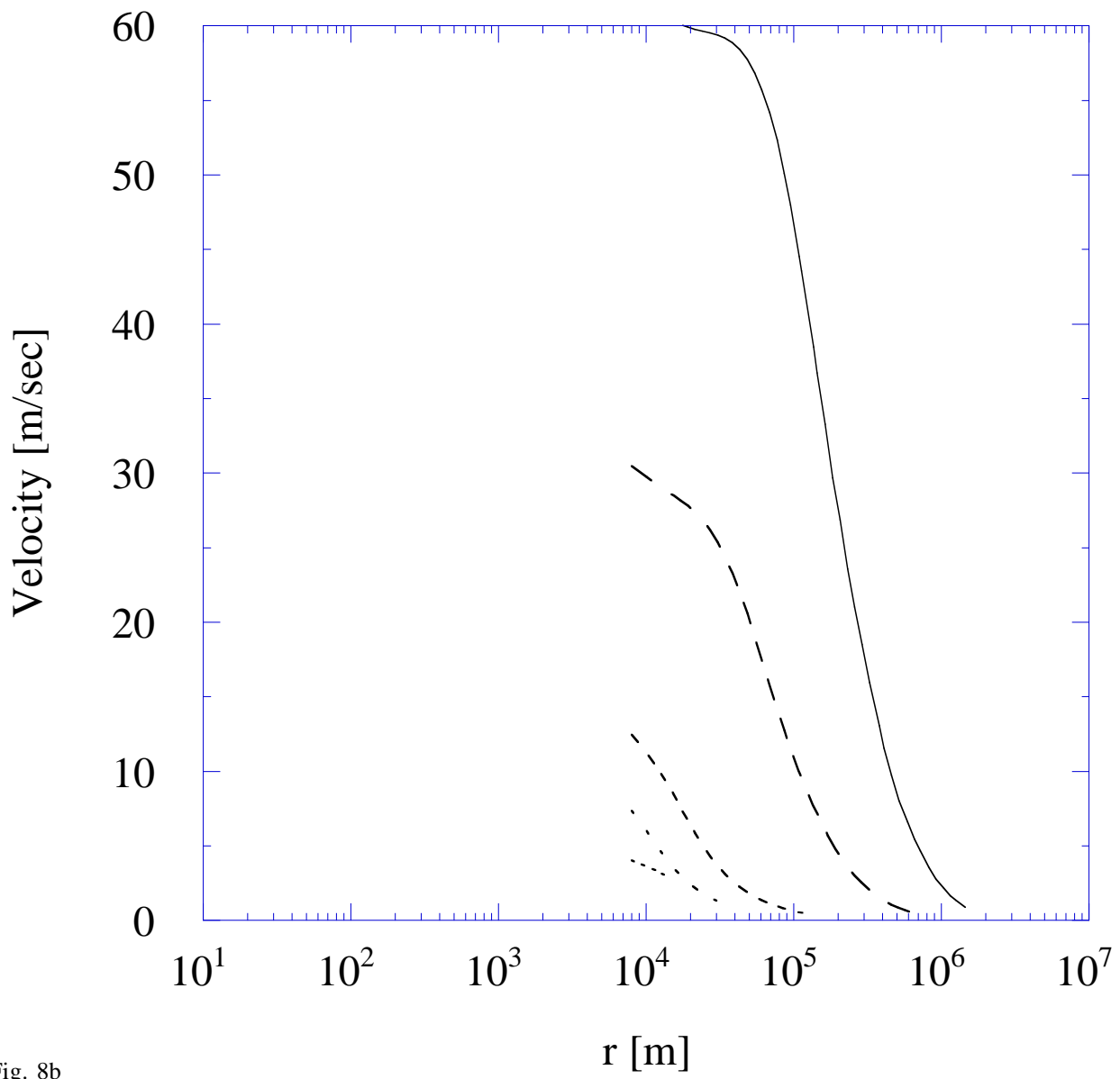


Fig. 8b

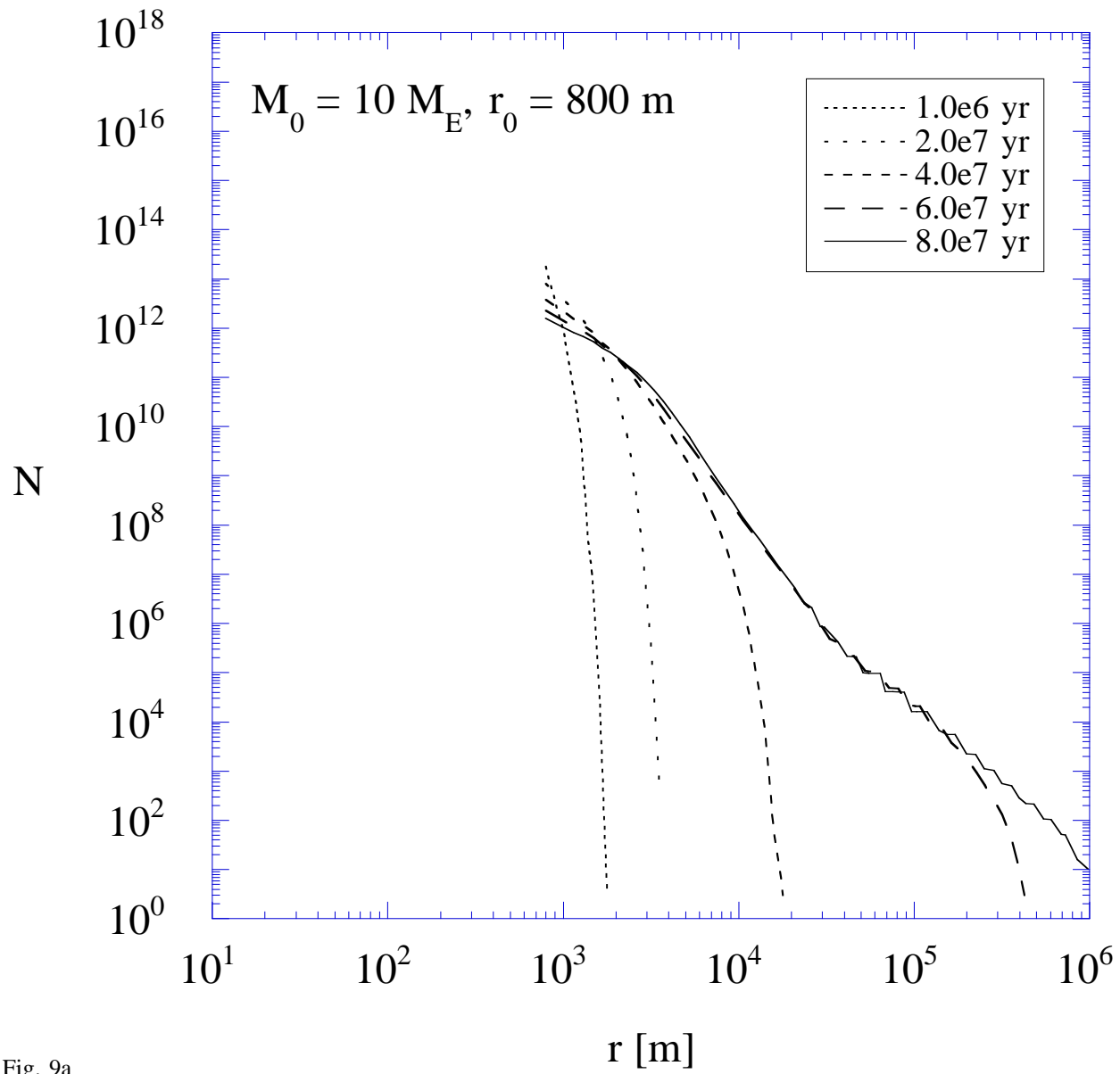


Fig. 9a

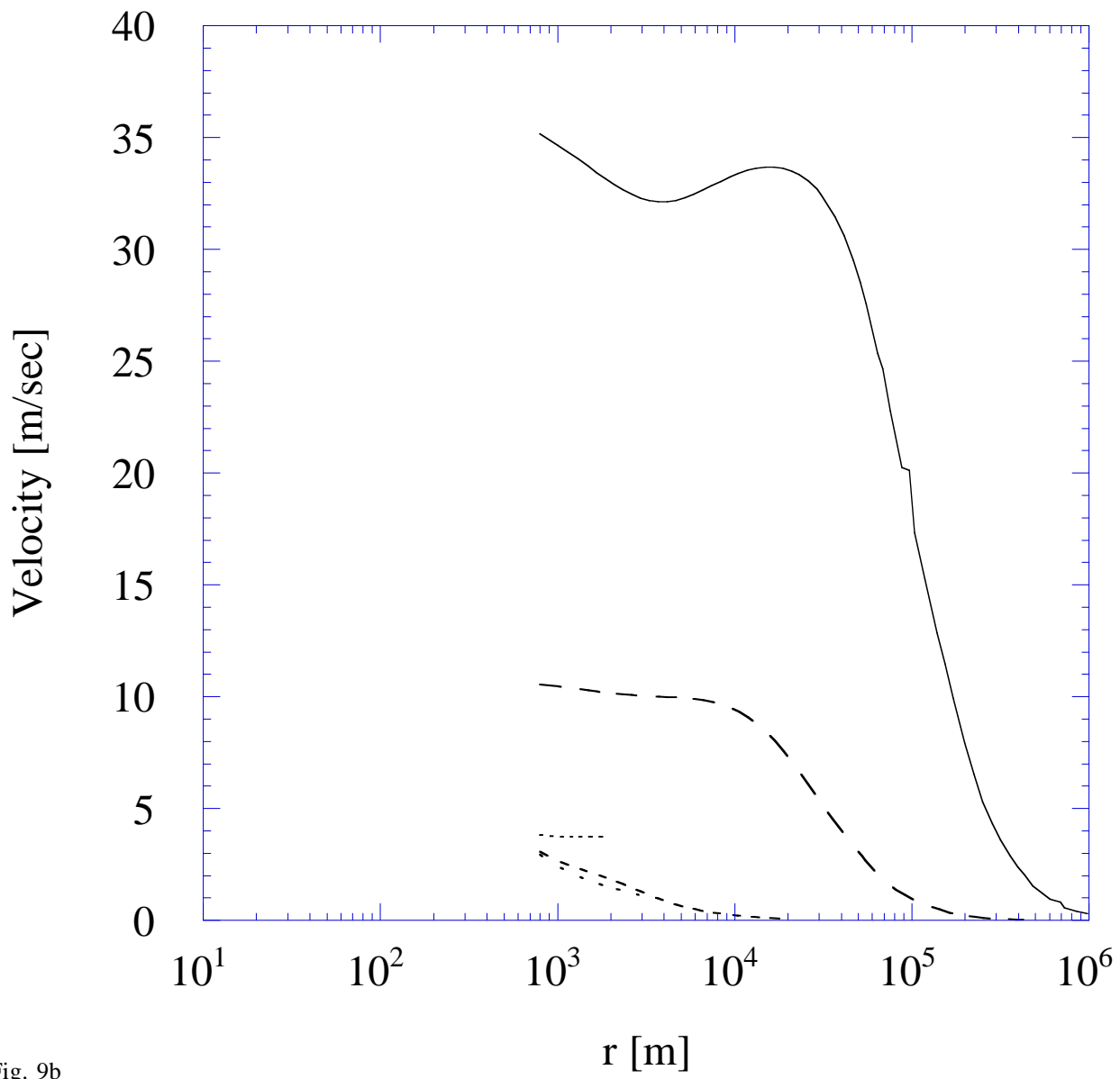


Fig. 9b

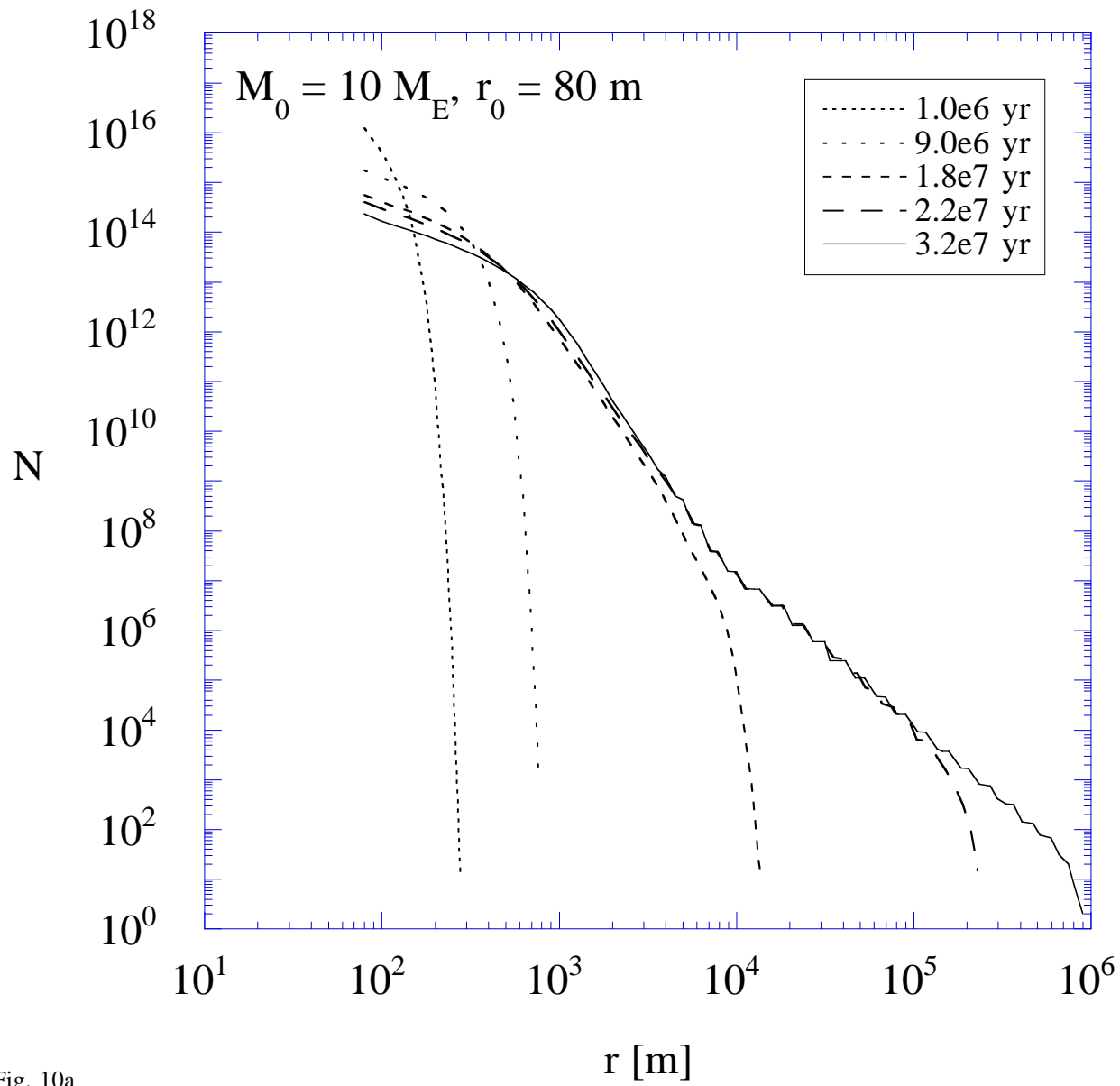


Fig. 10a

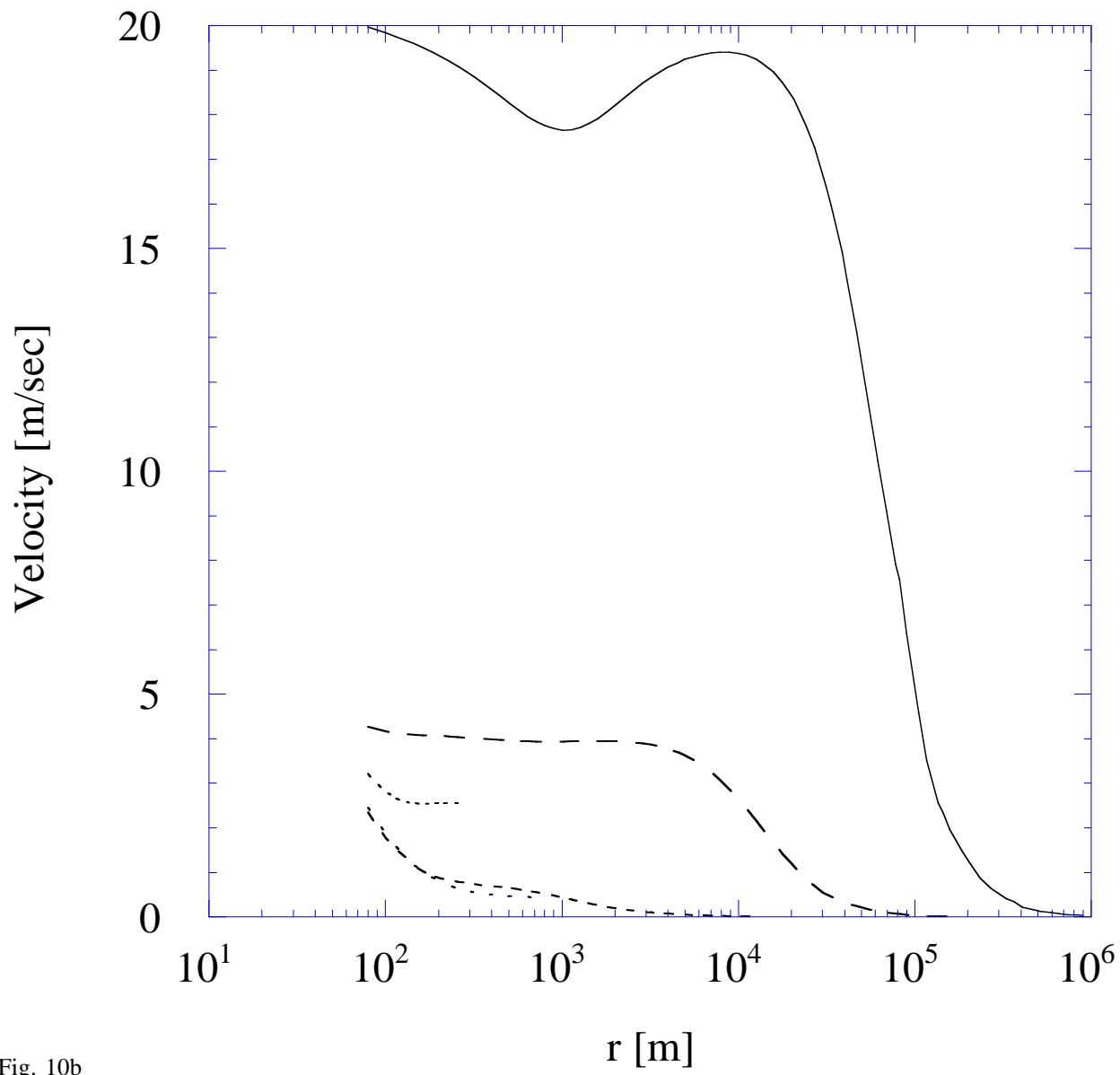


Fig. 10b

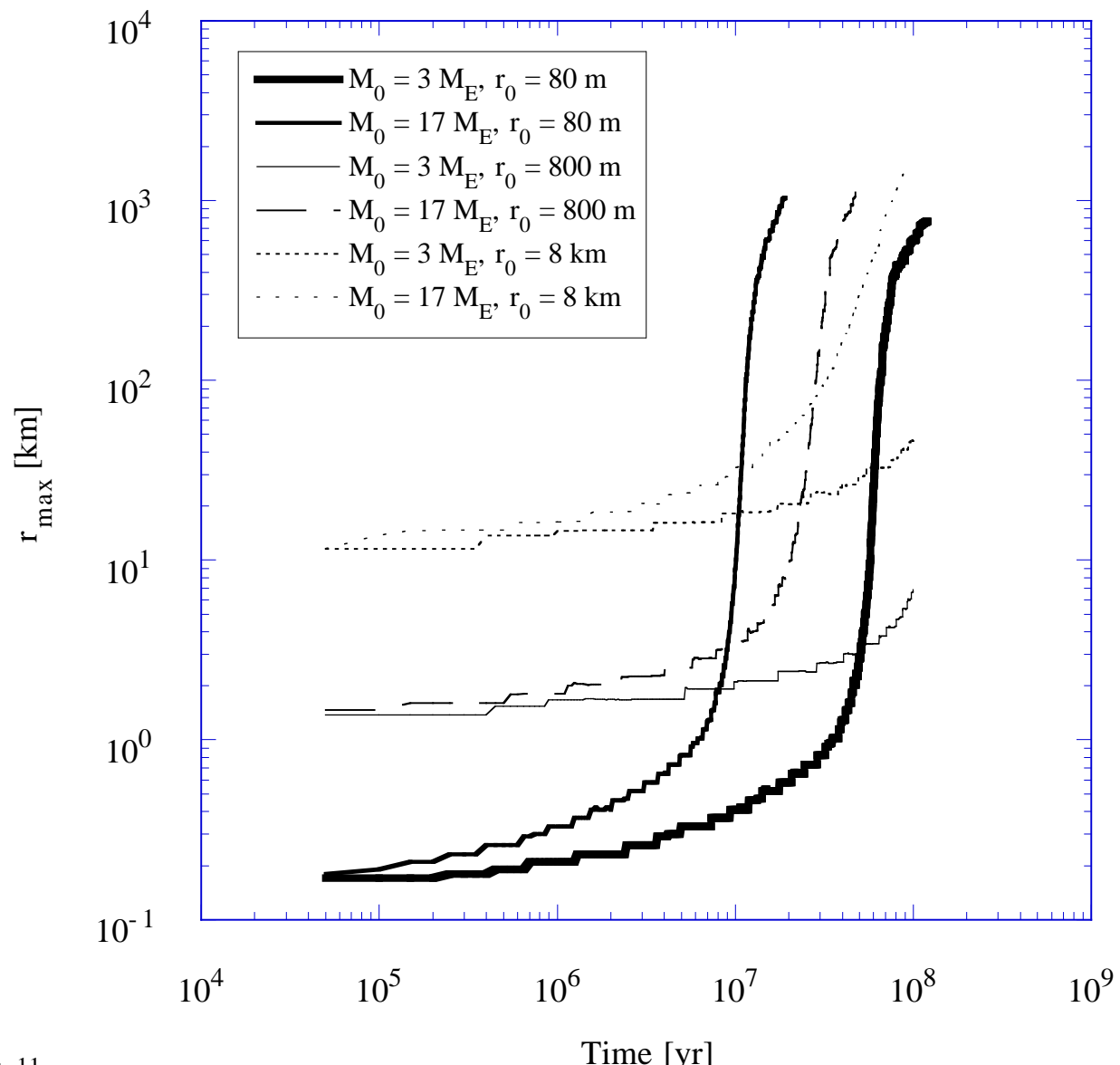


Fig. 11

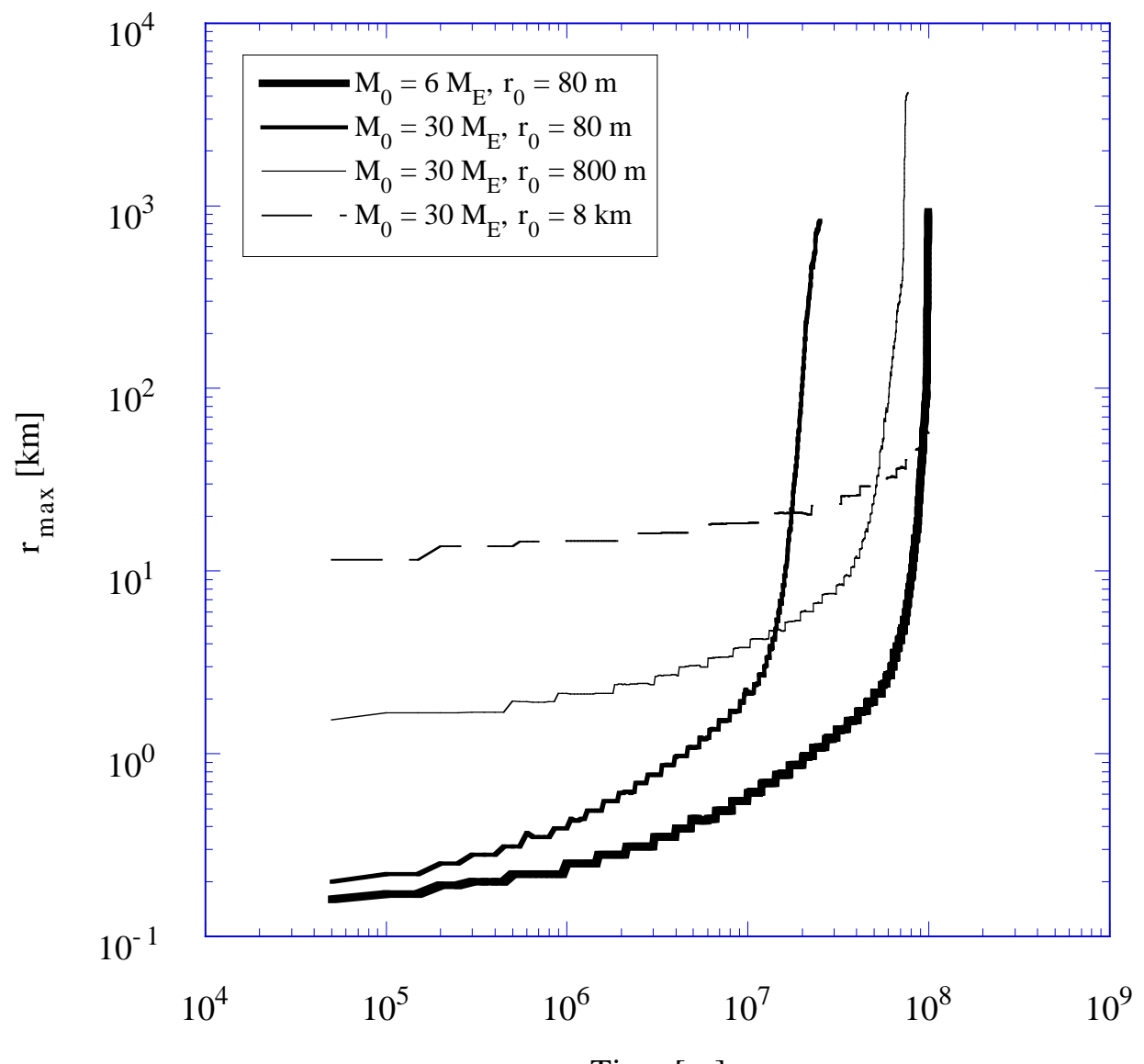


Fig. 12

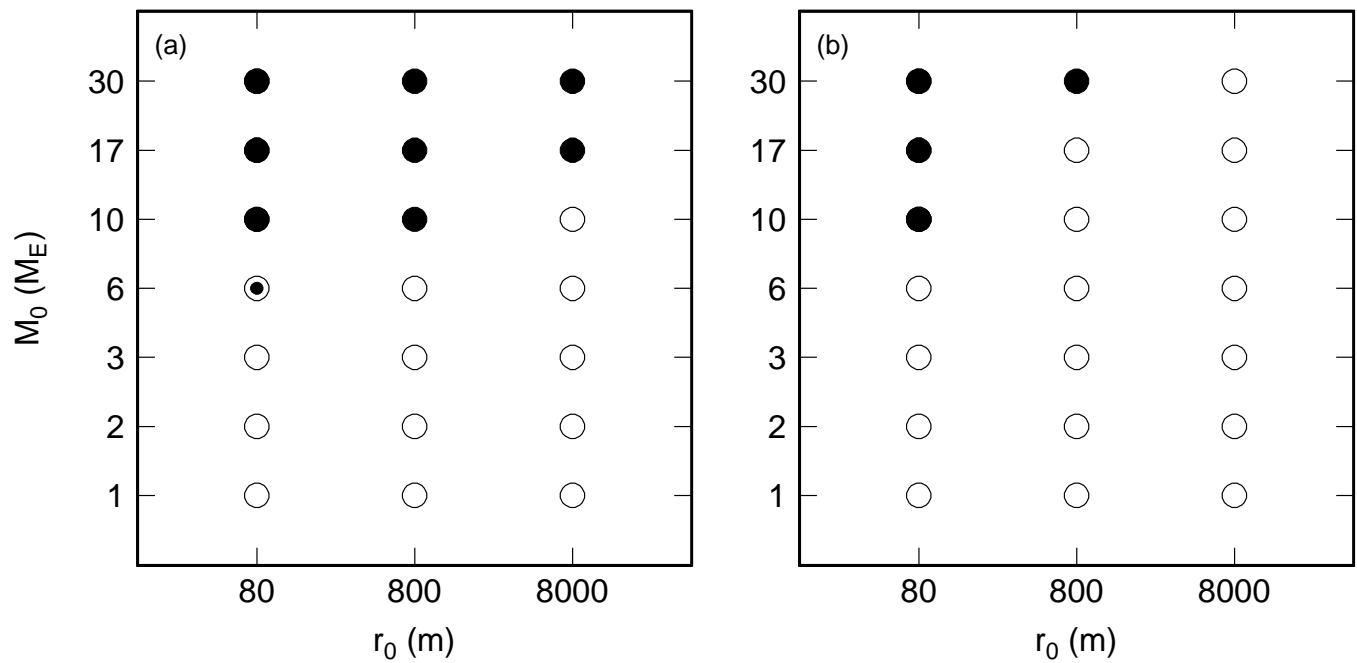


Fig. 13

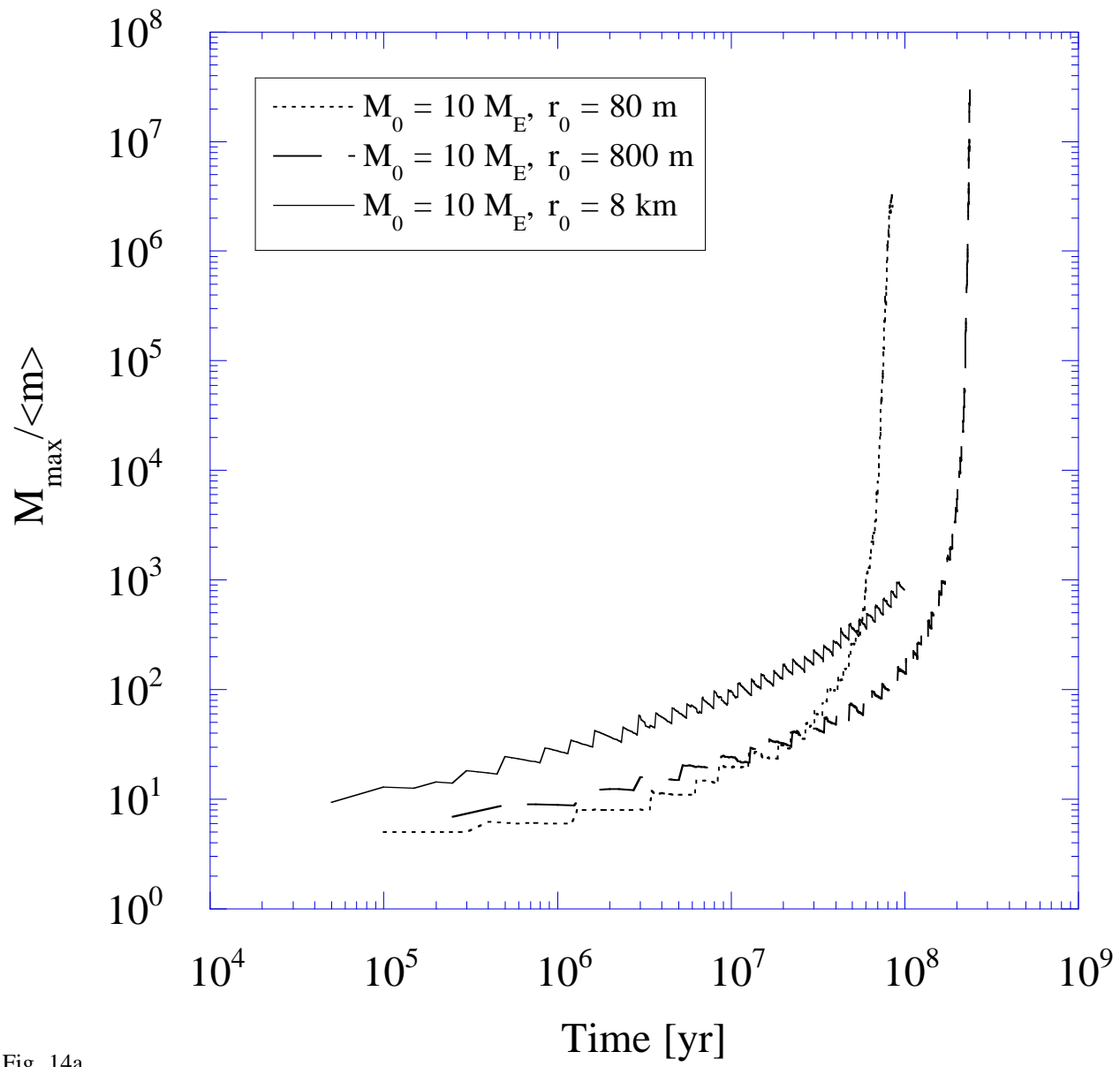


Fig. 14a

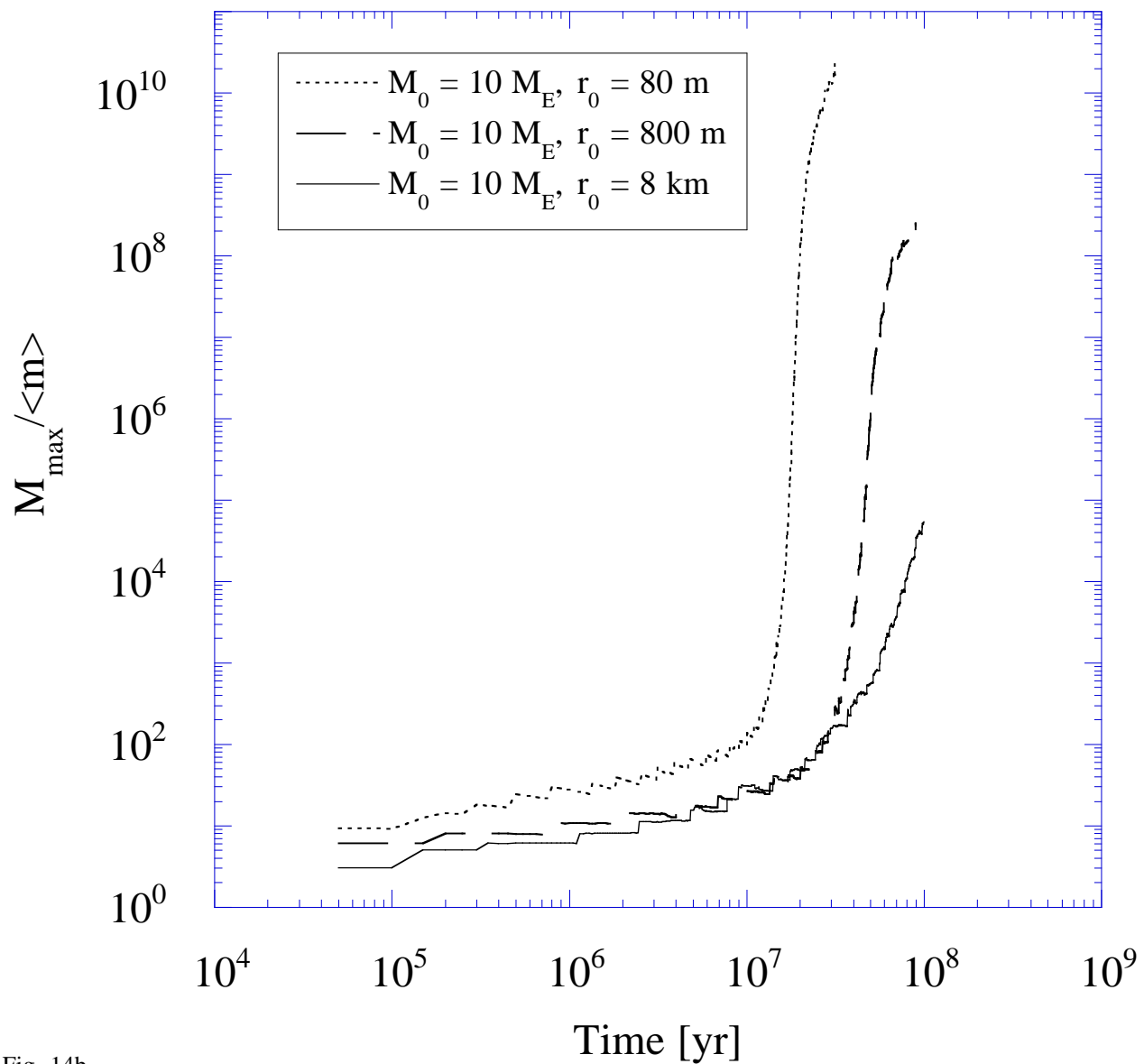


Fig. 14b

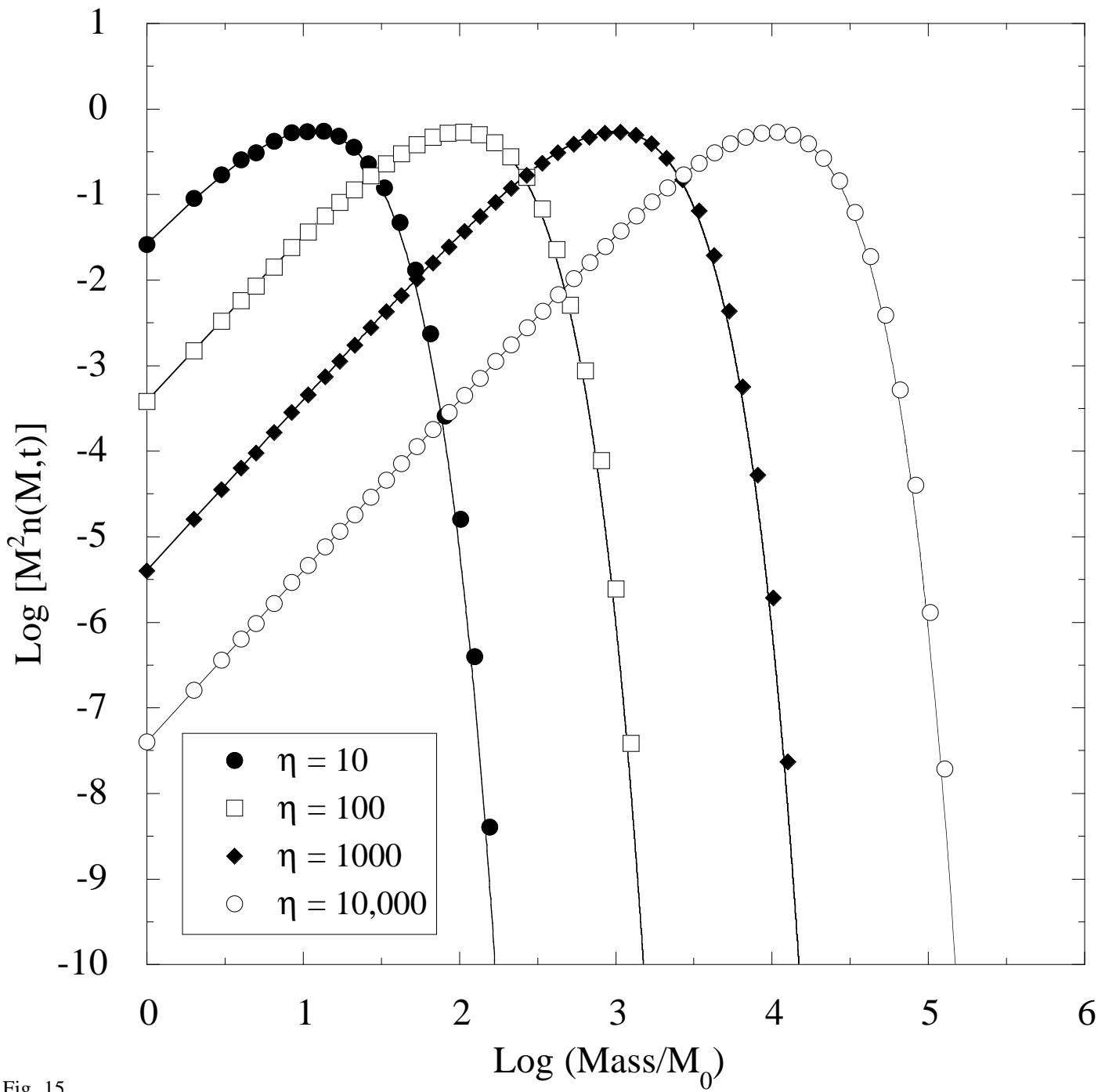


Fig. 15

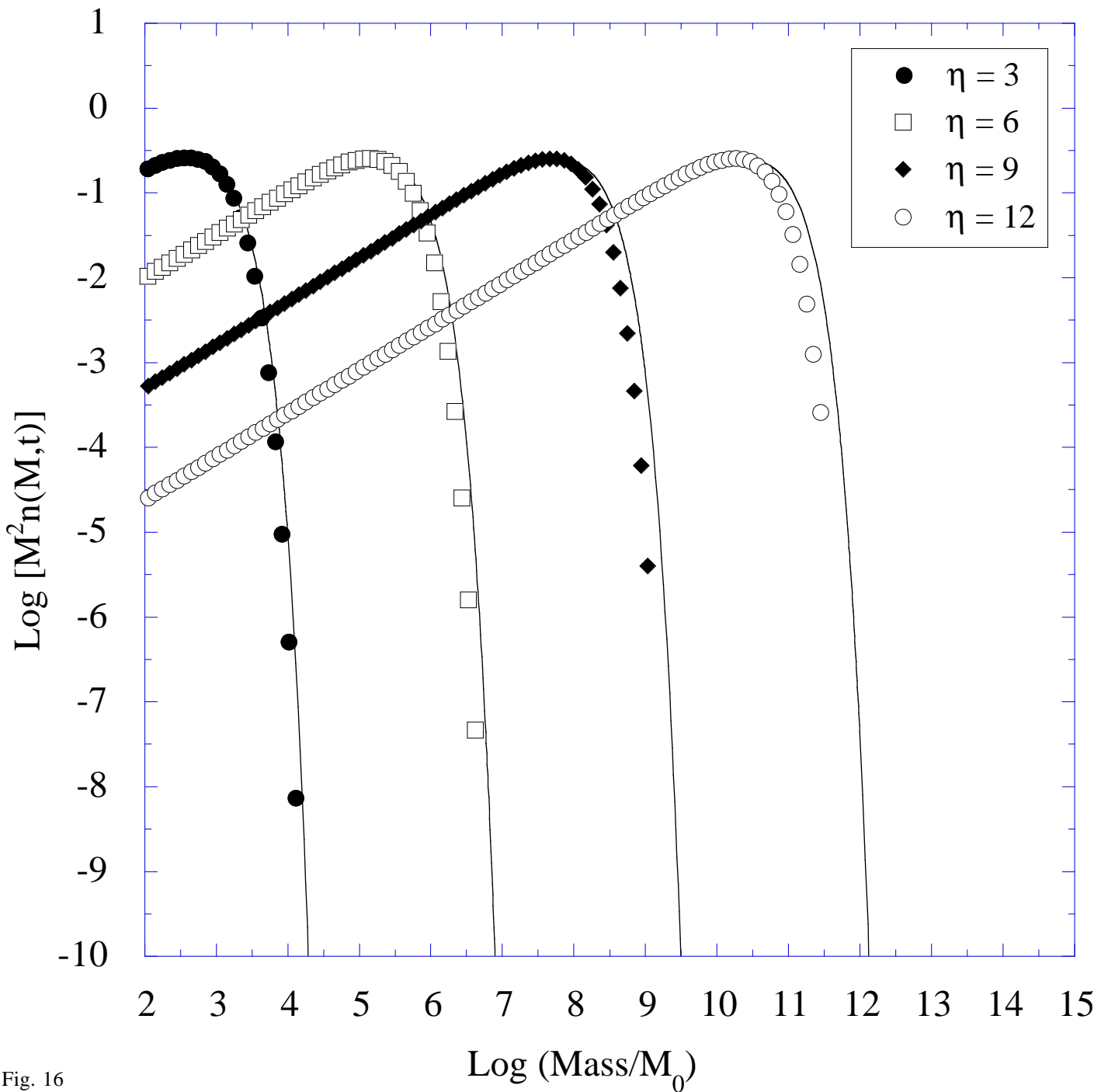


Fig. 16

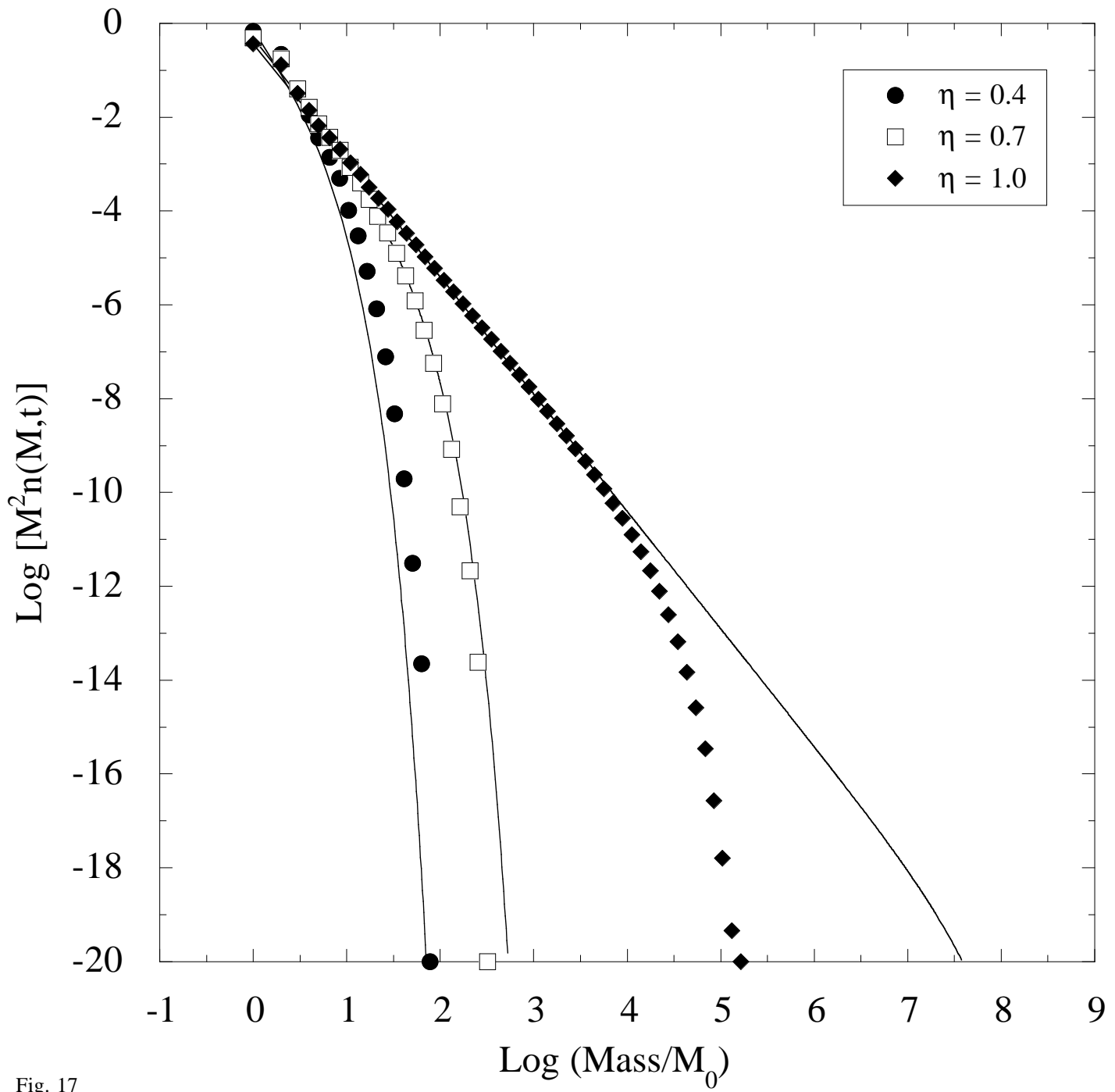


Fig. 17

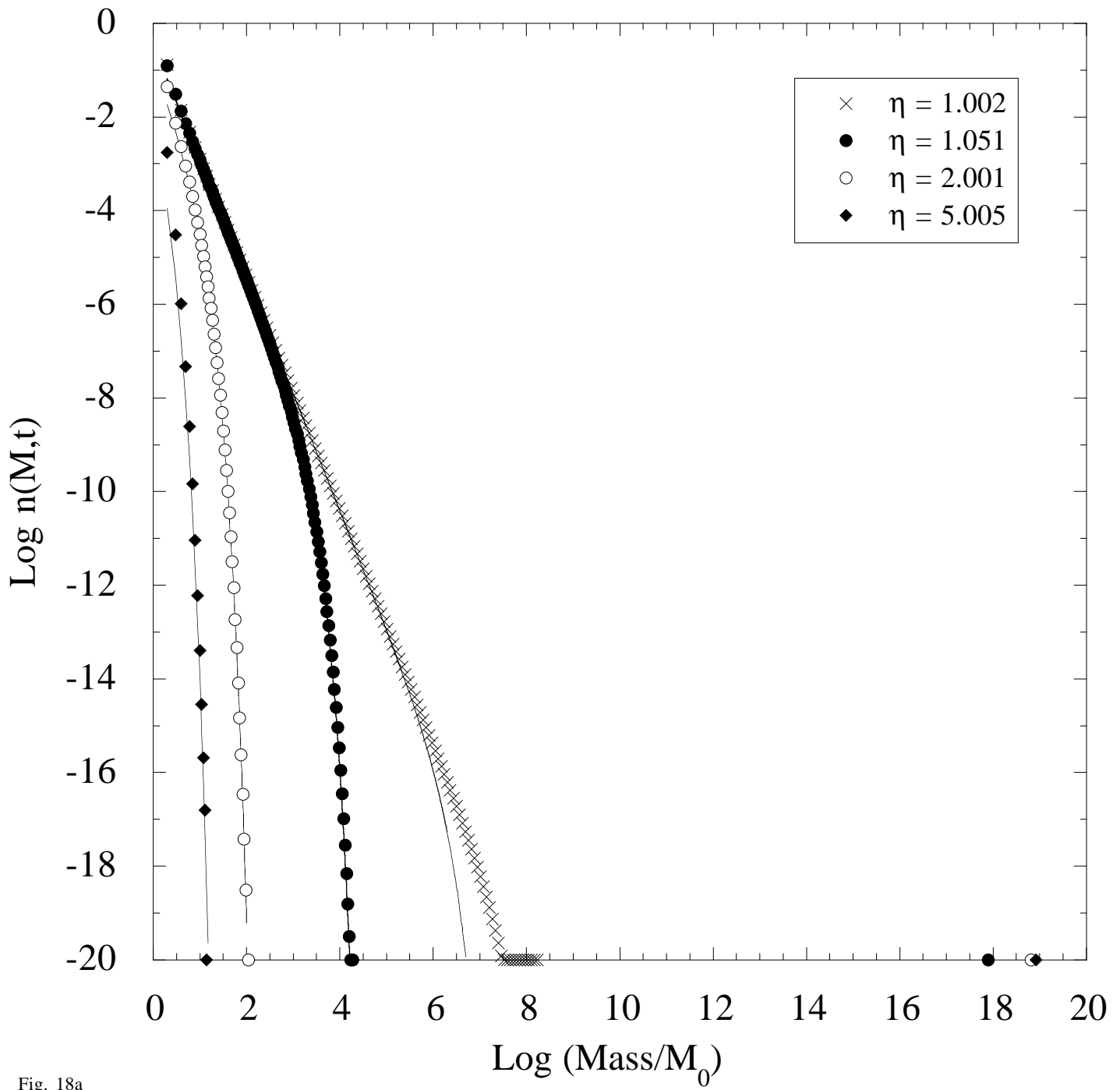


Fig. 18a

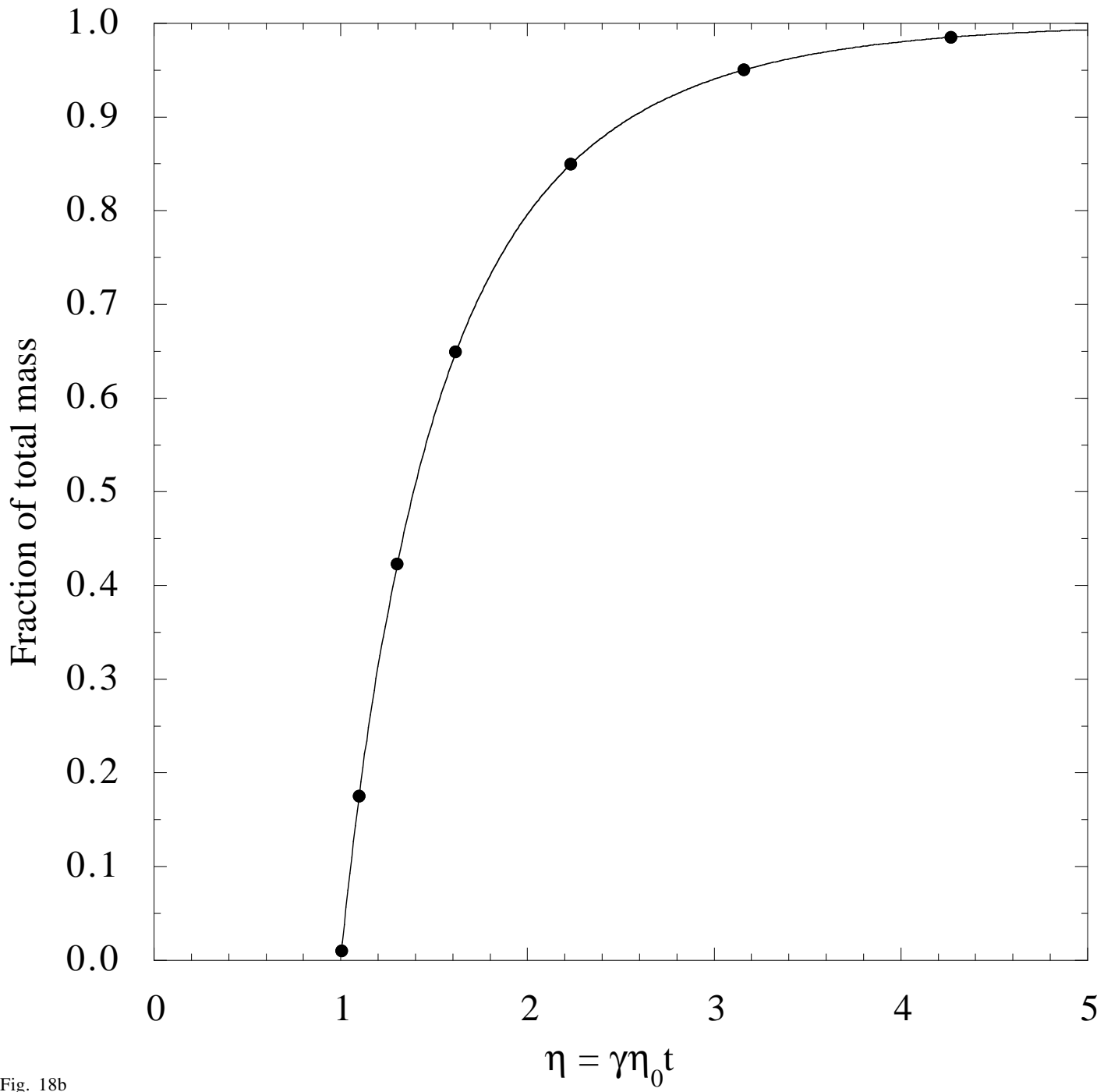


Fig. 18b